REPORT DOCUMENTATION PAGE

Form Approved
OMB No. 0704-0188

1. REPORT DATE *(DD-MM-YYYY)*	**2. REPORT TYPE**	**3. DATES COVERED** *(From - To)*
August 26, 2012	FINAL REPORT	7/1/2008 - 5/9/2011

4. TITLE AND SUBTITLE

HIGH PERFORMANCE PIEZOELECTRIC ACTUATORS AND WINGS FOR NANO AIR VEHICLES

5a. CONTRACT NUMBER

5b. GRANT NUMBER
FA9550-08-1-0293

5c. PROGRAM ELEMENT NUMBER

6. AUTHOR(S)

Christopher D. Rahn, Srinivas A. Tadigadapa

5d. PROJECT NUMBER

5e. TASK NUMBER

5f. WORK UNIT NUMBER

7. PERFORMING ORGANIZATION NAME(S) AND ADDRESS(ES)

Pennsylvania State University

8. PERFORMING ORGANIZATION REPORT NUMBER

9. SPONSORING / MONITORING AGENCY NAME(S) AND ADDRESS(ES)

Air Force Office of Scientific Research
Suite 325, Room 3112
875 Randolph Street
Arlington, VA 22203-1768

10. SPONSOR/MONITOR'S ACRONYM(S)

AFOSR

11. SPONSOR/MONITOR'S REPORT NUMBER(S)
AFRL-OSR-VA-TR-2012-0967

12. DISTRIBUTION / AVAILABILITY STATEMENT

Distribution A - Approved for Public Release

13. SUPPLEMENTARY NOTES

14. ABSTRACT

Swarms of flying robotic insects could revolutionize hazardous environment exploration, search and rescue missions, and military applications. Reducing size to insect scale enables entrance into extremely narrow spaces with inherent stealth advantages. For mass production, these vehicles must have reliable and repeatable fabrication processes that define flapping wing mechanisms with microscale features and produce large flapping amplitudes at frequencies in the range of many insects. This report focuses on the design and fabrication processes of flapping wing mechanisms for these types of robots.

15. SUBJECT TERMS

16. SECURITY CLASSIFICATION OF:			**17. LIMITATION OF ABSTRACT**	**18. NUMBER OF PAGES**	**19a. NAME OF RESPONSIBLE PERSON**
a. REPORT	**b. ABSTRACT**	**c. THIS PAGE**			Christopher D. Rahn
U	U	U	U	143	**19b. TELEPHONE NUMBER** *(include area code)* 814-865-6237

Standard Form 298 (Rev. 8-98)
Prescribed by ANSI Std. Z39.18

HIGH PERFORMANCE PIEZOELECTRIC ACTUATORS AND WINGS FOR NANO AIR VEHICLES

AFOSR Grant No. FA9550-08-1-0293

Christopher D. Rahn
Professor of Mechanical Engineering

Srinivas A. Tadigadapa
Professor of Electrical Engineering

The Pennsylvania State University

FINAL REPORT

August 26, 2012

Abstract

Swarms of flying robotic insects could revolutionize hazardous environment exploration, search and rescue missions, and military applications. Reducing size to insect scale enables entrance into extremely narrow spaces with inherent stealth advantages. For mass production, these vehicles must have reliable and repeatable fabrication processes that define flapping wing mechanisms with microscale features and produce large flapping amplitudes at frequencies in the range of many insects. This report focuses on the design and fabrication processes of flapping wing mechanisms for these types of robots.

First, the design, fabrication, modeling, and experimental validation of the Penn State Nano Air Vehicle (PSNAV), a NAV scale piezoelectrically actuated clapping wing mechanism, is presented. A flexure hinge allows passive wing rotation for the clapping wing mechanism. Analytical models of wing flapping and rotation are derived and validated using experimental wing trajectory results. The PSNAV prototype is experimentally shown to provide approximately 54 $deg.$ peak to peak wing rotation, 14 $deg.$ peak to peak flapping angle, and 0.21 mN of thrust at 9.5 Hz. At 25.5 Hz, the prototype produces a maximum of 1.34 mN of thrust. The PSNAV model accurately predicts the wing resonances in the experimental prototype. Model-predicted thrust is lower than the experimentally measured values, however.

Towards a compliant mechanism, the next stage of this research introduces a simple process to monolithically fabricate flying robotic insects at the pico air vehicle (PAV) scale from SUEX dry film, an epoxy based negative photoresist similar to SU-8. The developed process has fewer steps compared to other methods, does not use precious metals, and greatly reduces processing time and cost. It simultaneously defines the PAV airframe, compliant flapping mechanism, and artificial insect wing using photolithography. Using this process, we designed and fabricated the LionFly, a flapping wing prototype actuated by a PZT-5H bimorph actuator. Several LionFly prototypes were fabricated and experimentally tested. Theoretical and experimental results have excellent agreement validating the compliant mechanism kinematics and aerodynamic added mass and damping. High voltage tests show a peak to peak flapping angle of 55 $deg.$ at 150 V amplitude with 150 V DC offset at 51 Hz resonance. Consistent performance from multiple prototypes demonstrate the reliable and repeatable nature of the fabrication process.

Lastly, this research presents detailed modeling and experimental testing of wing rotation and lift in the LionFly. A flexure hinge along the span of the wing allows the wing to rotate in addition to flapping. A linear vibrational model is developed and augmented with nonlinear aerodynamic forces using the blade element method. This model is validated using experimental testing with a laser vibrometer and accurately predicts small amplitude wing dynamics in air and vacuum. Strobe photography and high definition image processing is used to measure high amplitude wing trajectories. At higher amplitudes, the model can sufficiently predict wing trajectory amplitudes, but phase measurement and simulation have slight error. The LionFly produces 46 $deg.$ flap and 44 $deg.$ rotation peak to peak with relative phase of 12 $deg.$, and maximum lift of 71 μN at 37 Hz. By reducing the inertia of the wing and tuning the rotational hinge stiffness, a redesigned device

is simulated to produce lift to weight ratio of one.

Table of Contents

List of Figures

List of Tables

Chapter 1

Introduction

Miniature unmanned air vehicles have been increasingly popular over the last decade for potential reconnaissance and search and rescue applications. DARPA defines Micro Air Vehicles (MAVs) as having wingspans less than 15 cm, and the next generation Nano Air Vehicles (NAVs) as having wingspans less than 7.5 cm, weight less than 10 grams, with payload capability of 2 grams[2]. Recently, Wood has defined a Pico Air Vehicle (PAV), with a maximum takeoff weight of 500 milligrams and maximum dimension of five centimeters [3]. Reducing size to insect scale enables entrance into extremely narrow spaces with inherent stealth advantages.

Typical air vehicle configurations consist of fixed wings[4] or rotary wings[5]. The superior maneuverability of small birds and insects have motivated researchers to explore flapping wing mechanisms for NAVs[6, 7, 8]. The potential ability to fly at both high and low speeds, hover and glide give flapping wing air vehicles advantages over miniature fixed wing aircraft. In addition, if designed properly, these vehicles could hide in plain sight and mimic a small bird or insect which current rotary wing aircraft cannot achieve. The smaller dimensions and unique wing trajectory specifications present many challenges in the design and fabrication of flapping wing actuators and mechanisms.

Flying insects have been a crucial source of inspiration in the design of flapping mechanisms [9, 8, 10, 7]. Dipteran insects use indirect flight muscles that use the thorax to amplify flapping wing motion and operate at the natural frequency of the combined system [8]. In addition to flapping angles, the wings undergo pronation and supination, or rotation, which is key for lift production [11]. Swarms of these flying robotic insects could revolutionize hazardous environment exploration, search and rescue missions, and military applications. For mass production, these vehicles must have reliable and repeatable fabrication processes that define flapping wing mechanisms with microscale features and produce large flapping amplitudes ($> 40°$) at frequencies in the range of many insects (35-100 Hz) [12].

This research focuses on the subsystem of flapping wing mechanisms, including the actuator, amplification mechanism, and wing; the interested reader is directed to reviews of state-of-the-art energy storage, power electronics, sensing, and other payload requirements for NAV/PAVs [13, 14, 15]. The following section presents background and comparison on the state of the art in flapping wing actuators and mechanisms.

1.1 Background of Flapping Wing Mechanisms

1.1.1 Literature Review

At the MAV scale, many fabrication and actuation methods are similar to the *Delfly Micro* from the Delft Univerisity of Technology. This 10 *cm* wingspan MAV is hand built using carbon rods, balsa wood, Mylar foil, and powered by a DC electric motor coupled to a gearbox and linkage mechanism using conventional pin joints[16]. Coupled to a MAV scale motor and gearbox, Pornsin-Sirirak et al. microfabricate 7 *cm* Ti-alloy and parylene C wings using wet etching[17]. AeroEnvironment has recently fabricated the "Nano Hummingbird" which is capable of sustained flight and reconnaissance [18].

Wood et al.[19] have developed the Smart Composite Microstructure (SCM) process where carbon fiber and polyimide layers are laser micromachined and folded to form compliant mechanisms, enabling fabrication and assembly of the Harvard Microrobotic Fly (HMF), a 60 mg, 3-cm wingspan PAV that uses a compliant flapping wing transmission to create large wing angles from piezoelectric bimorph displacement[8]. Successful tethered and externally powered flight of the HMF has shown that piezoelectric actuation with compliant mechanism amplification is suitable for PAV flight. Using MEMS fabrication, Bronson et al.[20] fabricate the smallest NAV in the literature, using PZT thin film actuators directly coupled to a 2.5 mm $SiO_2/Si_3N_4/Ti$-Au wing that produces large flapping angle at resonance. Bao[21] et al. microfabricated a electromagnetically powered flapping wing NAV from multiple layers of SU-8 photoresist.

Many actuation methods exist in the design space of flapping wing MAVs/NAVs: rubber bands[22], reciprocal chemical muscles[23], shape memory alloys[24, 25], electromagnetic actuators[10], electromagnetic motors[6, 7, 26, 27, 28] and piezoelectric actuators[8, 29, 30, 31]. Electromagnetic motors have been the popular choice for larger scale mechanisms [17, 9]. For PAVs, linear electromagnetic actuation [21] and bulk PZT bimorph actuators [8], and thin film PZT unimorph actuators [20] have been used.

Wing rotation is crucial for insect flight and has been extensively studied by biologists and engineers [11, 32, 33, 34]. To produce aerodynamic forces sufficient for flight, insects have large flapping angles ($> 40°$), high flapping frequencies ($> 40Hz$), and wing twist, or rotation, at proper times during the flapping cycle [12]. Many insects do not use significant muscle power in rotating their wings, but aerodynamic and inertial forces cause passive wing rotation [11]. Many computational fluid dynamic studies have been conducted regarding the complex fluid structure interaction on wing rotation and flexibility [35, 36]. In miniature air vehicle design, wing rotation has been achieved by direct actuation [29], elastody-

namic tuning [30], and aerodynamic loading [8]. From a vehicle design standpoint, achieving wing rotation passively is preferred for reduced system mass, complexity, and power load. Designing this type of vehicle requires accurate modeling of aerodynamic and inertial loads on the wing during the flapping cycle.

Recently, engineers have used quasi-steady aerodynamic models using the blade element method to elucidate aerodynamic forces and moments acting upon the wing [33]. Nonlinear analytical models have been created which also describe flapping and rotation dynamics including NAV flapping mechanisms and actuators [37]. Although the NAV system dynamics are nonlinear, linear systems analysis allow a wide variety of design tools and have shown to be accurate over a large operating region [38].

1.1.2 Component Selection

The insect flight apparatus consists of three major components: the flight muscle, thorax, and wing. Flight muscles in insects such as flies, bees, wasps, and beetles deform the thorax amplifying the limited muscle contraction into large flapping angles [39]. For pico air vehicle design, the selection of the actuator, or flight muscle, determines the type of amplification mechanism, or thorax, required for the most effective flapping wing mechanism.

Flapping wing mechanism actuators provide either linear or angular displacement which must be converted to large flapping angles. Electric motors are most commonly used for rotary motion input with gearbox and four bar mechanism amplificiation using conventional pin joints. At the PAV scale, the gearbox becomes difficult to fabricate in an integrated way, and the pin joints show increased friction losses. Linear actuators have been used with conventional pin joints [31], compliant mechanisms [30, 40, 8], and with no amplification mechanism [20, 41]. Devices which do not use an amplification mechanism have actuators which attach to the wing itself, and use the length to amplify tip displacement. These type of

actuators do not show promise because no similar type of mechanism is found in biology, and no fabricated device has been shown to produce lift [20, 41]. On the other hand, reduced wear, friction, and backlash, compatibility with MEMS processing techniques and proven PAV application [8] motivate the use of compliant mechanisms.

Table 1.1.1. Qualitative comparison of candidate linear actuator materials adapted from [42]

Actuator Type	Example	Force	Deflection	Bandwidth	Efficiency	Notes
Electromagnetic	linear coil actuator [10]	Medium	Medium	High	Medium	Low operating voltage
Electrostatic	comb drive extender [43]	Low	Low	High	High	High operating voltage
Shape Memory Alloy	artificial muscle wire [24]	Very high	High	Low	Low	Very high energy density
Piezoelectric	bimorph cantilever[44]	Medium	High	High	High	High operating voltage
Thermal	trilayer cantilever [41]	Very high	Medium	Low	Low	Large material selection
Dielectric Elastomer	cantilever [45]	Medium	Very high	Medium	High	Very high operating voltage

Table 1.1.2. Comparison of piezoelectric actuator materials

Material	$E\ (GPa)$	$\rho\ (kg/m^3)$	$d_{31}\ (pC/N)$	k_{31}	Q_m
PZT-4 [1]	78	7600	-122	0.31	400
PZT-5H [1]	64	7500	-265	0.39	65
PZN-PT [46, 47]	15	8310	-1154	0.66	31-40
PMN-PT [46, 47]	14	8060	-1330	0.73	35-44
PVDF [46, 48]	9	1780	20	0.17	13-25

Many types of linear actuators exist that are compatible with compliant amplification mechanisms. To reduce the scope to microrobotics, six candidate actuator technologies were selected for comparison: electromagnetic [10], electrostatic [43], shape memory alloy (SMA) [24], piezoelectric [44], thermal [41], and dielectric elastomers [45]. Table 1.1.1 shows a qualitative comparison of these actuators based on the review and analysis by Karpelson and Wood [42]. The results of this comparison may change based on the specific design of individual actuators, however this is useful in finding fundamental shortcomings and advantages to different actuator methodologies. For PAV flapping mechanisms, electrostatic actuators do not provide the requisite force and deflection, but they may be feasible for 10 mg scale microrobots [49]. Electromagnetic linear actuators are strong candidates, however at PAV geometries and below resistive heat losses dominate electromagnetic force generation, reducing efficiency [50]. SMA actuators have very high energy density and thermal actuators are very powerful, but neither can provide the high flapping frequencies required for small insect flight. Additionally, the mode of operation of these actuators requires Joule heating through electrical current which has reduced efficiency compared with other methods. Electromagnetic, SMA, and thermal actuators are better suited for larger scale applications with larger dimensions and lower flapping frequencies. Dielectric elastomers are very promising actuators for PAV applications, however require voltages an order of magnitude higher than piezoelectric actuators which already suffer from high voltage requirements. Recent development has designed and fabricated PAV scale power electronics suitable for piezoelectric actuators [51]. The piezoelectric effect enjoys many benefits such as favorable scaling, sufficient force and deflection, high bandwidth, and good efficiency at resonance which can be further increased with charge recovery circuitry [52].

Table 1.1.2 shows a number of piezoelectric actuator materials consisting of piezoelectric ceramics, PZT-4 and PZT-5H, single crystal relaxor ferroelectrics,

PZN-PT and PMN-PT, and piezoelectric polymer PVDF. Young's modulus, E, density, ρ, piezoelectric coefficient, d_{31}, electromechanical coupling coefficient, k_{31}, and mechanical quality factor, Q_m are used to compare these materials. Actuator performance is dependent on configuration such as unimorph, bimorph, rolled actuator or multilayer stack, but can be fundamentally compared using material properties. Single crystal relaxor ferroelectric materials have impressive piezoelectric coefficient and electromechanical coupling coefficient, however poor fracture properties have made implementation difficult [44]. PVDF has very small piezoelectric coefficient, requiring very high voltages to achieve similar strains as other piezoelectric materials. Hard piezoelectric ceramics such as PZT-4 have higher mechanical quality factor, linear response, and are better suited for resonance applications. PZT-5H, a soft piezoelectric ceramic, has higher piezoelectric coefficient and electromechanical coupling, but large hysteresis and nonlinearity. Maximizing power output per unit weight is the first figure of merit, making PZT-5H the best piezoelectric material for PAV actuators. For an additional detailed review of piezoelectric materials and actuators, see Appendix A.

Unimorph [53], bimorph [44], and flextensional [54] actuators have been used for PAV applications. Unimorph actuators consist of an active piezoelectric layer (in the case of a bimorph two active layers) and a passive elastic layer which constrains the field induced extension of the active layer causing bending that is amplified by the length of the beam, increasing tip deflection. Flextensional devices include a compliant mechanism to amplify extension of the piezoelectric element based on the geometry of the mechanism. None of these actuators provide enough deflection to flap a wing on their own, and they must have additional amplification for use in PAV mechanisms. The highest force and deflection output per unit weight is achieved using piezoelectric bimorph actuators, especially optimized trapezoidal bimorphs with extensions such as in [44].

The linear displacement of a piezoelectric bimorph such as [44] is below 500 μm

amplitude and requires significant amplification to achieve insect like flapping amplitudes of approximately 45 *deg*. peak to peak or higher. Flextensional methods alone provide little amplification as stated before, whereas compliant mechanisms based on traditional four bar rigid link mechanisms can be designed to provide sufficient amplification for flapping using piezoelectric actuation. Wood [55] and Fearing [40] have designed three dimensional compliant mechanisms with large amplification. Designing the link lengths and amplification is a factor of the individual actuator used and fabrication constraints. Jacobsen [56] discusses in-plane mechanisms which create out-of-plane motion. Creating mechanisms with high amplification in this way can be significantly more difficult, and will be discussed in this report.

1.2 Current Research

This research begins with the design, fabrication, modeling, and experimental testing of the first NAV scale clapping wing mechanism powered by piezoelectric T-beam actuators. The clapping design is motivated by an aerodynamic mechanism called the Weis-Fogh 'clap and fling' utilized by certain butterflies and wasps, in which opposing wings almost touch during part of the flap cycle, spawning vortex structures that increase thrust. Many different clapping wing vehicle designs exist [26, 9, 7, 28, 57], but all four-winged 'X' type clapping designs use a mechanism consisting of electromagnetic motors with gearboxes. The clapping mechanism outlined in this work amplifies the T-beam displacement using miniature revolute joints and hinges spaced a certain distance apart, creating a lever mechanism. The static and dynamic operation of flapping and rotation is characterized using stobe photography and video, and lift is measured using a force transducer coupled with a specially designed apparatus.

Many piezoelectrically actuated flapping wing mechanisms have been designed

and fabricated that are hand assembled and have 3D components [8, 30, 31, 29]. Most MEMS compliant mechanisms operate in-plane with in-plane actuators [58, 59]. Jacobsen *et al.* [56] present designs for lamina emergent mechanisms that are planar mechanisms capable of out of plane motion. This research introduces a simple flapping wing mechanism fabricated monolithically from SUEX dry film, an epoxy based negative photoresist similar to SU-8. The developed fabrication process has fewer steps compared to other methods, does not use precious metals, and greatly reduces processing time and cost. It simultaneously defines the PAV airframe, compliant flapping mechanism, and artificial insect wing using photolithography. Using this process, we designed and fabricated the LionFly, a flapping wing prototype actuated by a PZT-5H bimorph actuator. Rapid prototypes were fabricated with precisely defined features and material properties and geometry that are similar to insects. We present the fabrication process and characterization of SUEX, static and dynamic modeling of the PAV, and experimental results from multiple prototype devices that demonstrate applicability of the developed fabrication process for flapping wing air vehicle applications.

Finally, in miniature air vehicle design, wing rotation has been achieved by direct actuation [29] and elastodynamic [30] and aerodynamic [8] passive tuning. From a vehicle design standpoint, passive wing rotation is preferred for reduced system mass, complexity, and power consumption. Designing a vehicle with passive wing rotation requires accurate modeling, including the complex interplay between the actuator, mechanism kinematics, and wing vibration and aerodynamics during the flapping cycle. This research presents detailed modeling and experimental testing of wing rotation and lift in the LionFly. The goal of this chapter is to understand the flapping and rotation dynamics, and the lift-producing mechanisms in this device. A linear vibrational model is developed and augmented with nonlinear aerodynamic forces using the blade element method. Experimental testing using a laser vibrometer in air and in vacuum is used to characterize small amplitude

flapping and rotation. Strobe photography and high definition image processing is used to measure high amplitude wing trajectories. A lift measurement system using a force transducer is designed and used to measure average lift. Finally, the development of an improved fabrication process that enables thinner flexures and wings is motivated by simulations using the experimentally validated model that predict a lift to weight ratio of one.

1.3 Contribution and Organization of Report

The following are novel contributions in the field of piezoelectric actuators, flapping wing mechanism fabrication, and microfabrication:

1. Fabrication of piezoelectric T-beam actuators

   A novel fabrication process using a high precision dicing saw has been developed to fabricate piezoelectric T-beam acuators at the millimeter scale. The static and dynamic displacement and blocking force of PZT-5H piezoelectric T-beam acuators have been modeled and experimentally validated. The understanding developed in this research can allow piezoelectric T-beam actuators to be used in place of unimorph or bimorph actuators in certain applications.

2. Clapping wing mechanism for NAV applications

   Using T-beam actuators, a novel clapping wing mechansim has been designed and fabricated using miniature revolute joints made from diced medical grade syringes and tungsten pins, and chemically etched stainless steel. This research demonstrates the first piezoelectrically actuated clapping wing vehicle to produce lift.

3. Monolithic multilevel fabrication of SUEX dry film

A novel fabrication process has been developed to monolithically fabricate SUEX dry film. The process exploits the optical transmission properties of SUEX dry film, defining thin flexible regions using 310 nm wavelength and thick rigid regions using 365 nm wavelength UV energy. Low cost and rapid prototypes of compliant mechanisms of arbitrary 2D dimensions and varied thickness can now be fabricated using photolithography.

4. The LionFly, a SUEX flapping wing mechanism

   A novel compliant slider crank mechanism, fabricated monolithically from SUEX, has been developed to provide large flapping and rotation angles. Detailed linear vibrational modeling of the flapping and rotation dynamics are developed and are augmented by nonlinear aerodynamic forces. The model is experimental validated using laser vibrometer measurement, strobe photography and image processing, and lift measurement with a force transducer and apparatus.

The report is organized as follows: Chapter 2 describes the design, fabrication, modeling and experimental testing of the clapping wing mechanism powered by piezoelectric T-beam actuators. Chapter 3 describes the monolithic fabrication of SUEX for use in compliant mechanisms, and the design, fabrication, modeling, and experimental testing of a compliant slider crank mechanism is presented. Chapter 4 presents detailed modeling and experimental testing of flapping and rotation in the LionFly mechanism. Chapter 5 concludes with results from the different flapping wing mechanism analyses.

Chapter 2

Clapping Wing Nano Air Vehicle Actuated By Piezoelectric T-beams

2.1 Introduction

In this chapter, the design, fabrication, modeling, and experimental validation of an NAV scale clapping wing mechanism is presented. Figure 2.1.1 shows a conceptual drawing of the proposed four winged, clapping mechanism for an NAV. A flexure hinge allows passive wing rotation for the clapping wing mechanism. To properly predict and design wing trajectories, analytic models of wing flapping and rotation are derived, including unsteady aerodynamic wing loading corresponding to the low Reynolds numbers flow. The simulated NAV wing trajectories and thrust are validated using the PSNAV prototype.

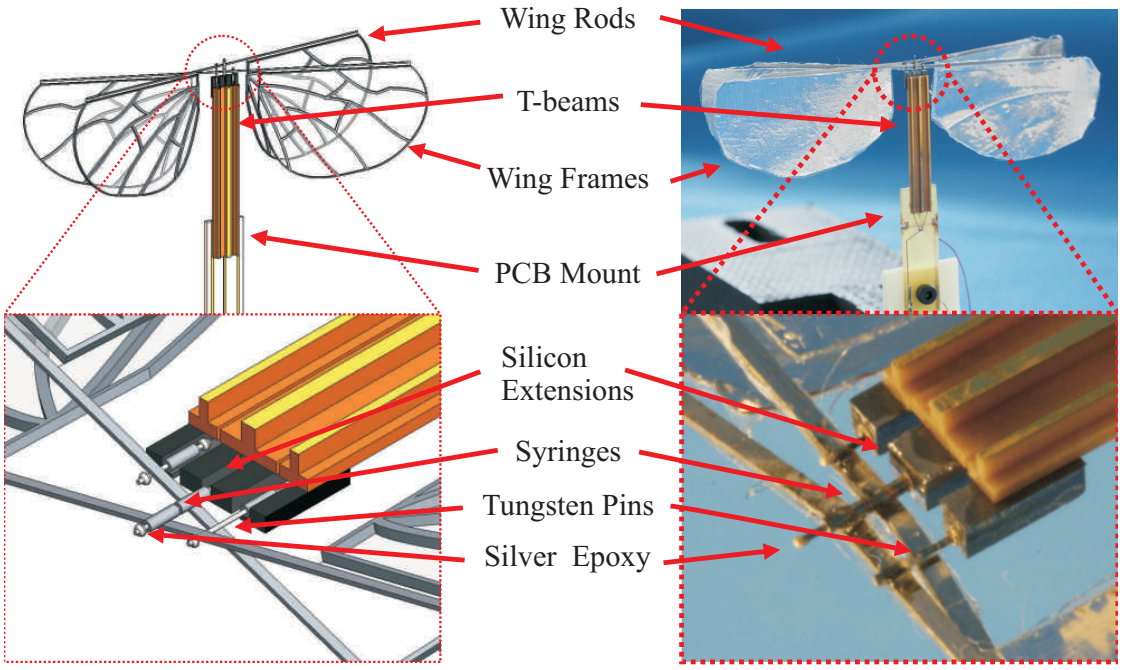

Figure 2.1.1. Conceptual drawing (left) of the PSNAV, a four winged piezoelectrically driven nano air vehicle and fabricated device (right)

2.2 Design and Fabrication

2.2.1 T-Beam Actuators

Unimorph, bimorph, and multilayer actuators have been developed to amplify PZT strain to produce larger transverse deflection in a cantilevered beam. These actuators require process steps that bond separated layers of piezoelectric or passive material that, in bulk piezoelectric form, are difficult to translate to the small scale required of the NAV application. T-beam actuators are monolithically fabricated from a bulk piezoelectric chip and provide in-plane and out-of-plane bending in a cantilevered beam [60]. T-Beam actuators have T-shaped cross sections and, for this application, electrodes on the top and bottom of the structure. Voltage applied between the top and bottom electrodes produces an electric field that concentrates in the web. The flange material is essentially passive and resists contraction.

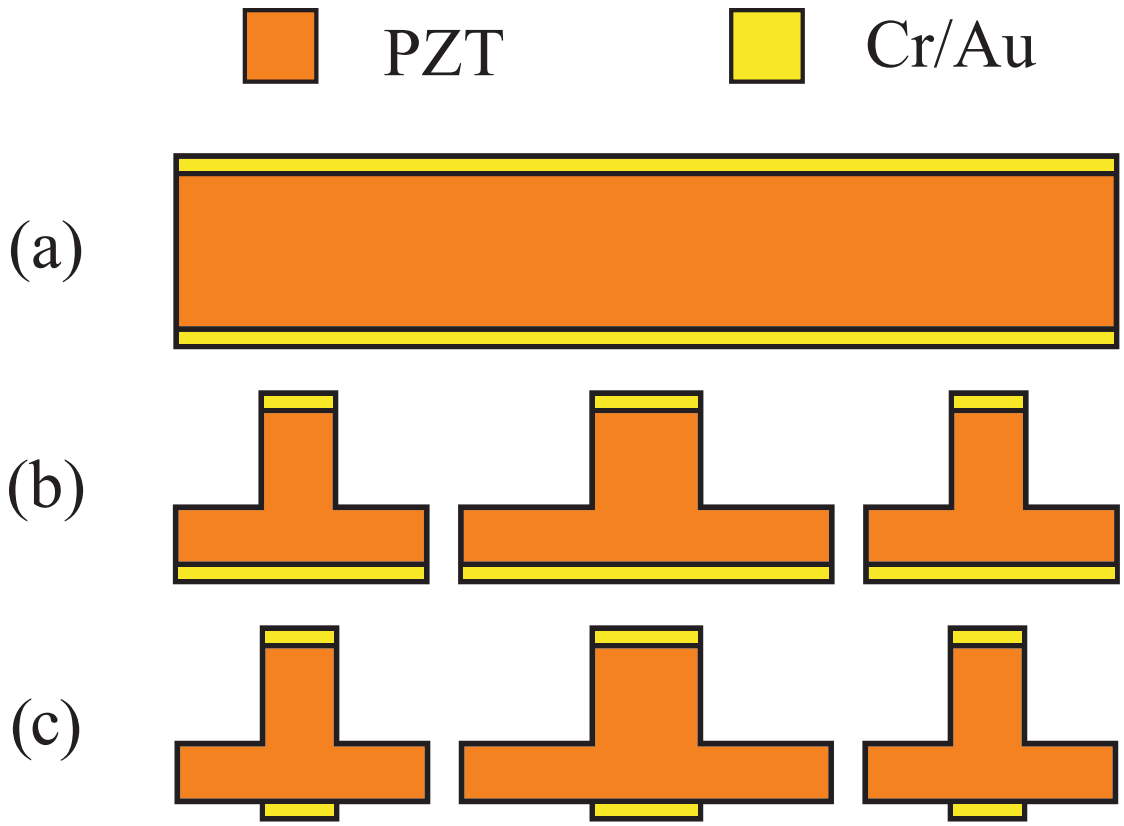

Figure 2.2.1. NAV T-beam fuselage fabrication process: (a) 25.4 mm $\times$25.4 mm $\times$1 mm finely polished, Cr/Au electroded PZT-5H chip (b) machining of PZT using high precision dicing saw (c) patterning of bottom electrode

The web contracts due to the applied field, producing a differential strain across the cross section and constant curvature bending. With a fixed-free boundary condition, a cantilevered T-beam bends out-of-plane to produce relatively large displacement.

These 1 mm thick, 20 mm long actuators produce 200 μm peak to peak free tip displacement and 30 mN blocking force at 1 $V/\mu m$ DC. T-Beams are fabricated using a K&S 980 Series high precision dicing saw with a 100 μm wide nickel blade that is coated in 3-6 μm diamond grit. The fuselage is diced from a 25.4 mm x 25.4 mm x 1 mm finely polished, Cr/Au electroded PZT-5H chip that is bonded to a 2" x 3" glass slide using 1827 photoresist. A 5 μm layer of 1827 spun onto

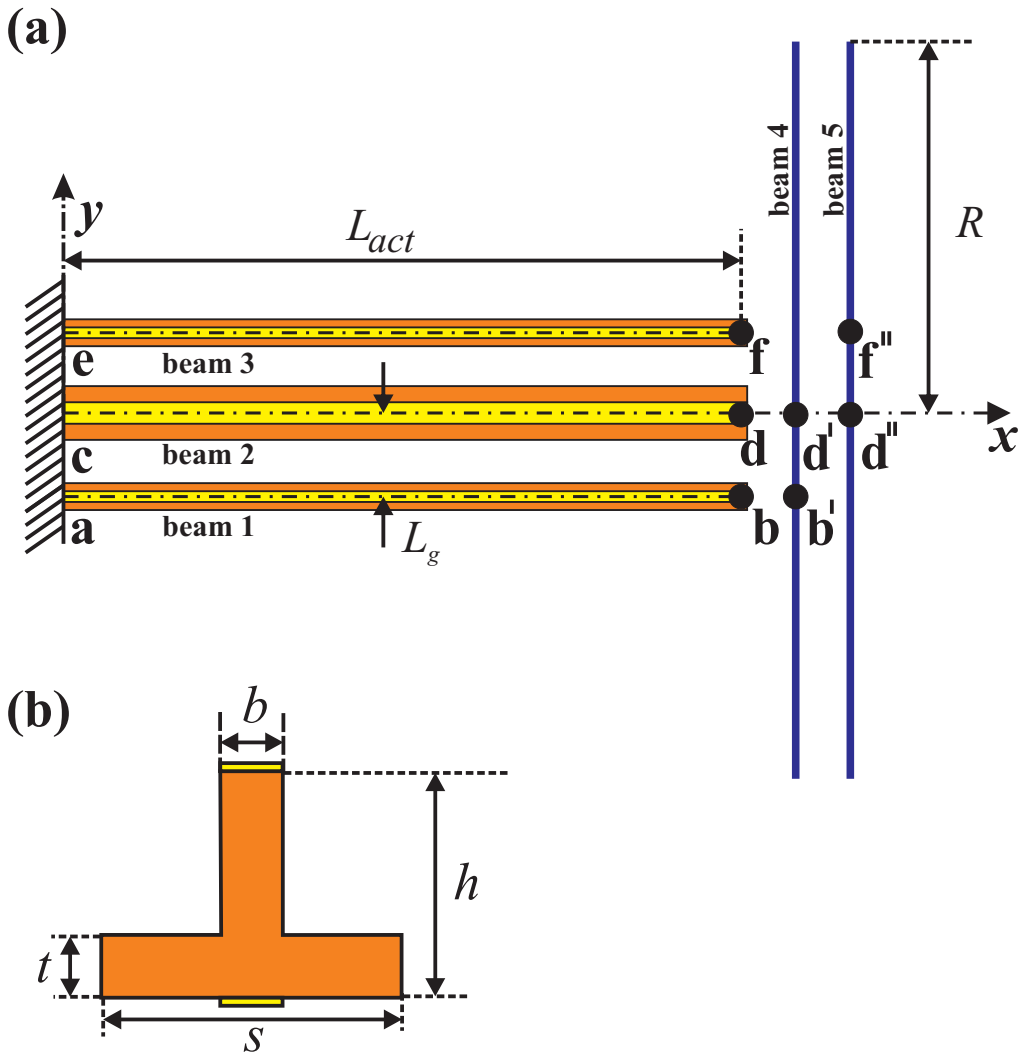

Figure 2.2.2. Schematic diagram of the PSNAV:(a) Top view, (b) Cross-Section of a T-Beam Actuator

the PZT chip protects the T-Beams from particles during dicing. The fabrication process steps are shown in section 2.2. The dicing blade spins at 30 $krpm$ and machines the PZT at a rate of 0.3 mm/s. Multiple passes realize the T cross section, and create a 20 mm x 110 μm air gap in between adjacent T-beams. This leaves approximately 5 mm of PZT material at the base to ensure that the three beams remain parallel and rigidly connected. The center beam in this work

is passive, but could potentially be biased and/or sinusoidally actuated to move the thrust vector and increase flap amplitude. The two outer T-Beams create displacement which is amplified by the hinge and lever system producing large angular rotation. The T-beams are mounted to a custom PCB board using silver epoxy, and wirebonded.

The schematic model of the NAV system is shown in Figure 2.2.2. Beams 1, 2 and 3 are the piezoelectric T-beam actuators and beams 4 and 5 are wing supports. The T-beams are fixed at one end and connected to wing supports at the other end. Beam 4 is connected to beams 2 and 3 with hinges at **b-b'** and **d-d'** and beam 5 is hinged to T-beams 2 and 3 at **d-d"** and **f-f"**. Cantilevered T-beam models developed in a previous paper [60] are used to predict the displacement, u and the blocking force, F. The parameters that define the cross-section are the total height, h, total width, s, web thickness, b, and flange thickness, t as shown in Figure 2.2.2(b).

T-beam displacement increases with the square of the length, L_{act} [60]. The current design has constraints on the length, $L_{act} = 2\ cm$ and total height, $h = 1\ mm$ because it is fabricated from a 25.4 mm x 25.4 mm x 1 mm PZT chip. We constrain $s = 1\ mm$ and 2 mm for the outer and center T-Beams, respectively. The center T-Beam is twice as wide because it is loaded by both outer T-Beams and requires double the stiffness. Web thickness, b, and flange thickness, t, are chosen to optimize the T-beam mechanical energy $E_{MECH} = uF$. Figure 2.2.3 shows the maximum mechanical energy output for a given web thickness and its corresponding optimal flange thickness for the outer T-beams. The optimal flange and web thickness are 331 μm and 245 μm, respectively. Similarly, the optimized central T-beam has $t = 331\ \mu m$ and, $b = 490\ \mu m$.

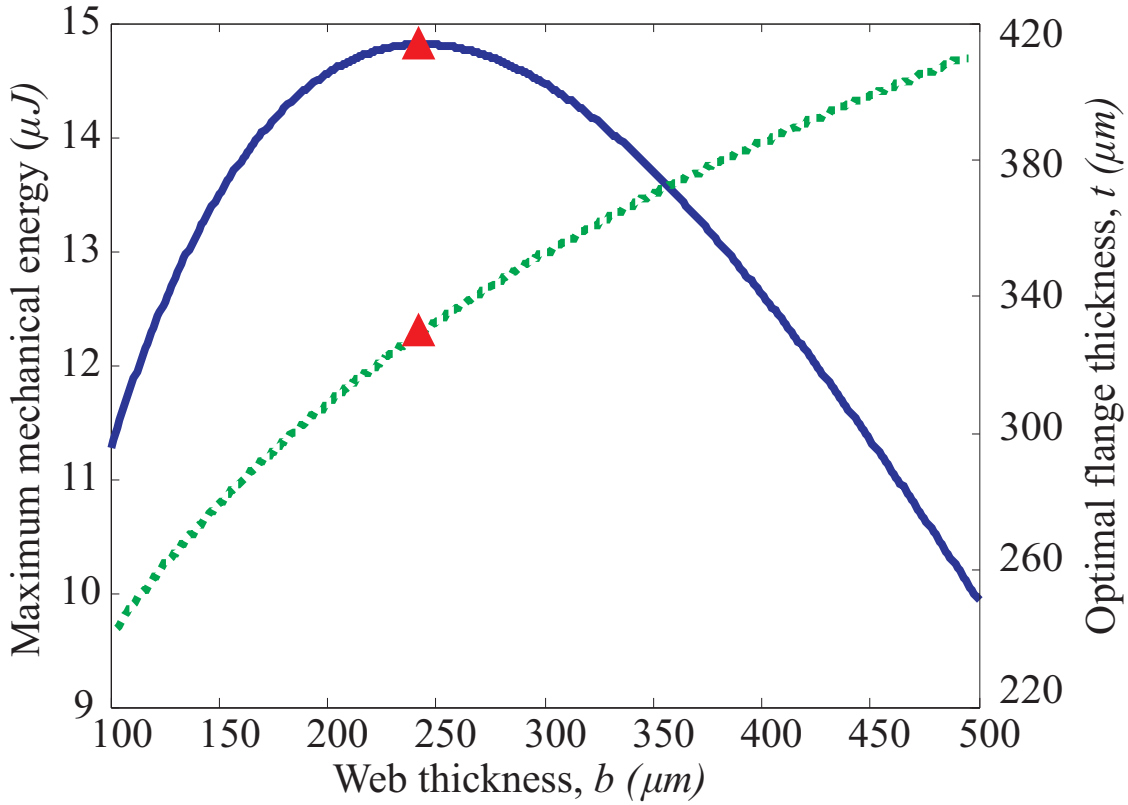

Figure 2.2.3. T-beam maximum mechanical energy, E_{MECH} versus web thickness, b, for optimal flange thickness, t, (blue-solid) and T-beam optimal flange thickness, t, versus web thickness, b, (green-dashed) length, $L_{act} = 2\ cm$, total height, $h = 1\ mm$, and total width, $s = 1\ mm$

2.2.2 Amplification Mechanism

Using piezoelectric actuators, the small linear displacement must be amplified and converted into large angular displacment sufficient for flapping. The clapping mechanism outlined in this work amplifies the T-beam displacement using miniature revolute joints and hinges spaced a certain distance apart, creating a lever mechanism. The revolute joints are fabricated by inserting 3-5 mm long 162.5 μm tungsten pins into 2 mm long 165 μm inside diameter medical syringes housed in 2 mm silicon extensions, which ensure proper alignment and bonding and attach to the free end of the T-beam actuators, shown in Figure 2.2.4.

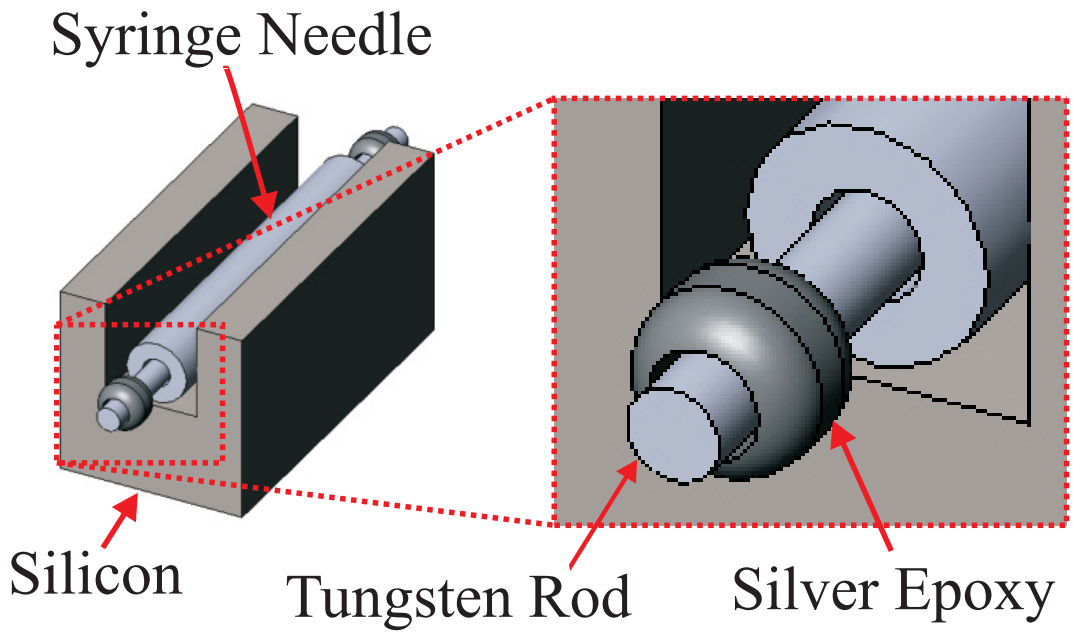

Figure 2.2.4. Drawing of revolute joint made from diced 1 mm thick Silicon, 165 μm inside diameter medical grade syringe needle, 162.5 μm diameter tungsten rod, and silver epoxy beads.

2.2.3 Wing Design

The wing is fabricated by first stretching 12.5 μm thick Mylar sheet onto a frame, then precisely placing a 70 μm thick aluminum foil wingframe onto prescibed location using a linear stage. The wingframe is shaped similar to a fruitfly aerofoil. The wing rod, 200 μm x 600 μm x 6 cm stainless steel, is placed in a similar fashion and connects the two aerofoils forming the leading edge. A 150 μm gap between the leading edge and the wing frame forms the flexure hinge which allows passive wing rotation. Figure 2.2.5 shows a picture of a fabricated wing set, and zoomed in picture of the flexure hinge. A 15° bend is introduced in the wing rod to give clearance for the second wing set. The wingsets and T-beams are set on separate

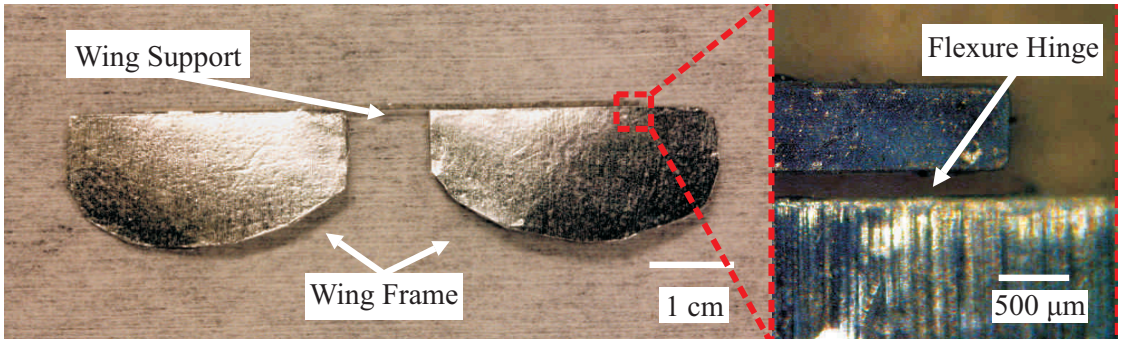

Figure 2.2.5. 100 μm thick aluminum wing frames mounted on 12.5 μm thick mylar wing membrane bonded to 6 cm long stainless steel wing supports

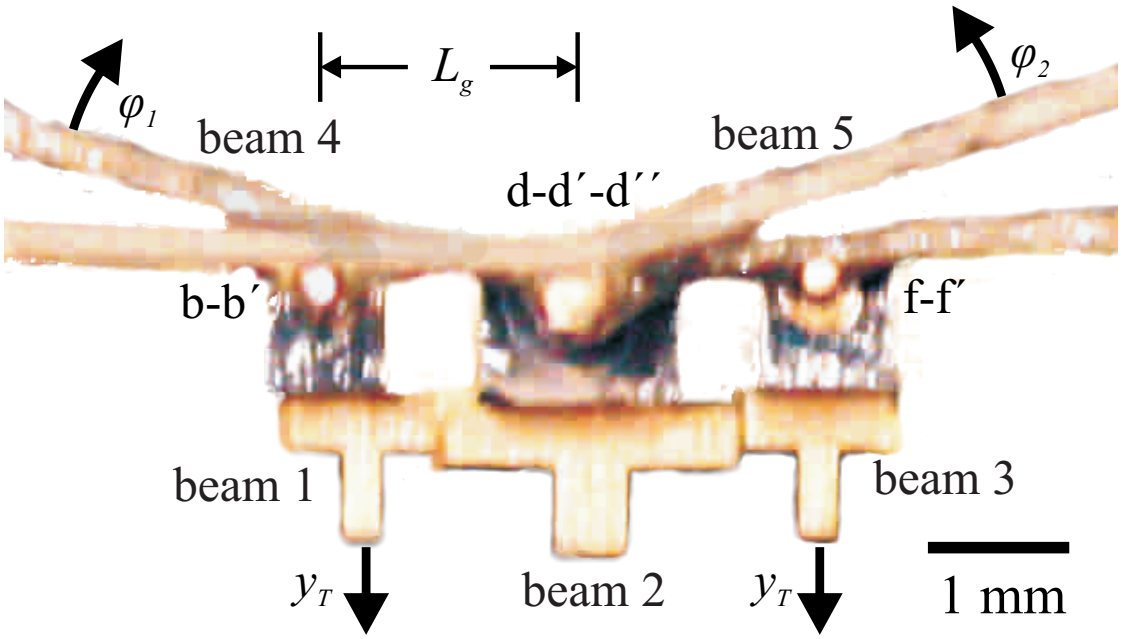

Figure 2.2.6. Schematic of fabricated T-beam fuselage, revolute joints, and wing rod comprising the wing stroke amplification mechanism

micrometer stages and the leading edge of the wing rod is precisely connected to the tungsten pins under a microscope, and bonded using epoxy. An end view of the fabricated T-beams, amplification mechanism, and wing rods is shown in Figure 2.2.6.

2.3 Modeling

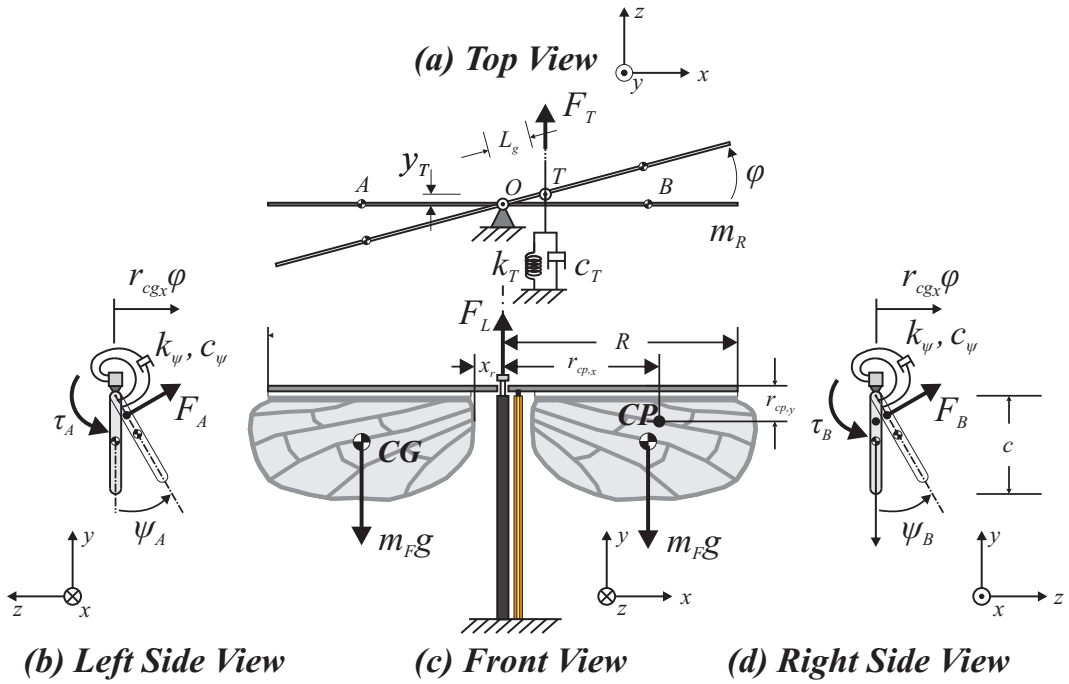

Figure 2.3.1. Schematic of the clapping winged PSNAV system model of one wing set.

Figure 2.3.1 shows a schematic drawing of the clapping wing mechanism. The goal of the structural dynamic modeling is to understand the resonance behavior of the mechanism to aid in future designs. Thus to simplify the order of the model, a single wingset is modeled, and the interactions with the other wingset is neglected. The mechanism is clamped and oriented vertically as in Figure 2.3.1(c). The wing rod is assumed to be rigid and connects the leading edge of each aerofoil to the central T-beam, also assumed to be rigid, at the hinge at the point O. The flapping stroke is constrained to the xy plane and approximated for small angles by $\sin(\phi) \approx \phi = y_T/L_G$ where y_T is the T-beam displacement. The T-beam actuator and pin assembly is modeled as a force, F_T, and linear spring, k_T, hinged to the wing rod at point T. The aerofoils A and B attach to the leading edge by

flexure hinges represented as hinged joints with added torsional springs, k_{ψ_A} and k_{ϕ_B}, respectively. The leading edges of aerofoils A and B undergo displacement by $R_{cg_A}\phi$ and $R_{cg_B}\phi$, respectively. The center of gravity and inertia of the wings are calculated using SolidWorks. The mass of the T-beam actuator is negligible compared to the inertia of the wings.

The sources of losses in the design are in the revolute joints and in the aerodynamic drag experienced by the aerofoils. The lossed in the hinges are modeled as a single damper, c_ϕ applied at the hinge at O. To properly model the unsteady aerodynamics and the fluid structure interation is beyond the scope of this work. Alternatively, a linearized aerodynamic loading effect is simulated upon aerofoils A and B by introducing viscous dampers, c_{ψ_A} and c_{ψ_B}, applied at the hinges A and B, respectively.

Choose as generalized coordinates $q = \begin{bmatrix} \psi_A & \phi & \psi_B \end{bmatrix}^T$, where ψ_A and ψ_B are the wing rotation angles of the left and right wing, respectively, and ϕ is the flapping stroke angle as shown in Figure 2.3.1. Using the small angle approximation, the kinetic and potential energy expressions can be written as

$$\begin{aligned} T &= T_\phi + \sum_{i=A,B} T_{\psi_i} = \frac{1}{2}\dot{\mathbf{q}}^T \mathbf{J} \dot{\mathbf{q}} \\ V &= V_\phi + \sum_{i=A,B} V_{\psi_i} = \frac{1}{2}\mathbf{q}^T \mathbf{K} \mathbf{q} \end{aligned} \tag{2.1}$$

where

$$\mathbf{J} = \begin{bmatrix} J_{\psi,A} & J_{\phi,\psi,A} & 0 \\ J_{\phi,\psi,A} & J_\phi & J_{\phi,\psi,B} \\ 0 & J_{\phi,\psi,B} & J_{\psi,B} \end{bmatrix}, \tag{2.2}$$

$$\mathbf{K} = \begin{bmatrix} k_{\psi_A} & 0 & 0 \\ 0 & k_\phi & 0 \\ 0 & 0 & k_{\psi_B} \end{bmatrix}, \tag{2.3}$$

the terms $J_\phi, J_{\psi,i}, J_{\phi,\psi,i}$ for $i \in \{A, B\}$ are calculated from Solidworks, and

$$k_\phi = k_T L_g^2, \tag{2.4}$$

$$k_{\psi,i} = k_{flex,i} + m_{F,i} g R_{cg,y} \texttt{for } i \in \{A, B\} \tag{2.5}$$

are calculated using parameters from Table 2.3.1. The Solidworks model is calibrated using the measured mass of the wing set. The equations of motion can be written using the Euler-Lagrange formulation, where the Lagrangian

$$L = T - V = \frac{1}{2}\dot{\mathbf{q}}^T \mathbf{J} \dot{\mathbf{q}} - \frac{1}{2}\mathbf{q}^T \mathbf{K} \mathbf{q} \tag{2.6}$$

and Lagrange's Equations

$$\frac{d}{dt}\left(\frac{\partial L}{\partial \dot{\mathbf{q}}}\right) - \frac{\partial L}{\partial \mathbf{q}} = \mathbf{J}\ddot{\mathbf{q}} + \mathbf{K}\mathbf{q} = \mathbf{Q}, \tag{2.7}$$

where the generalized forces are

$$\mathbf{Q} = -\mathbf{C}\dot{\mathbf{q}} + \begin{bmatrix} 0 \\ F_T L_g \\ 0 \end{bmatrix}$$

with viscous damping

$$\mathbf{C} = \begin{bmatrix} c_{\psi_A} & 0 & 0 \\ 0 & c_\phi & 0 \\ 0 & 0 & c_{\psi_B} \end{bmatrix}, \tag{2.8}$$

and $F_T L_g$ is the torque generated from T-beam tip force. Substitution of the

generalized forces, intoEquation 2.7 produces the PSNAV system dynamics

$$\frac{d}{dt}\begin{bmatrix}\mathbf{q}\\ \dot{\mathbf{q}}\end{bmatrix} = \begin{bmatrix}\mathbf{0} & \mathbf{I}\\ \mathbf{J}^{-1}\mathbf{K} & \mathbf{J}^{-1}\mathbf{C}\end{bmatrix}\begin{bmatrix}\mathbf{q}\\ \dot{\mathbf{q}}\end{bmatrix} + \mathbf{J}^{-1}\begin{bmatrix}0\\ \mathbf{Q}_{AF}\end{bmatrix}. \tag{2.9}$$

Table 2.3.1. PSNAV Parameters and Values

Parameter	Description	Value	
R	span of one wing, root to tip	37.5	mm
c	chord of wing	17	mm
L_G	distance from fulcrum to T-beam	1.68	mm
L_{flex}	flexure length	1.5	μm
L_{act}	T-beam length	20.2	mm
L_{pin}	Tungsten pin length	1.63	mm
t_{mylar}	thickness of Mylar	12.5	μm
E_{mylar}	Young's modulus of mylar	4	GPa
E_{PZT5H}	Young's modulus of PZT5H	63	GPa
I_T	T-beam area moment of inertia	0.0371	mm^4
$k_T = \frac{6E_{PZT5H}I_T}{L_{act}^2(2L_{act}+L_{pin})}$	T-beam stiffness	817	$\frac{N}{m}$
ρ_{Al}	density of Aluminum	2700	$\frac{kg}{m^3}$
ρ_{SS}	density of stainless steel	8000	$\frac{kg}{m^3}$
$R_{cg,x}$	aerofoil CG from root, spanwise	17.5	mm
$R_{cg,y}$	aerofoil CG from root, chordwise	8.5	mm
m_F	wing frame mass	116	mg
m_R	wing rod mass	23	mg
$I_{flex} = \frac{w_{flex}t_w^3}{12}$	flexure area moment of inertia	3.3e-6	mm^4
$k_{flex} = \frac{E_{mylar}I_{flex}}{L_{flex}}$	flexure stiffness	0.088	$N \cdot mm$

Figure 2.3.2 shows a cross section of the wing chord illustrating the aerodynamic forces and torques acting upon the wing and the definition of angle of attack, $\alpha = \arctan(v_{y'}/v_{x'})$, which is crucial for lift production. First, the translational velocity of the wing is transformed into the wing reference frame by the rotation

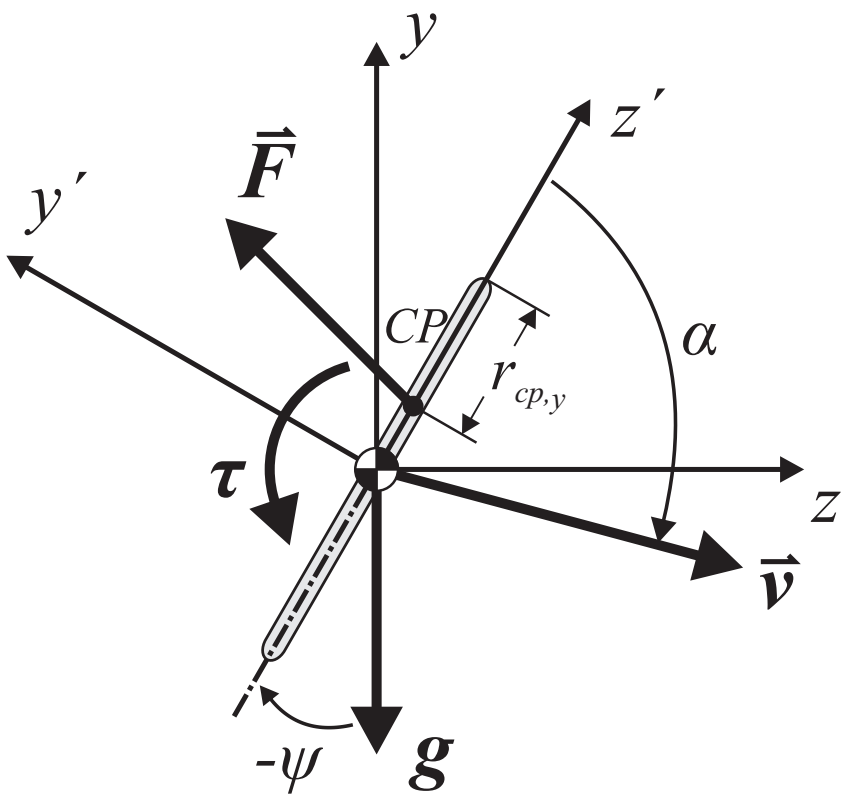

Figure 2.3.2. Aerodynamic forces on the wings(adapted from Andersen et. al. [61]).

matrix

$$\mathbf{R}(\psi) = \begin{bmatrix} -\sin(\psi) & \cos(\psi) \\ -\cos(\psi) & -\sin(\psi) \end{bmatrix}. \tag{2.10}$$

Following the approach in [61], the viscous torque

$$\tau^{\nu} = \frac{1}{64} R \rho_{air} C(\pi/2) c^4 |\dot{\psi}| \dot{\psi}$$

and forces

$$F_{x'} = -\rho_{air} \Gamma v_{y'} - F^{\nu}_{x'} \tag{2.11}$$

$$F_{y'} = \rho_{air}\Gamma v_{x'} - F^{\nu}_{y'} \tag{2.12}$$

act on one aerofoil in the wing reference frame where the circulation around the aerofoil is

$$\Gamma = -\frac{1}{2}C_{Tr}Rc|\mathbf{v}|sin(2\alpha) + \frac{1}{2}C_{R}Rc^2\dot{\psi},$$

and the viscous drag force is

$$\mathbf{F}^{\nu\prime} = \frac{1}{2}\rho_{air}Rc(C_D(0)\cos^2(\alpha) + C_D(\frac{\pi}{2})\sin^2(\alpha))|\mathbf{v}|\mathbf{v}'.$$

The drag coefficient C_D is evaluated at $\alpha = 0$ and $\alpha = \pi/2$ using data from [61]. The torque and force, transformed back into the inertial reference frame, are

$$\tau = \frac{Rc}{4}\rho_{air}\Gamma|\mathbf{v}| - \tau^{\nu}, \tag{2.13}$$

$$\mathbf{F} = \mathbf{R}^{-1}(\psi)\mathbf{F}', \tag{2.14}$$

respectively. The inertial forces and torques in Equation 2.13) act at the center of pressure, a quarter chord from the leading edge of the aerofoil. The virtual work associated with the aerodynamic loads and the T-beam force, F_T, is

$$\delta W = F_T\delta y_T + \sum_{i=A,B}\{\tau_i\delta\psi_i + F_{i,x}\delta r_{i,x} + F_{i,y}\delta r_{i,y}\} \tag{2.15}$$

$$= (F_T L_G + \sum_{i=A,B} F_{i,x}R_{cp,x})\delta\phi + \sum_{i=A,B}\left\{\left(\tau_i - F_{i,y'}\frac{c}{4}\right)\delta\psi_i\right\} \tag{2.16}$$

$$= Q_\phi\delta\phi + \sum_{i=A,B} Q_{\psi_i}\delta\psi_i \tag{2.17}$$

Substitution of the generalized aerodynamic forces, $\mathbf{Q}_{AF} = [Q_{\psi_A}, Q_\phi, Q_{\psi_B}]^T$ into Eq. **??** produces the PSNAV system dynamics

2.4 Experimental Testing and Results

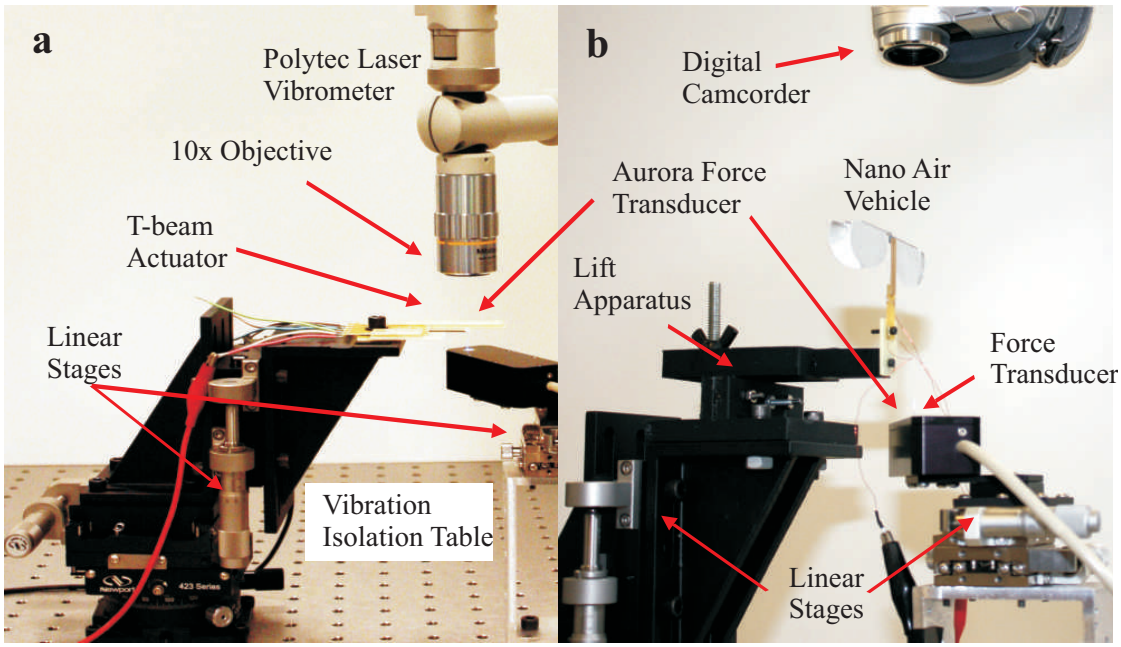

Figure 2.4.1. Photograph of experimental test setup for (a) T-beam actuators (b) nano air vehicle

A photograph of the experimental setup for actuator measurement is shown in Figure 2.4.1(a). An input signal is generated in LabVIEW and amplified using a Trek Model 609E-6 high voltage amplifier which can provide 10kV max voltage up to 6kHz. A Polytec Laser Vibrometer® with a 10X objective focuses a 20 μm laser onto the gold web electrode of a T-Beam and returns displacement signals to LabVIEW. A The clapping wing mechanism is mounted vertically, and Newport XYZ linear stages allow precision positioning. The wing trajectories of the PSNAV are measured using strobed photography. The PSNAV is fixed to an ABS plastic lift apparatus that uses a razor blade fulcrum that preloads and transmits dynamic loads to an Aurora Scientific, Inc. 402A force transducer with 10 μN resolution and 2kHz bandwidth. At least 50 cycles are measured to obtain steady-state lift.

The T-Beam actuators are tested off-resonance, quasi-statically at 1 Hz.Figure

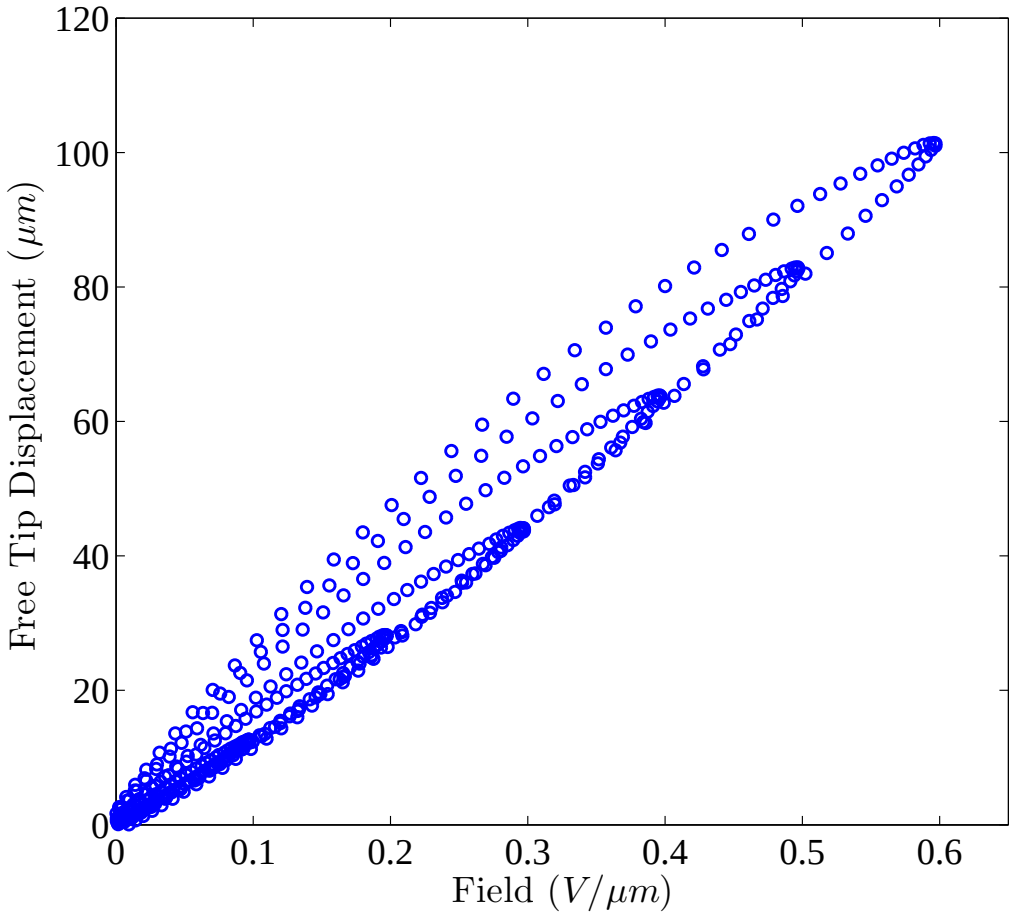

Figure 2.4.2. Quasi-static free tip displacement of a T-beam actuator

2.4.2 shows the free tip displacement and blocking force response of the left and right T-Beam under varying peak applied fields. The actuators are designed to provide large displacement, so the hysteresis associated with relatively high strain PZT-5H is a minor drawback. During blocking force measurements the compliance of the PCB board was apparent. The measured blocking force is significantly less than the true blocking force of the T-beam actuator due to bending of the PCB board seen in figure 2.4.3. Ideally, the displacement at the base of the T-beam would be zero during blocked force measurement.

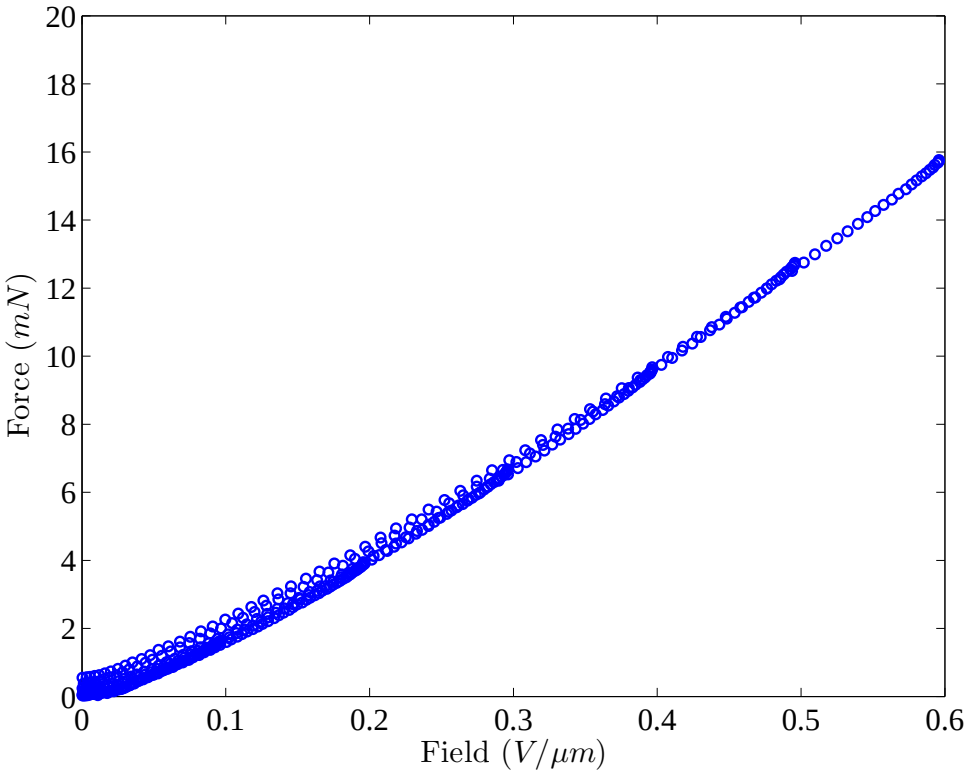

Figure 2.4.3. Measured force of T-beam actuator. Actual blocking force is larger due to compliance in mounting.

A field of 0.7 $V/\mu m$ amplitude with 0.1 $V/\mu m$ DC bias is applied to the fabricated prototype PSNAV from DC to 30 Hz. Two resonance modes were observed near 9.5 Hz and 25.5 Hz. Figure 2.4.4 shows a photograph of the PSNAV flapping stroke motion in the open and closed position, showing ˜$11 - 14^o$ peak to peak per aerofoil at 9.5 Hz that produces near clapping (Figure 2.4.4(a)) and a gap of around 30^o (Figure 2.4.4(b)) at different times during the flapping cycle. Figure 2.4.5 shows images at five stages of the flapping cycle at 9.5 Hz. The left set of wings passively rotate from -33^o to 21^o during the flapping cycle. The right set of wings, however, show substantially less rotation and translation. This is due to the slight differences in resonance frequencies between the two sets of wings. Figure 2.4 show the flapping and rotation amplitudes versus frequency. The right

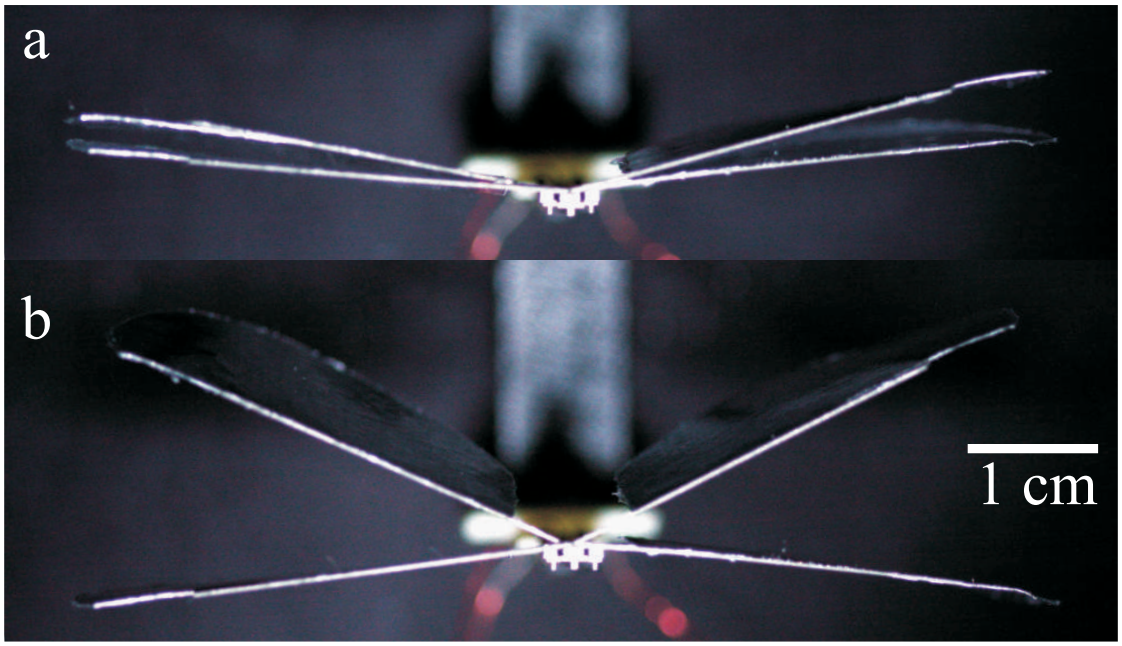

Figure 2.4.4. LionFly in the closed(a) and open(b) position showing 30 *deg.* of stroke from DC to 9.5Hz using 0.7 $V/\mu m$ amplitude and 0.1 $V/\mu m$ DC bias

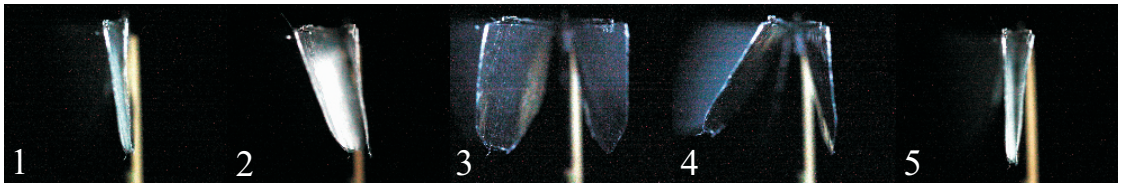

Figure 2.4.5. Strobed images of one period of wing rotation actuated at 9Hz using 0.7 $V/\mu m$ amplitude and 0.1 $V/\mu m$ DC bias

pair of wings are slightly off-resonance so the amplitudes are smaller. The resonance mode at 25.5 Hz produces ˜8^o peak to peak flapping angle and ˜24^o rotation angle. The response of $\phi_{A,B}$ is nearly 90^o out of phase with θ at 9.5 Hz and 180^o at 25.5 Hz. Figure 2.4.7 shows the experimentally measured thrust versus frequency at 0.1 V/um bias and 0.7 V/um amplitude. The peaks at 9.5 Hz and 25.5 Hz are clearly seen.

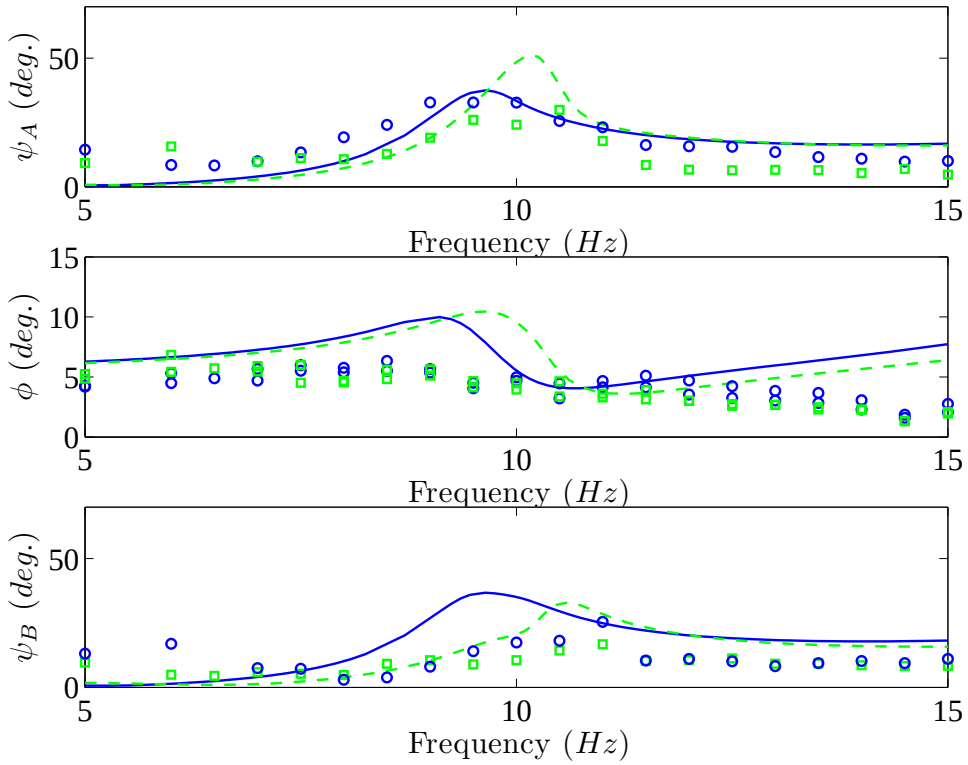

Figure 2.4.6. Stroboscopically photographed, image processed experimental data and simulated wing A rotation ψ_A (top), flapping ϕ (middle), and wing B rotation, ψ_B (bottom) versus frequency at applied field of 0.7 $V/\mu m$ and 0.1 $V/\mu m$ DC bias: experimental data for wing set 1 (blue circles), simulated data for wing set 1 (blue solid), experimental data for wing set 2 (green squares), and simulated data for wing set 2 (green dashed).

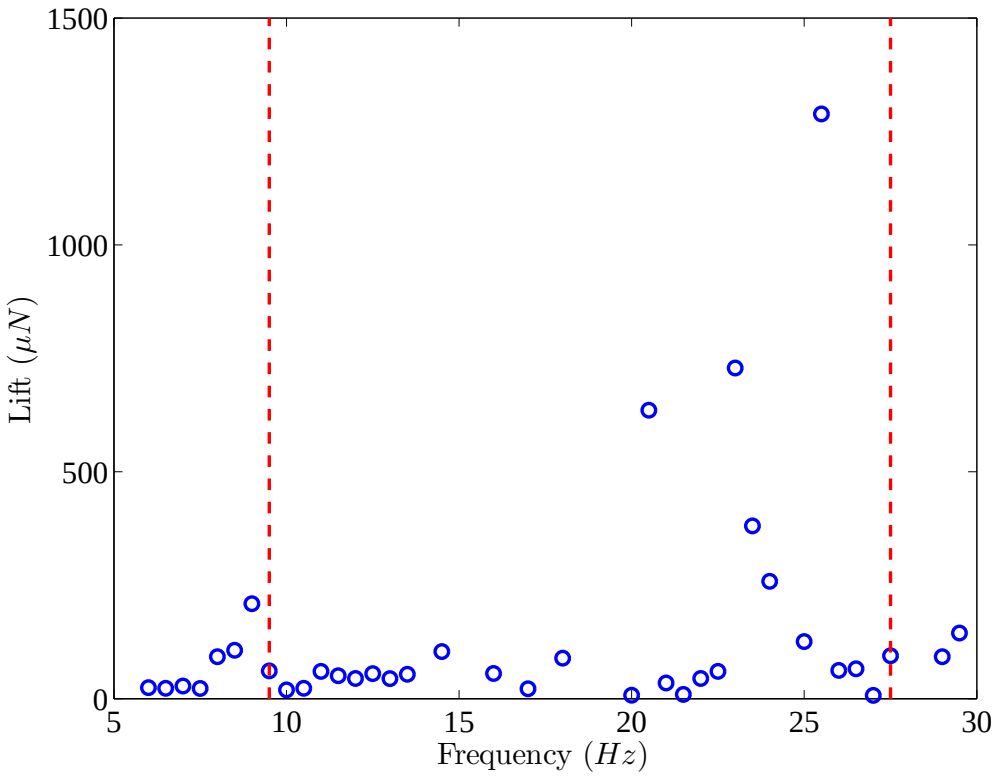

Figure 2.4.7. Average lift force of NAV versus frequency under applied field of 0.7 $V/\mu m$ and 0.1 $V/\mu m$ DC bias. Resonance frequencies of the two modes are highlighted (red dashed).

Chapter 3

Monolithic SUEX Flapping Wing Mechanisms for Pico Air Vehicle Applications

3.1 Introduction

This chapter introduces a simple flapping wing mechanism fabricated monolithically from SUEX dry film, an epoxy based negative photoresist similar to SU-8. We present the fabrication process and characterization of SUEX, static and dynamic modeling of the PAV, and experimental results from multiple prototype devices that demonstrate applicability of the developed fabrication process for flapping wing air vehicle applications.

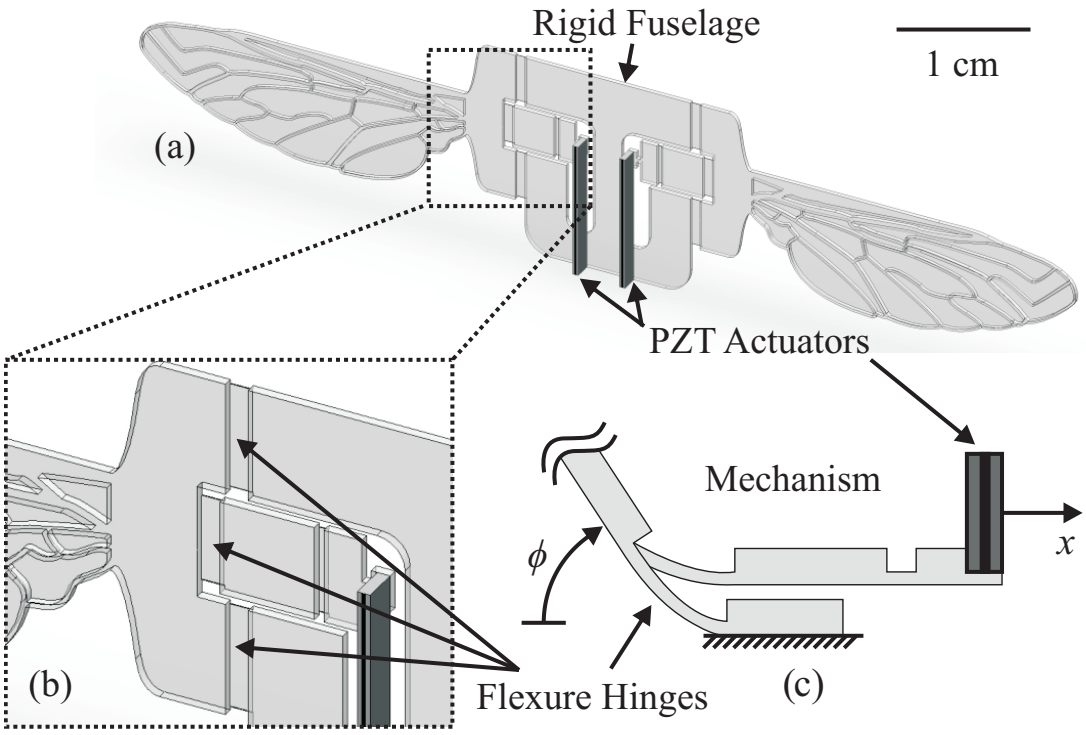

Figure 3.1.1. Conceptual drawing of the Penn State LionFly: (a) Isometric view, (b) zoomed inset of compliant mechanism and piezoelectric bimorph actuator, and (c) operation of compliant flapping wing mechanism with actuator displacement input, x, and flapping output, ϕ.

3.2 Material Choice and Fabrication

3.2.1 Material Choice for Compliant Mechanisms

Compliant mechanisms typically consist of a system of rigid links connected by flexible members designed to bend within a certain range of motion. These mechanisms can be fabricated from multiple layers bonded together or monolithically from a single layer with an etched flexible region. The use of multiple layers can increase fabrication complexity and introduce problems such as delamination. Monolithic fabrication is simpler, but it is important to select a material that can be fabricated to the desired geometry with suitable material properties. Figure 3.2.1 shows a typical flexure hinge under normal operation, where one rigid

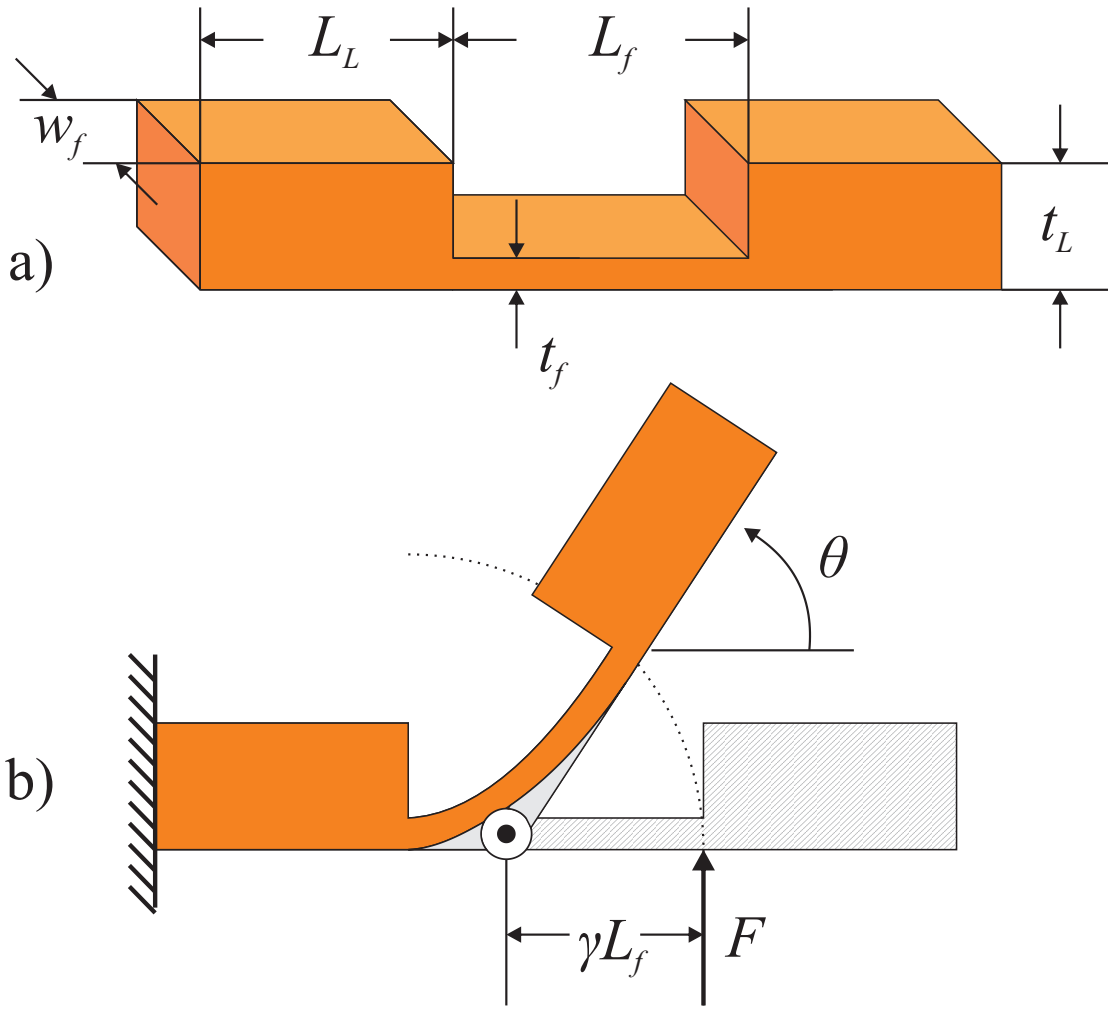

Figure 3.2.1. Schematic of a flexure hinge: a) dimensions, b) typical operation

link is fixed, and the other is free and has a force perpendicular to the tip of the flexure region. The bending stiffness of the rigid portion is much larger than the bending stiffness of the flexure region ($EI_L >> EI_f$). This is achieved by reducing the thickness of the flexure region, in which a reduction by a factor of 5 creates a bending stiffness ratio of 125 for a monolithic flexure hinge because the moment of inertia for a rectangular cross section, $I = wt^3/12$. The maximum bending angle

for a short rotational flexure can be determined by [19]

$$\theta_{max} = \frac{2\sigma_y L_f}{E_f t_f} \tag{3.1}$$

where σ_y is the yield strength and E_f is the Young's modulus of the material. The factor σ_y/E_f determines the maximum strain before yielding, ϵ_y, of a material, independent of geometry. Table 3.2.1 shows many candidate flexure hinge materials and their properties ranked by yield strain. Ranking high are polymer materials such as polyimide, and low are metals such as steel and polysilicon. Single crystal silicon is an excellent material for compliant mechanisms in theory. However in practice, sensitivity to crystallographic defects and surface imperfections make single crystal silicon susceptable to crack propagation [62] and incapable of handling large loads [17].

SU-8, a negative tone, epoxy based, near UV, thick photoresist, has traditionally been used for high aspect ratio applications such as electroplating masks [63], deep reactive ion etching masks [64], and microfluidics [65]. Its use as a structural material has been shown in applications such as compliant microgrippers [59] and recently in NAV applications [21, 10]. SU-8 is typically spin coated onto a Si wafer, soft-baked (65-95 °C), exposed to 365 nm UV light, post-exposure baked (PEB) (65-95 °C), developed in PGMEA, and optionally hard baked (HB) (150-200 °C). Multiple layers must be spun after the initial layer soft bake step to increase overall thickness. SUEX, by DJ DevCorp, Inc. has nearly identical characteristics to SU-8 [66], but is available as a dry film in thicknesses up to 1 mm. Post soft bake, the processing is nearly identical to SU-8, but SUEX can be processed as a substrate, with the exception of 50 μm PET protective layers that are easily removed. Low density and fabrication advantages make SUEX an excellent material for PAV applications, despite not ranking first in yield strain in Table 3.2.1.

Table 3.2.1. Table of candidate materials for flexure Hinges

Material	ϵ_y (%)	E (GPa)	σ_y (MPa)	ρ (kg/m^3)	Source
PI-2525	5.35	2.4	128.5	1420	[67]
Si[a]	3.68	190.0	7000.0	2300	[62]
Si_3N_4[a]	3.64	385.0	14000.0	3100	[62]
SUEX	3.07	2.8	86.0	1190	[68]
PET	2.87	2.8	79.3	1356	[69]
PP	2.43	1.4	34.0	855	[70]
Parylene C	1.99	2.8	55.0	1289	[71]
Nylon-66	1.96	2.8	55.0	1150	[70]
Ti-13[b]	1.03	114.0	1170.0	4820	[70]
Steel 4140[c]	0.79	207.0	1641.0	7750	[70]
Al 7075[b]	0.70	71.7	503.0	2795	[70]
poly-Si	0.55	169.0	930.0	2329	[70]

[a]single crystal, [b]heat treated, [c]Q&T400

3.2.2 Monolithic Multilevel Fabrication of SUEX

Similar to other negative photoresists [72, 73], SUEX has unique optical properties where absorption is much higher at shorter wavelengths, allowing only partial penetration of thickness. At higher wavelengths (above 365 nm) the material is transparent, allowing ultra thick and high aspect ratio features. Figure 3.2.2 shows the optical transmission spectrum of unexposed SUEX film, taken using a Perkin Elmer Lambda 950 UV/Vis Spectrometer. The film is nearly transparent above 365 nm, but blocks wavelengths below 350 nm, enabling definition of thin flexible, full thickness, and through etched regions. We exploit this phenomenon to define flexure hinges using UV energy at 310 nm for thin flexible regions, and 365 nm for thick rigid regions. Figure 3.2.3 shows the fabrication process: (a) 250 μm thick SUEX comes sandwiched between two 50 micron PET layers for support. In (b) the top layer is removed, and the first mask defines the thin flexure and wing membrane region with the thickness controlled by the exposure dose at 310 nm wavelength. Figure 3.2.3 (c) shows the thick or rigid link regions of the LionFly defined by exposure at 365 nm using the second mask. The post exposure bake

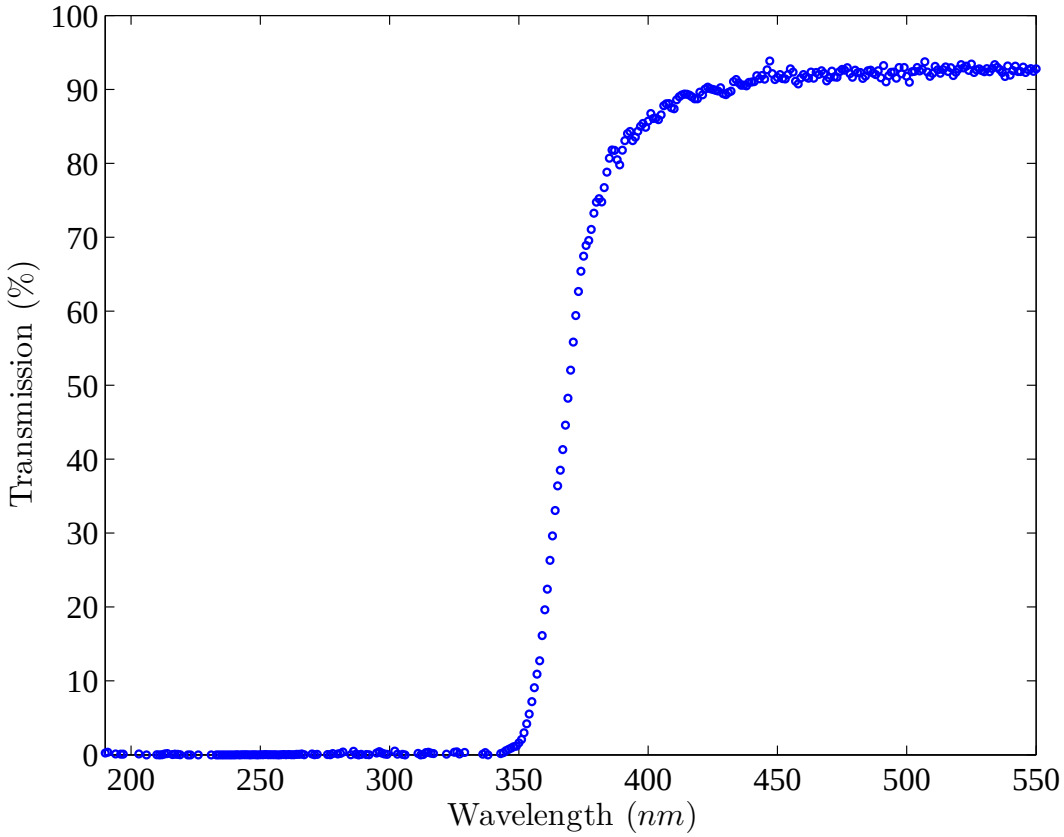

Figure 3.2.2. Optical transmission spectrum of SUEX

(PEB) (d), performed at 65°C for 30 minutes on a hotplate, is crucial for cross linking of SUEX. The wafer is removed and allowed to cool for an additional half hour. The bottom PET layer is removed, and the SUEX is developed in a mesh cage in PGMEA (e) for one hour at room temperature with light agitation. The devices are removed from the mesh, blow dried with N_2, and put in a vacuum oven at 50 °C for a half hour to dry. The devices at this point are ready for mounting with total clean room processing time approximately three hours.

Multiple tests at varying doses were conducted to characterize the effect of 310 nm exposure dose on flexure thickness. The UV exposure wavelength can be controlled by installing different filter sets in mask aligners with broadband light intensity. In this work, two mask aligners with different UV intensity at 310, 365

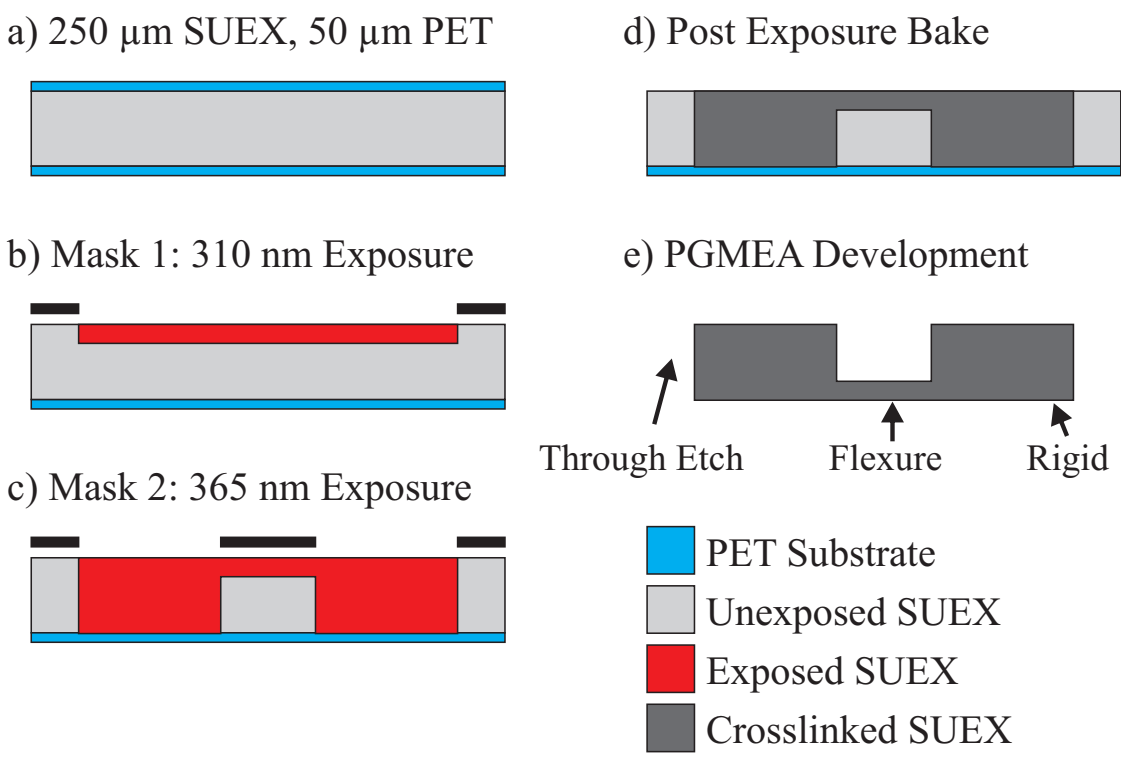

Figure 3.2.3. Fabrication of SUEX structure: (a) initial SUEX substrate between two 50 μm PET layers, (b) 310 nm exposure dose of 500 mJ/cm^2 for 25 μm flexure layer, (c) 365 nm exposure dose of 1350 mJ/cm^2 for 250 μm rigid layer, (d) post exposure bake (65°for 30 min) to activate cross linking in SUEX, (e) development in PGMEA for 1 hr with light agitation releases structures

and 405 nm wavelength were used. The Karl Suss MJB-3 contact aligner was used for flexure definition and has average light intensity of 2.9 mW/cm^2 at 310 nm, near zero at 365 nm, and 1.15 mW/cm^2 at 405 nm. The EVG 620 mask aligner was used for rigid link definition and has average light intensity of 4.5 mW/cm^2 at 310 nm, 13.96 mW/cm^2 at 365 nm, and 26.14 mW/cm^2 at 405 nm. Step height measurement was conducted using a Zygo® NewView 100C optical profilometer, and total thickness measurements using an optical microscope. Figure 3.2.4 shows the flexure thickness begins to saturate at approximately 70±5 μm at doses beyond 1 J/cm^2, and is nearly linear between 0.25-0.75 J/cm^2. Figure 3.2.5 shows a cross section of a fabricated flexure hinge from SUEX. It should be noted that in this

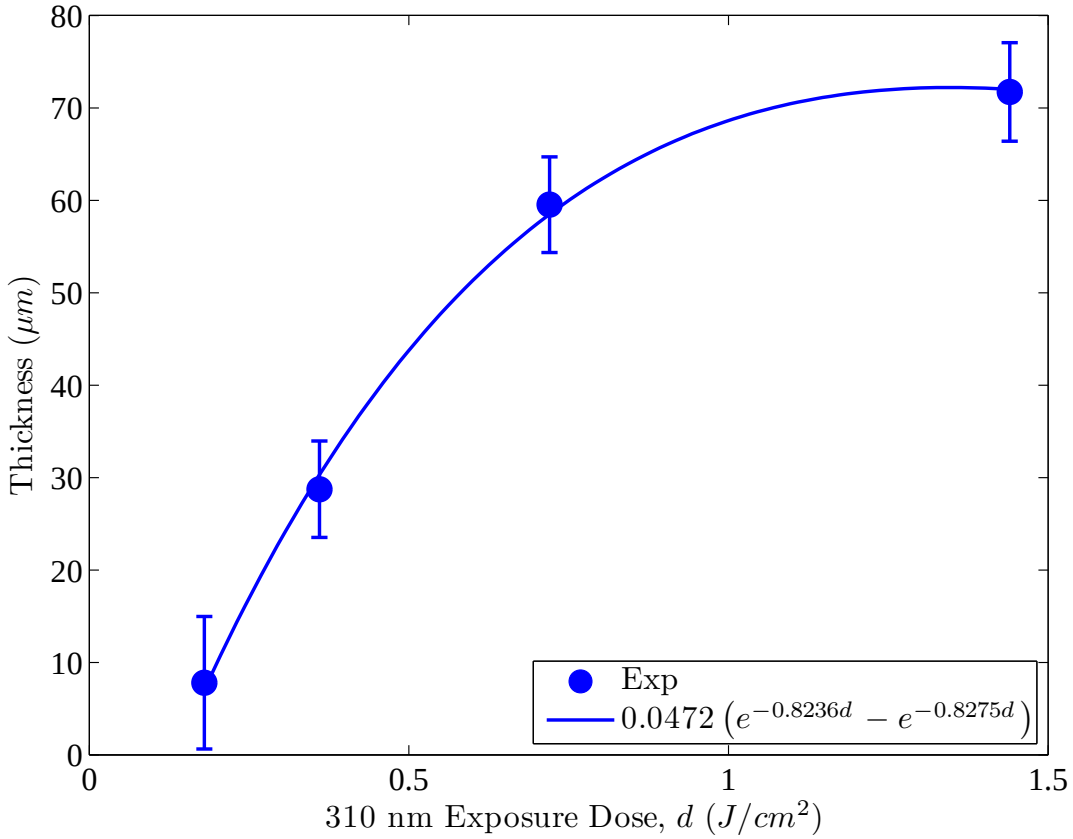

Figure 3.2.4. Flexure thickness versus 310 nm exposure dose

work only two thickness levels are chosen, however this process can be extended to have multiple levels with additional masks defining each level with increasing 310 nm exposure dose.

3.2.3 Actuator Selection

In this work, we use high performance PZT-5H bimorphs from Piezo Systems, Inc.®, comprised of a 115 μm thick composite shim material sandwiched between two 127 μm thick PZT-5H piezoelectric layers. The material is diced into smaller 2 mm $\times$ 10 mm bimorphs using a K&S Model 980 dicing saw. Typical actuators weigh 55 mg, produce $\pm$ 100μm tip displacement and 45 mN blocking force at

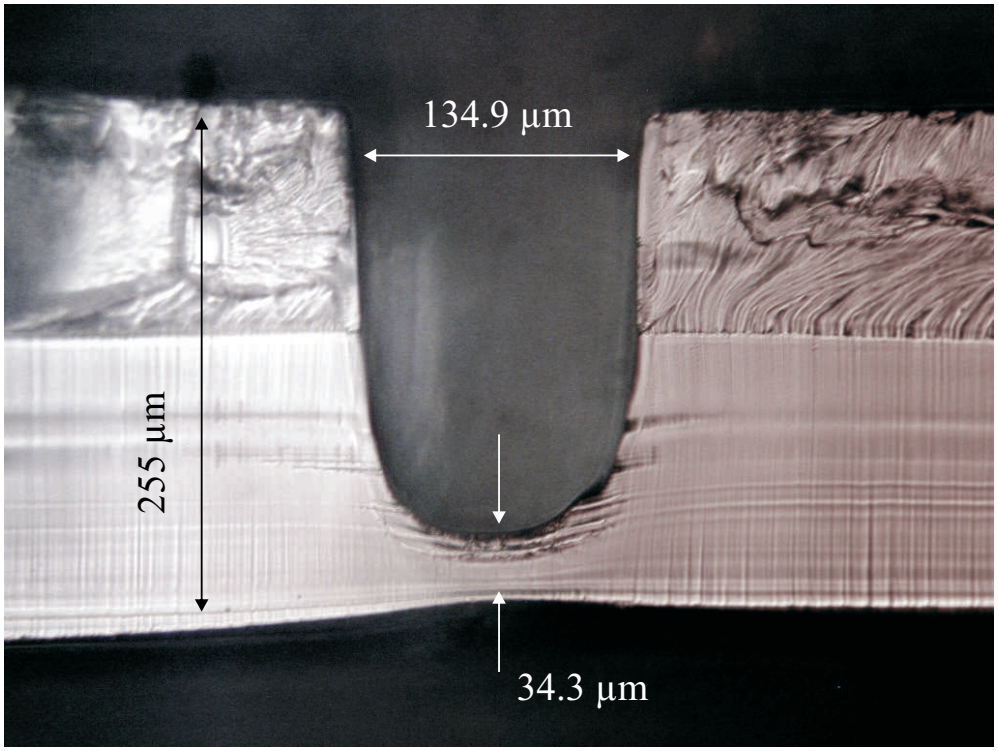

Figure 3.2.5. Cross section of a fabricated flexure hinge

$\pm 150\ V$, and have a resonance frequency of $> 1\ kHz$.

3.3 Compliant Mechanism Design and Modeling

3.3.1 Mechanism Design

Due to the flexure length limitations set by Equation 3.1, it is difficult to achieve large amplification with out-of-plane displacement. In this work, an offset slider-rocker compliant mechanism is designed using a bimorph mounted such that the input displacement direction is in-plane. This mechanism has high amplification and is shifted from the horizontal plane using a small vertical offset. To realize this design, flexure hinges must be designed to undergo large deformation yet resist buckling when loaded. Using the standard Euler buckling relationship for a flexure

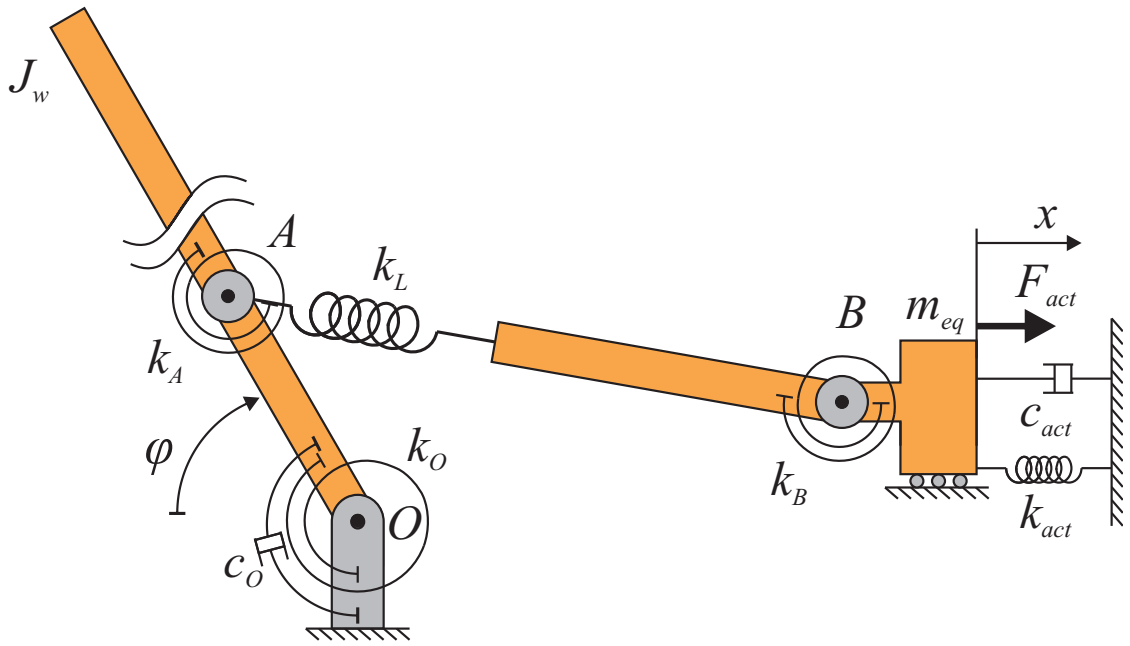

Figure 3.3.1. Schematic of pseudo rigid body model of slider crank mechanism

that is fixed at one end and free on the other, the critical axial load is

$$F_{crit} = \frac{\pi^2 E_f w_f t_f^3}{48 L_f^2} \tag{3.2}$$

In this work, the flexure lengths are designed to bend at a maximum of 60° and the flexure widths are designed to prevent buckling.

3.3.2 Modeling

Figure 3.3.1 shows a schematic of the psuedo rigid body approximation of the compliant slider-rocker mechanism. This approximation has been developed for large range of motion, and allows the flexure hinges to be approximated as ideal

pins with torsional stiffnesses of [70]

$$k_{eq} = \gamma K_\Theta \frac{E_f w_f t_f^3}{12 L_f}, \tag{3.3}$$

where γ is the characteristic radius factor and K_Θ is a stiffness coefficient dependent on the range of motion. This equation is used when the flexure length is on the same order of magnitude as the length of the rigid links. It is also assumed that no off axis translation or rotation occurs and the stiffness is linear along the range of motion of the spring. The mechanism consists of three main hinges, O, A, and B, with torsional stiffness, k_O, k_A, and k_B respectively. Linear viscous damping is included on main wing hinge O,

$$c_O = c_{O,f} + c_{O,air} \tag{3.4}$$

where $c_{O,f}$ is a structural damping term, and $c_{O,air}$ is linear damping term to simulate aerodynamic drag, with $c_{O,air} = 0$ in vacuum. The bimorph is modeled as a linear voltage controlled force acting upon the slider [74],

$$F_{act} = G_{act} V = \frac{9 E I_{eff} Y (2Y+1) d_{31} V}{2 t_m (t_m + 2t_p) L_{act} (XY^3 + 3Y^2 + 3Y + 1)}, \tag{3.5}$$

with linear stiffness, k_{act}, viscous damping, c_{act}, and linear displacement x.The actuator stiffness is

$$k_{act} = \frac{3 E I_{eff}}{L_{act}^3} \tag{3.6}$$

with

$$E I_{eff} = \frac{w_{act} E_p}{2} \left[\frac{t_p^3}{3} + t_p (t_m + t_p)^2 + \frac{E_m}{E_p} \frac{t_m^3}{6} \right], \tag{3.7}$$

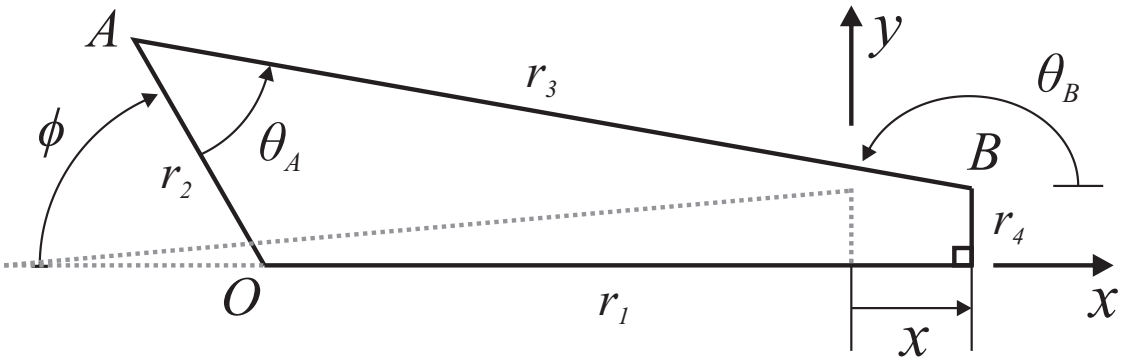

Figure 3.3.2. Link diagram of the slider rocker mechanism (initial (grey dashed) and final (black solid) configurations)

$X = E_m/E_p$, and $Y = t_m/(2t_p)$. The bimorph damping is included for generality but can be safely neglected relative to the large wing damping. The bimorph is attached to the wing by the coupler link with stiffness k_L. Figure 3.3.2 describes the flapping angle, ϕ, defined with respect to the negative x-axis, the hinge B angle, θ_B, defined with respect to the positive x-axis, the relative angle between the links AO and AB, θ_A, and the actuator input, x. The psuedo rigid body approximation gives $r_2 = L_{OA} + \gamma L_O - (1-\gamma)L_A$, where L_O and L_A are the lengths of the flexure hinges O and A respectively. The loop closure equations are solved to yield

$$r_3(\phi, x) = \frac{r_2 \cos\phi - r_1(x)}{\cos\theta_B} \tag{3.8}$$

$$\theta_B(\phi, x) = \arctan\frac{r_2 \sin\phi - r_4}{r_2 \cos\phi - r_1(x)} \tag{3.9}$$

$$\theta_A(\phi, x) = \theta_B - \phi \tag{3.10}$$

where $r_1(x) = r_{1_0} + x$, and r_{1_0} is the initial length of $r_1(x)$.

Using Figure 3.3.1, the potential energy of the mechanism is

$$U = \frac{1}{2}k_O(\phi - \phi_{ref})^2 + \frac{1}{2}\sum_{i=A,B} k_i(\theta_i(\phi, x) - \theta_{i,ref})^2 + \frac{1}{2}k_L(r_3(\phi, x) - r_{3,ref})^2 + \frac{1}{2}k_{act}(x - x_{ref})^2, \tag{3.11}$$

where ϕ_{ref}, $\theta_{A,ref}$, $\theta_{B,ref}$, $r_{3,ref}$, and x_{ref} are the reference positions of ϕ, θ_A, θ_B, r_3, and x, respectively. Gravitational potential energy is neglegible compared to the strain potential energy stored in the hinges and actuator.

The kinetic energy is

$$T = \frac{1}{2}J_w\dot{\phi}^2 + \frac{1}{2}m_{eq}\dot{x}^2, \tag{3.12}$$

where J_w is the wing inertia and m_{eq} is the equivalent mass of the actuator, $0.23m_{act}$. The mass and inertia of the coupler link is neglibly small. The wing inertia is approximated from a computer aided design (SolidWorks®) model of the wing with the density adjusted to match the measured mass of the fabricated wing. Assuming the wing is thin flat plate, the added mass can be found by

$$dm_{am} = \frac{\pi}{4}\rho_{air}c(r)^2dr, \tag{3.13}$$

where ρ_{air} is the density of air, and $c(r)$ is the chord length at position r along the wing. The added mass is calculated by numerically integrating this quantity in Matlab using a discretized image of the wing. Similarly, the added inertia is obtained by numerically integration of

$$J_{am} = \int_0^{R_w} r^2 dm_{am} = \frac{\pi}{4}\rho_{air}\int_0^{R_w} c(r)^2 r^2 dr. \tag{3.14}$$

The added mass is zero in vacuum.

The virtual work associated with the bimorph actuator and damping is

$$\delta W = -c_O \dot{\phi} \delta\phi + (G_{act} V - c_{act} \dot{x}) \delta x. \tag{3.15}$$

Choosing generalized coordinates $\boldsymbol{q} = [\phi, x]^T$, the equations of motion can be derived using the Euler-Lagrange formulation as

$$\boldsymbol{J}\ddot{\boldsymbol{q}} + \boldsymbol{C}\dot{\boldsymbol{q}} + \boldsymbol{f}(\boldsymbol{q}) = \boldsymbol{Q}, \tag{3.16}$$

where

$$\boldsymbol{J} = \begin{bmatrix} J_w & 0 \\ 0 & m_{eq} \end{bmatrix}, \tag{3.17}$$

$$\boldsymbol{C} = \begin{bmatrix} c_O & 0 \\ 0 & c_{act} \end{bmatrix}, \tag{3.18}$$

$$\boldsymbol{f}(\boldsymbol{q}) = \begin{bmatrix} \frac{\partial U}{\partial \phi} \\ \frac{\partial U}{\partial x} \end{bmatrix}, \tag{3.19}$$

$$\boldsymbol{Q} = \begin{bmatrix} 0 \\ G_{act} V \end{bmatrix}. \tag{3.20}$$

The static equilibrium point, q_{eq} depends on voltage as follows:

$$\boldsymbol{f}(\boldsymbol{q}) - \boldsymbol{Q} = 0. \tag{3.21}$$

The nonlinear stiffness can be linearized

$$\boldsymbol{K} = \begin{bmatrix} \frac{\partial f_1}{\partial \phi} & \frac{\partial f_1}{\partial x} \\ \frac{\partial f_2}{\partial \phi} & \frac{\partial f_2}{\partial x} \end{bmatrix} \Bigg|_{\boldsymbol{q}=\boldsymbol{q_{eq}}} = \begin{bmatrix} k_{11} & k_{12} \\ k_{12} & k_{22} \end{bmatrix}. \tag{3.22}$$

Taking the Laplace transform of the linearized equations of motion produces the

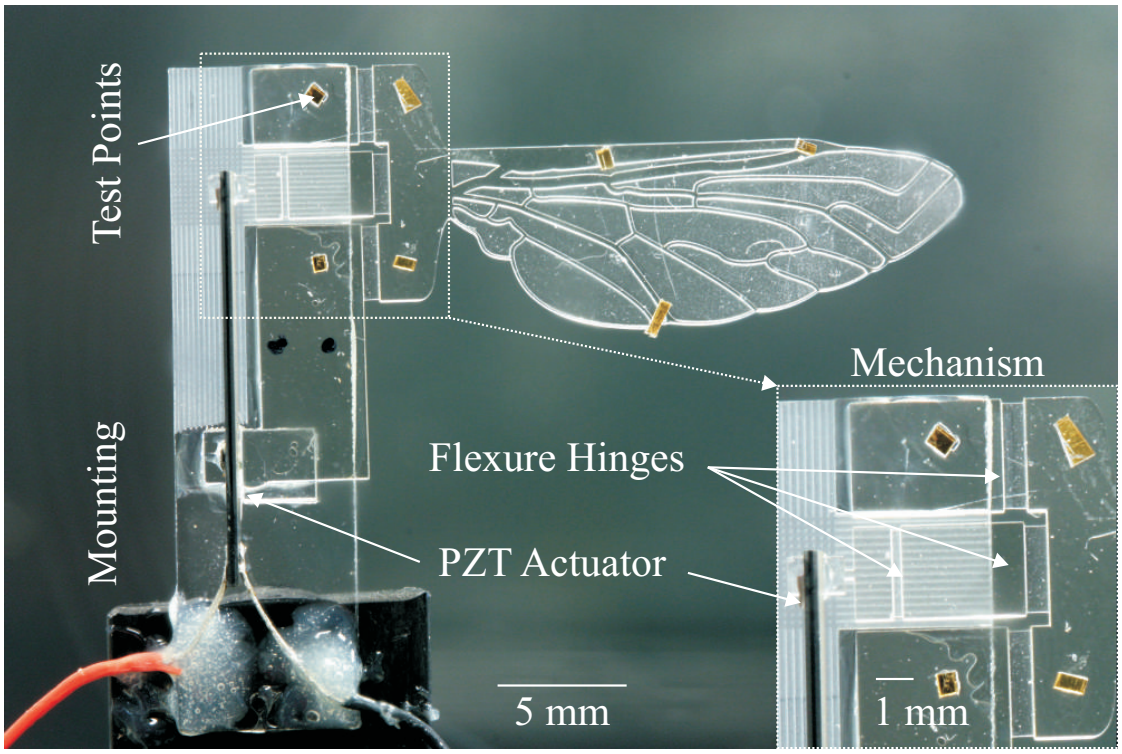

Figure 3.4.1. Photograph of LionFly prototype 07 and zoomed inset of flexure hinges and bimorph connection to coupler link.

linearized system transfer functions

$$\frac{\Phi(s)}{V(s)} = \frac{(-k_{12}G_{act}/(J_w m_{eq}))}{D(s)} \tag{3.23}$$

$$\frac{X(s)}{V(s)} = \frac{(s^2 + (c_O/J_w)s + k_{11}/J_w)G_{act}/m_{eq})}{D(s)}, \tag{3.24}$$

where

$$D(s) = (s^2 + (c_O/J_w)s + k_{11}/J_w) \cdot (s^2 + (c_{act}/m_{eq})s + k_{22}/m_{eq}) - k_{12}^2/(J_w m_{eq}). \tag{3.25}$$

3.4 Experimental Validation

The single wing LionFly prototype LF07, shown in Figure 3.4.1, is used for model validation. The piezoelectric bimorph tip is bonded to the coupler link, shown in the inset of Figure 3.4.1 using precision linear stages. The actuator is clamped at the base using a 2 mm by 2 mm glass square. Lead wires are soldered directly onto the bimorph. Gold film reflective test surfaces are attached to the wing and bimorph for laser vibrometer measurement.

3.4.1 Experimental Setup

Figure 3.4.2 shows the experimental setup used to test the LionFly mechanism. The mechanism is mounted on a carbon fiber holder in an aluminum vacuum chamber with an transparent quartz cover. The vacuum chamber is fixed to Newport linear stages for precise alignment. A Polytec® laser vibrometer measures the displacement at the test points on the wing surface and the bimorph tip. The vibrometer uses a 10× objective lens to focus the laser to a 25 μm point and returns displacement and velocity data to LabView® with sub micron precision. For small signal actuation, the LabView® DAQ system can provide a 10V amplitude signal, but for high voltage experiments (150 V amplitude with 150 V DC bias), a Matsusada® AP-1B3 amplifies the DAQ output.

3.4.2 Experimental Results

The static response is measured using an applied 100 V triangle wave over 240 seconds. The theoretical results are found by numerically solving the nonlinear equilibrium Equation 3.21 using Newton's method. The theoretical static response in Figure 3.4.3 (blue solid) matches the experimental response (blue circles) for small voltages but is lower than the experimental response at high voltages because PZT-5H is nonlinear, showing a field dependent d_{31} and hysteresis [75]. Introducing

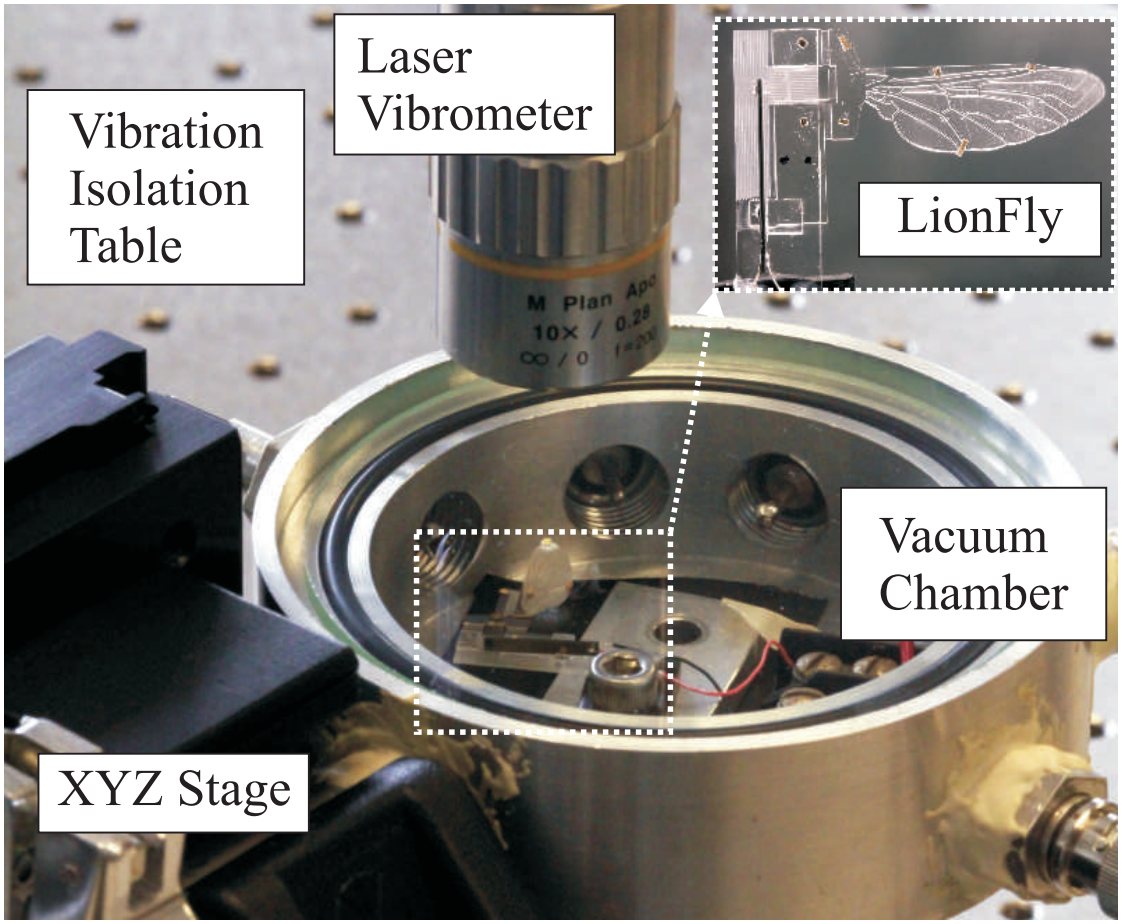

Figure 3.4.2. Photograph of experimental testing setup.

a quadratic, field dependent

$$d_{31}(V/t) = d_{31}(V/t) + \alpha(V/t)^2 \tag{3.26}$$

coefficient produces a more accurate theoretical (green dashed) curve. Static operation shows kinematic amplification of 0.244 $deg./\mu m$ and low voltage gains of 7.3 $deg./kV$ and 31.24 $\mu m/kV$ for θ and x respectively.

The flap and actuator displacement frequency responses of the LionFly mechanism LF07 are shown in Figures 3.4.4 and 3.4.5, respectively. Testing results in air and in a vacuum chamber pumped down to 76 Torr show velocity data measured

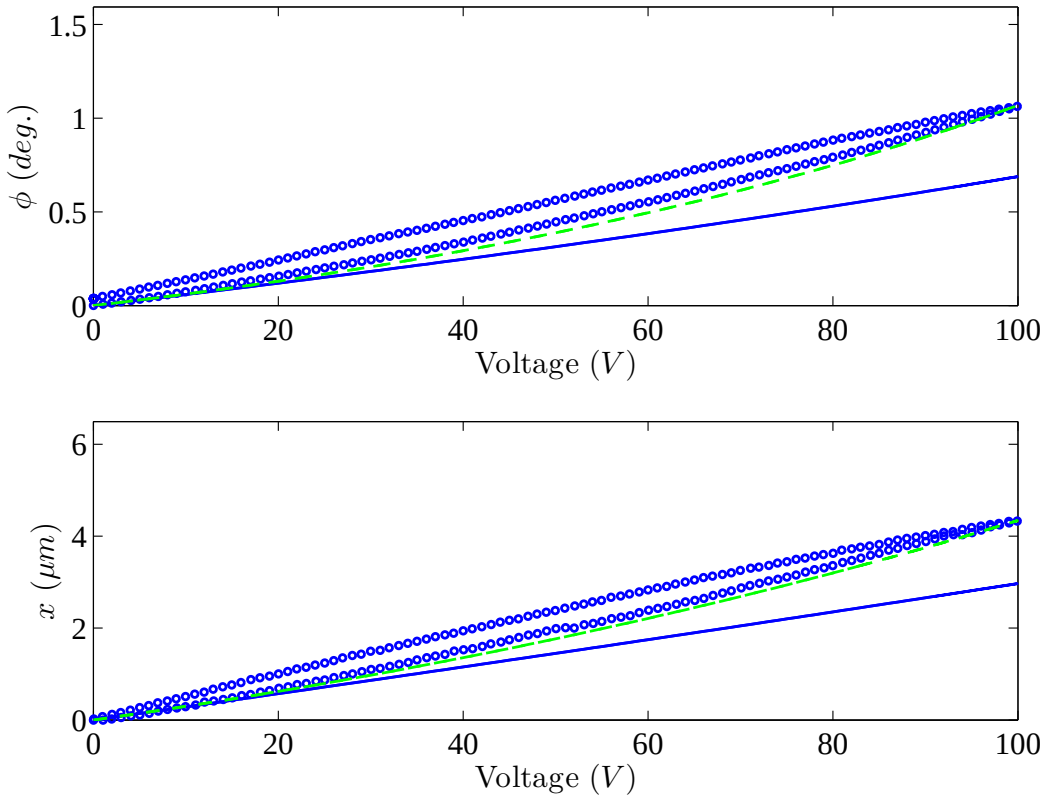

Figure 3.4.3. Quasi-static response of LF07: experimental data (blue circles) , theoretical curve using linear d_{31} (blue solid), theoretical curve using quadratic (green dashed).

from multiple points on the wing. The parameters used in model validation are shown in Table 3.4.1 for the bimorph and Table 3.4.2 for the LionFly mechanism LF07. Figure 3.4.4 shows the flapping angle calculated from the outermost test point using $\phi = \arctan(z_{meas}/R_{tp})$. The effect of aerodynamic added mass and drag are seen here as a shift in resonance frequency and a reduction in amplitude, respectively. The theoretical results show that the added mass calculation is effective in capturing this effect. The linear aerodynamic damping term is sufficient to capture the reduction in amplitude at this relatively low voltage excitation. No significant wing deformation is observed using the data from the numerous test points on the wing.

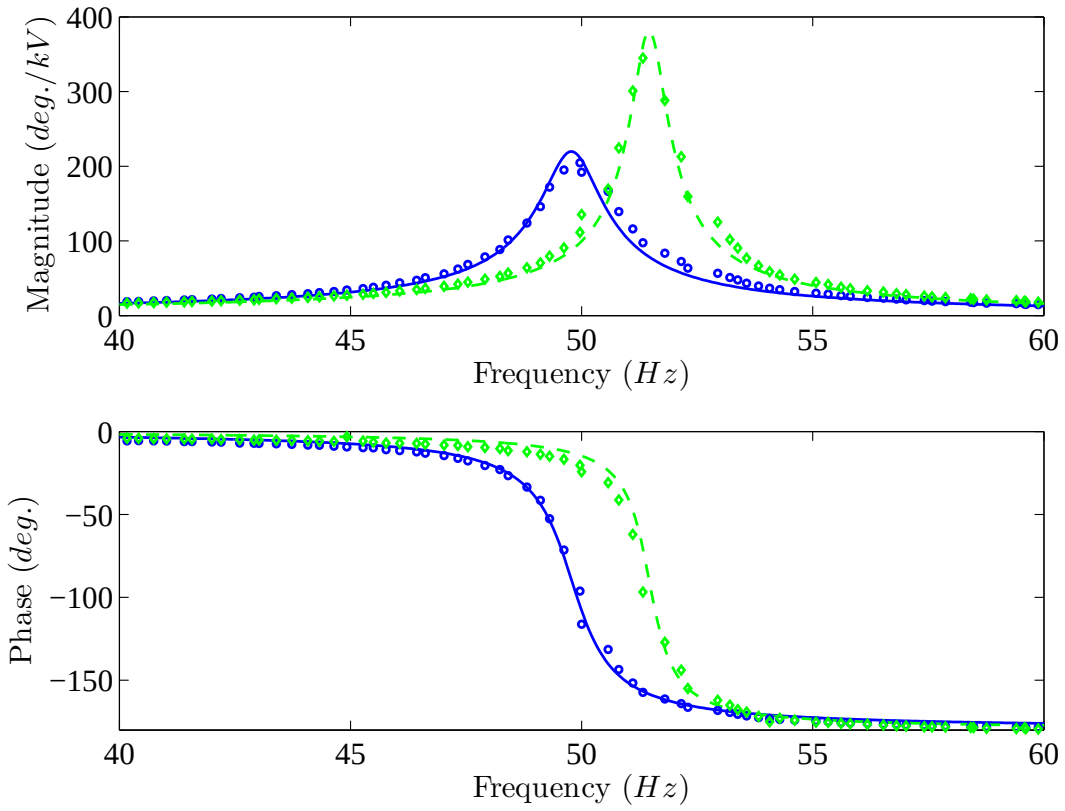

Figure 3.4.4. Frequency response $\Phi(s)/V(s)$ of LF07: Experimental data in air (blue circles), theoretical response in air (blue solid), experimental data in vacuum (green diamonds), theoretical response in vacuum (green dashed).

The frequency response of the LF07 bimorph actuator displacement shows good agreement between the experimental and theoretical results. The presence of the zero in Equation 3.24 is clearly seen here, at 53 Hz, and shows the effect of the coupler link compliance.

Several LionFly prototypes were tested with high voltage at resonance, and a summary of their performance is listed in Table 3.4.3. The fabricated LionFly prototypes show a consistent resonance frequency of 49.13 ± 1.43 Hz over four devices. Figure 3.4.6 shows the 55° peak flapping angle of the LionFly LF09. Continuous operation at large flapping angles, however, led to failure of the wing hinge.

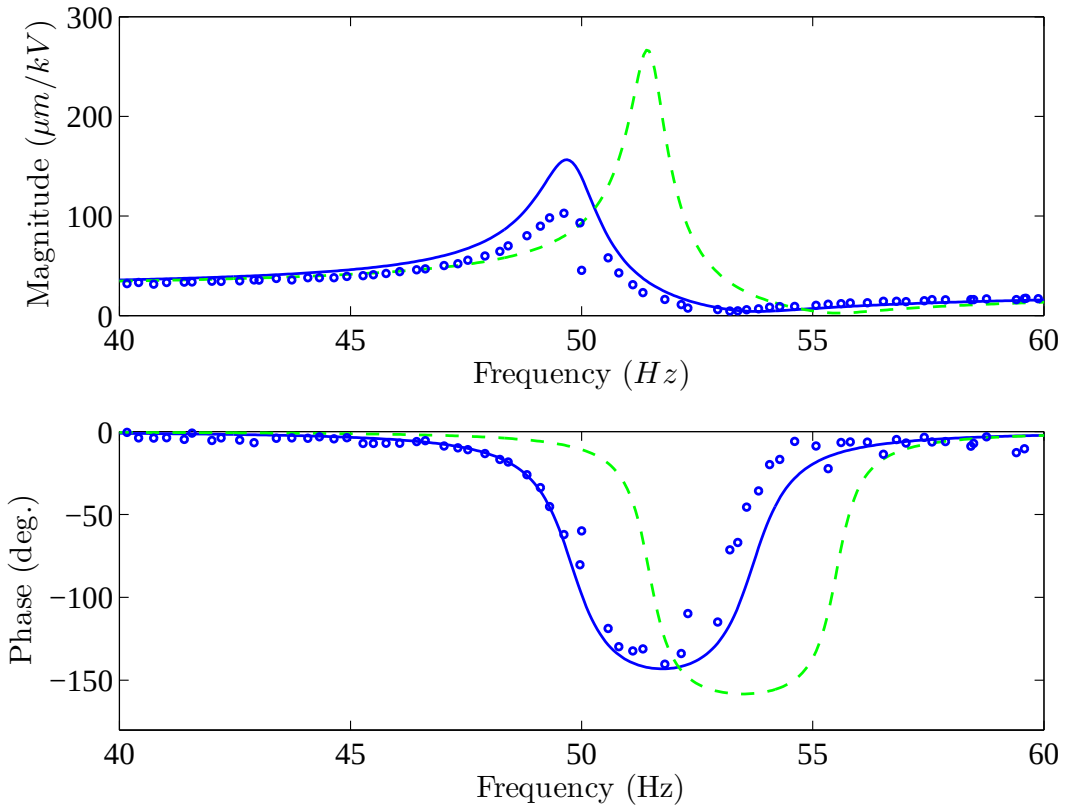

Figure 3.4.5. Frequency response $X(s)/V(s)$ of LF07: Experimental data in air (blue circles), theoretical response in air (blue solid), theoretical response in vacuum (green dashed).

Longer cycle life can be achieved by increasing flexure length and/or reducing flexure thickness to increase the maximum bending angle.

Table 3.4.1. Bimorph parameters and values for LF07

Parameter	Description	Value	
d_{31}	piezoelectric constant	-274.0	pm/V
α	quadratic field dependent coefficient	450.0	$(\mu m/mV)^2$
E_p	Young's modulus of PZT-5H	63.0	GPa
E_m	Young's modulus of shim	2.0	GPa
ρ_p	density of PZT-5H	7500.0	kg/m^3
ρ_m	density of shim	1600.0	kg/m^3
L_{act}	free length of actuator	9.5	mm
t_p	thickness of PZT-5H layer	135.0	μm
t_m	thickness of shim	115.0	μm
w_{act}	width of actuator	2.0	mm
m_{act}	mass of actuator	54.0	mg

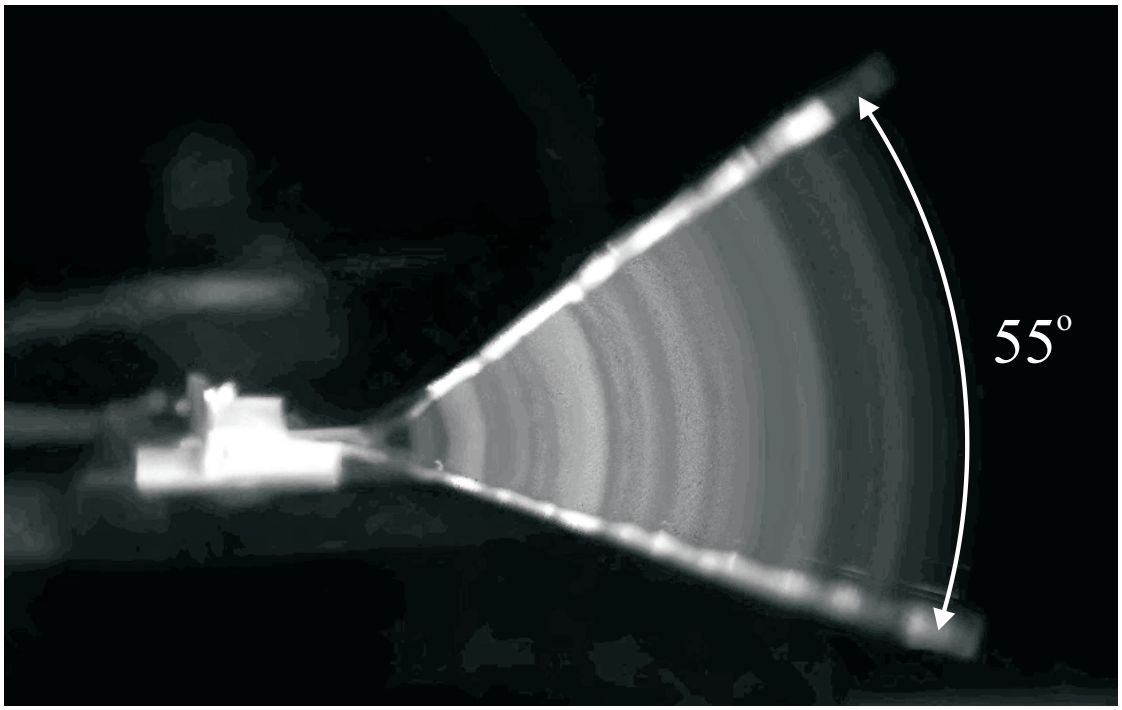

Figure 3.4.6. Flapping angle of LF09 with 150 V amplitude, 150 V DC offset, at 51 Hz

Table 3.4.2. LionFly parameters and values for LF07

Parameter	Description	Value	
Constants			
E_f	Young's modulus of SUEX	2.80	GPa
ρ_{air}	density of air	1.28	kg/m^3
ρ_{SUEX}	density of air	1190	kg/m^3
γ	characteristic radius factor	0.8517	
K_θ	stiffness coefficient	2.6762	
Mechanism Parameters			
L_{AB}	length of coupler link	3.25	mm
L_{OA}	length of rocker link	520.00	μm
L_A	length of flexure hinge A	670.00	μm
L_B	length of flexure hinge B	275.00	μm
L_O	length of flexure hinge O	670.00	μm
t_A	thickness of flexure hinge A	32.43	μm
t_B	thickness of flexure hinge B	34.41	μm
t_O	thickness of flexure hinge O	33.02	μm
w_A	width of flexure hinge A	2.30	mm
w_B	width of flexure hinge B	2.30	mm
w_O	width of flexure hinge O	5.60	mm
ϕ_{ref}	reference position of ϕ	0.00	$rad.$
$\theta_{A,ref}$	reference position of θ_A	0.00	$rad.$
$\theta_{B,ref}$	reference position of θ_B	π	$rad.$
x_{ref}	reference position of x	98	μm
r_{1_0}	initial value of r_1	2.87	mm
r_2	rocker length	0.99	mm
$r_{3,ref}$	reference value of r_3	3.86	mm
r_4	vertical offset of slider	0.10	mm
k_L	coupler link stiffness	17.50	N/mm
Wing Parameters			
m_w	mass of wing	18.70	mg
R_w	distance from hinge O to wing tip	23.00	mm
R_{tp}	distance from hinge O to test point	16.25	mm
J_w	wing inertia, in vacuum	1.80	$g \cdot mm^2$
J_{am}	inertia due to added mass	0.12	$g \cdot mm^2$
$c_{O,f}$	structural damping of ϕ	8.80	$mN \cdot \mu m \cdot s$
$c_{O,air}$	aerodynamic damping of ϕ	7.00	$mN \cdot \mu m \cdot s$

Table 3.4.3. Summary of LionFly prototype performance at 150 V, 150 V_{DC}

Device	$\Theta(0)$ $(deg.)$	f_r (Hz)	Θ_{Max} $(deg.)$
LF07	0.16^b	50.0^b	42^c
LF08	/	47.5^a	/
LF09	12.1	51.0	55.0
LF12	10.5	48.0	30.0

^{a}100 V_{pp}, device failure before Θ response measured
^{b}20 V_{pp}, ^{c}In vacuum, 250 V_{pp}, 125 V_{DC}, 44 Hz

Chapter 4

Wing Rotation in SUEX Flapping Wing Mechanisms

4.1 Introduction

In this chapter, a flexure hinge along the span of the LionFly wing allows the wing to rotate in addition to flapping. This chapter presents detailed modeling and experimental testing of wing rotation and lift in the LionFly, shown schematically in Figure 4.1.1. The goal of this chapter is to understand the flapping and rotation dynamics, and the lift-producing mechanisms in this device.

4.2 Modeling

4.2.1 Kinematics

The LionFly PAV shown in Figure 4.1.1 is a SUEX dry film compliant slider-rocker mechanism coupled to a PZT-5H bimorph actuator. Figure 4.2.1 shows the psuedo rigid body approximation of the slider-rocker mechanism. The flexure hinges are assumed to be ideal pins with torsional stiffness with zero off axis compliance.

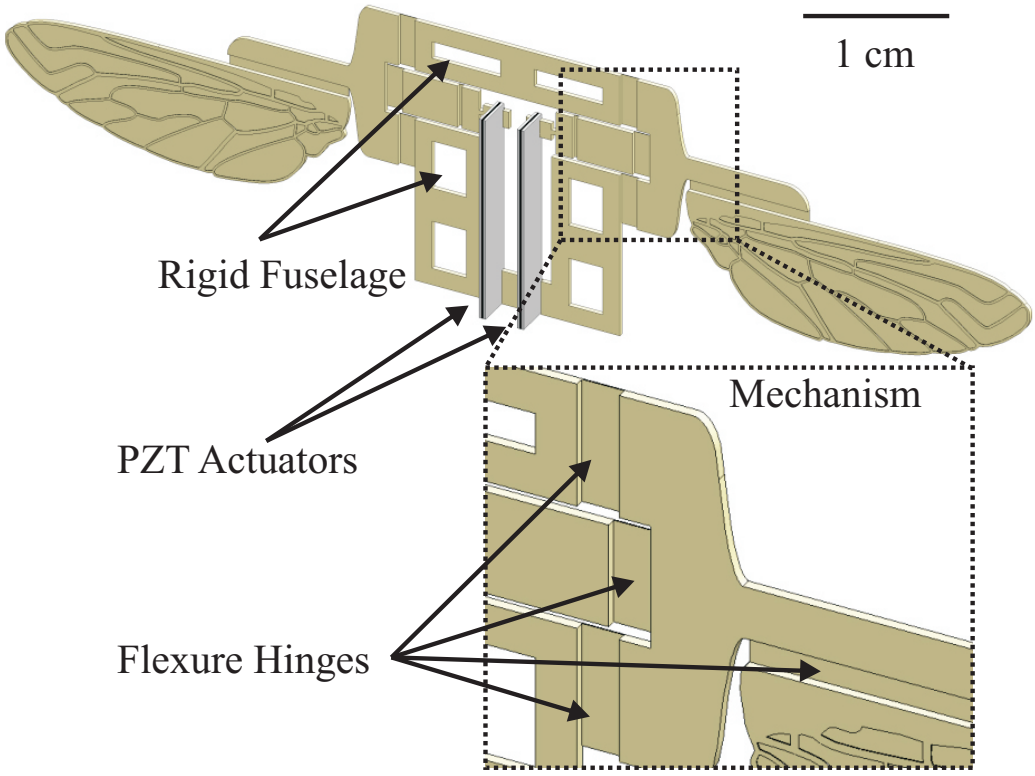

Figure 4.1.1. Conceptual drawing of the Penn State LionFly

The kinematics map the voltage-induced bimorph displacement to flapping angle. The mechanism is defined by the flexure lengths, L_A, L_B, L_O, link lengths, L_{AB}, L_{OA}, vertical offset, r_4, and the starting position of the actuator, x_{ref}. The flexure lengths and mechanism parameters must satisfy

$$L_{AB} - L_{OA} \pm r_4 + (L_A + L_B(1-\gamma) - L_O\gamma) > 0, \tag{4.1}$$

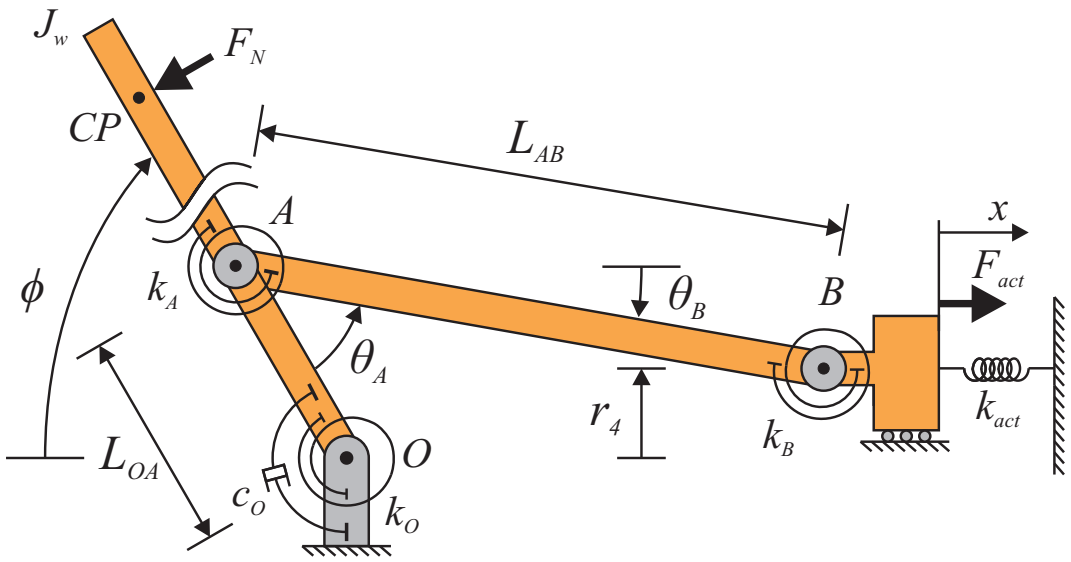

Figure 4.2.1. Schematic of slider rocker mechanism

where γ is the characteristic radius factor of a long flexure [70]. The kinematics relating the bimorph displacement to the flapping angle are

$$\phi(x) = \pi - \arccos\left(\frac{r_2^2 - r_3^2 + r_4^2 + (r_{1_0} + x)^2}{2r_2\sqrt{r_4^2 + (r_{1_0} + x)^2}}\right) - \arctan\left(\frac{r_4}{r_{1_0} + x}\right), \tag{4.2}$$

where the link lengths are

$$r_{1_0} = \sqrt{(r_3 - r_2)^2 - r_4^2}, \tag{4.3}$$

$$r_2 = L_{OA} + \gamma L_O - (1 - \gamma)L_A, \tag{4.4}$$

$$r_3 = L_{AB} + \gamma L_A + (1 - \gamma)L_B. \tag{4.5}$$

The initial ϕ angle is determined by finding the x_{ref} such that the equilibrium position x_0 yields $\phi_0(x_0) = \phi_{init}$. The potential energy of the single degree of freedom mechanism is

$$U = \frac{1}{2}k_O\phi(x)^2 + \frac{1}{2}\sum_{i=A,B} k_i\theta_i(x)^2 + \frac{1}{2}k_{act}(x - x_{ref})^2, \tag{4.6}$$

where k_O, k_A, and k_B are flexure hinge stiffnesses of the three joints of the slider rocker mechanism at O, A, and B, respectively, k_{act} is the actuator stiffness, θ_A and θ_B are the angles of the flexure hinges at A and B, respectively. The flexure stiffnesses are calculated by

$$k_{eq} = \gamma K_\Theta \frac{E_f w_f t_f^3}{12 L_f}, \tag{4.7}$$

where K_Θ is a stiffness coefficient dependent on the range of motion, E_f is the Young's modulus, w_f is the flexure width, t_f is the flexure thickness, and L_f is the flexure length [70]. The virtual work of the bimorph is

$$\delta W = G_{act} V \delta x, \tag{4.8}$$

where G_{act} is the blocking force gain of the actuator. The equilibrium equation is

$$G_{act} V - k_{act}(x_{ref} - x) - f_s(x) = 0, \tag{4.9}$$

where

$$f_s(x) = k_O \phi(x) \frac{\partial \phi}{\partial x} + \sum_{i=A,B} k_i \theta_i(x) \frac{\partial \theta_i}{\partial x} \tag{4.10}$$

Solving Equation 4.9 when $V = 0$ for x_{ref} with $x = x_{eq} = \phi^{-1}(\phi_0)$ yields the position of the bimorph needed for any desired initial angle. At this equilibrium position, the kinematics can be linearized to

$$\phi = \left. \frac{\partial \phi(x)}{\partial x} \right|_{x=x_{eq}} x = ax, \tag{4.11}$$

using Equation 4.2.

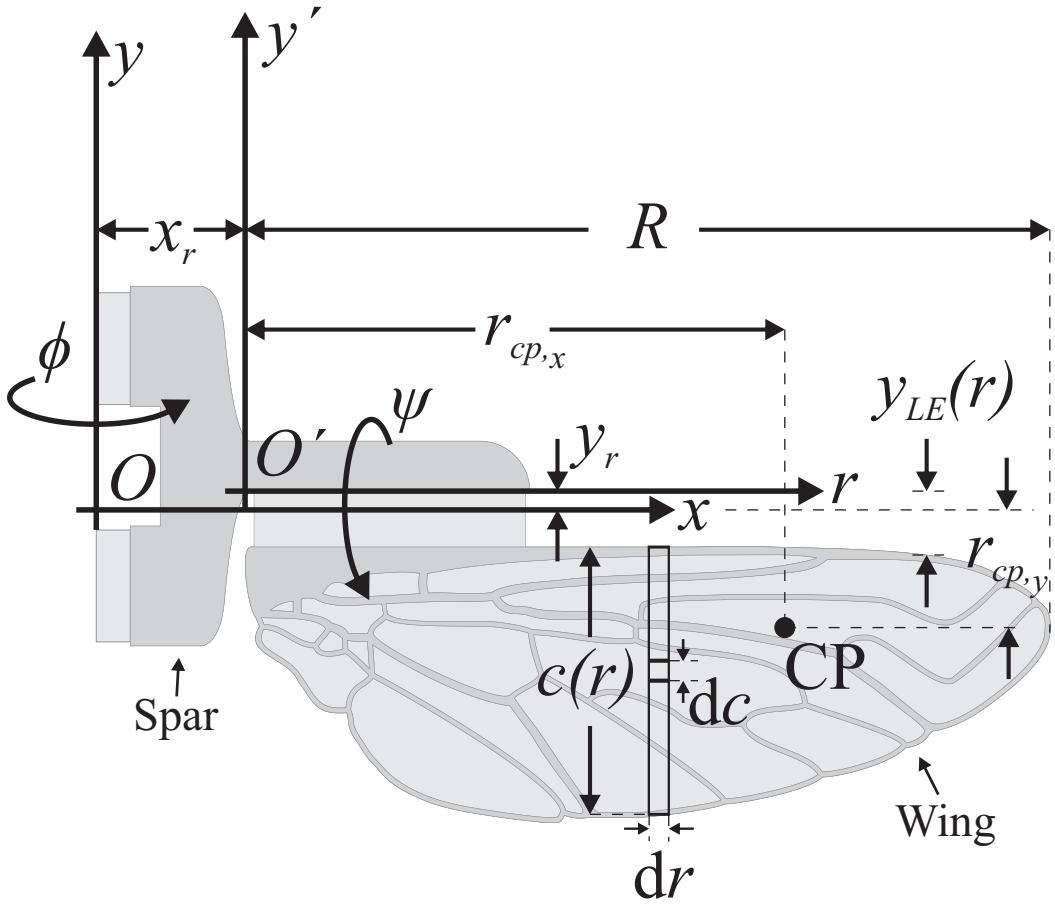

Figure 4.2.2. Schematic of LionFly wing defining fixed frame xy and wing frame ry' and relevant aerodynamic parameters

4.2.2 Vibration

Figure 4.2.2 shows the LionFly wing and spar with two degrees of freedom: rotation about the y axis, ϕ, and rotation about the x axis, ψ. Using the kinematics developed in the previous section, the potential energy of the mechanism is

$$U = \frac{1}{2}k_O\phi(x)^2 + \frac{1}{2}\sum_{i=A,B} k_i\theta_i(x)^2 + \frac{1}{2}k_{act}(x - x_{ref})^2 + \frac{1}{2}k_\psi\psi^2, \tag{4.12}$$

where k_ψ is the rotational flexure hinge stiffness. Gravitational potential energy is negligible compared to the strain potential energy stored in the hinges and actuator. The virtual work associated with the bimorph actuator input force, aerodynamic forces, aerodynamic damping, and linear viscous damping are

$$\begin{aligned}\delta W &= G_{act} V \delta x - F_N \delta \vec{r}_{CP} - M_\psi \delta\psi - c_\phi \dot{\phi}\delta\phi - c_\psi \dot{\psi}\delta\psi \\ &= \left(G_{act} a^{-1} V - F_N r_{cp_x} \cos\psi \cos\phi - c_\phi \dot{\phi}\right)\delta\phi \\ &\quad + \left(-F_N r_{cp_y} - M_\psi - c_\psi \dot{\psi}\right)\delta\psi \end{aligned} \tag{4.13}$$

where $\vec{r}_{cp}$ is the distance from the origin, O, to the center of pressure on the wing, and c_ϕ and c_ψ are the linear viscous damping coefficients of ϕ and ψ, respectively. The aerodynamic force normal to the wing, F_N, the aerodynamic damping term associated with rotation, M_ψ, and the center of pressure location, r_{cp_x} and r_{cp_y}, will be described in detail in the next section. Using the generalized coordinates, $\mathbf{q} = [\phi, \psi]$, the kinetic energy is

$$T = \frac{1}{2}\dot{\mathbf{q}}^{\mathbf{T}}\mathbf{J}\dot{\mathbf{q}} \tag{4.14}$$

with

$$\mathbf{J} = \begin{bmatrix} J_{yy} + J_s + J_{am_{yy}} & J_{xy} + J_{am_{xy}} \\ J_{xy} + J_{am_{xy}} & J_{xx} + J_{am_{xx}} \end{bmatrix} = \begin{bmatrix} J_\phi & J_{\psi\phi} \\ J_{\psi\phi} & J_\psi \end{bmatrix}, \tag{4.15}$$

where J_s is the inertia of the wing spar, and J_{xx}, J_{xy}, and J_{yy} are components of the wing inertia in the wing fixed coordinate system with associated added inertia terms $J_{am_{xx}}$, $J_{am_{xy}}$, and $J_{am_{yy}}$. The amplification factor is large ($a \sim 3200\ rad/m$), so the reflected equivalent mass of the actuator, $0.23 m_{act} a^{-2}$, is neglible compared to the wing and spar inertias. Using Lagrange's equations, with potential energy in Equation 4.12 linearized about $\mathbf{q_0} = [a x_{eq}, 0]$, kinetic energy in Equation 4.14,

and virtual work in Equation 4.13, the equations of motion are

$$\mathbf{J\ddot{q}} + \mathbf{Cq} + \mathbf{Kq} = \mathbf{BQ} \tag{4.16}$$

where

$$\mathbf{C} = \begin{bmatrix} c_\phi & 0 \\ 0 & c_\psi \end{bmatrix}, \tag{4.17}$$

$$\mathbf{K} = \begin{bmatrix} k_\phi & 0 \\ 0 & k_\psi \end{bmatrix}, \tag{4.18}$$

$$\mathbf{B} = \begin{bmatrix} G_{act}a^{-1} & -r_{CP_x}\cos(\psi)\cos(\phi) & 0 \\ 0 & -r_{CP_y} & -1 \end{bmatrix}, \tag{4.19}$$

$$\mathbf{Q} = \begin{bmatrix} V & F_N & M_\psi \end{bmatrix} \tag{4.20}$$

where

$$k_\phi = \frac{1}{a^2}\frac{\partial^2 U}{\partial x^2}\bigg|_{x=x_{eq}}$$

In vacuum, we can assume that the added mass terms, aerodynamic force, F_N, and moment, M_ψ are zero, and we can take the Laplace transform of Eq. 4.16 to find the transfer functions from applied voltage,

$$\frac{\Phi(s)}{V(s)} = \frac{((G_{act}/J_\phi)(s^2 + (c_\psi/J_\psi)s + (k_\psi/J_\psi)))}{D(s)} \tag{4.21}$$

$$\frac{\Psi(s)}{V(s)} = \frac{(G_{act}J_{\phi\psi}/J_\phi J_\psi)\, s^2}{D(s)} \tag{4.22}$$

where

$$D(s) = \left(s^2 + (c_\psi/J_\psi)s + (k_\psi/J_\psi)\right)\left(s^2 + (c_\phi/J_\phi)s + (k_\phi/J_\phi)\right) - J_{\phi\psi}^2 s^4/(J_\phi J_\psi) \tag{4.23}$$

4.2.3 Aerodynamics

The aerodynamic forces and moments presented here use quasi-steady approximations and the blade element method (BEM) [33]. We assume a hover configuration with the device mounted vertically, flapping stroke is limited to the horizontal plane, and zero ambient air velocity. Aerodynamic forces on the spar are neglected because the area and tip velocity are significantly smaller than the wing. Although many insect wings deform during the flap cycle [76], we assume the wing spar and aerofoil are rigid.

4.2.3.1 Aerodynamic Forces

Figure 4.2.2 shows relevant aerodynamic parameters for the LionFly wing. The origin, O, is defined as the intersection of the flapping axis, y, and the rotation axis, x. The wing root origin, O', is placed at the most proximal point along the leading edge of the aerofoil [33], The axes r and y' are shifted from the x and y axes by x_r and y_r, respectively. The position along the span of the wing is r, and the chord along the span of the wing is $c(r)$. The spanwise wing coordinates are nondimensionalized by the span from wing root (origin O') to wing tip, R [77]. The mean chord, $\bar{c} = A/R$, where A is the total wing area, is used to nondimensionalize chordwise coordinates. The spanwise position of the center of pressure is found by finding the second radius moment in the ry' frame,

$$\hat{r}_2^2 \equiv \int_0^1 \hat{c}(\hat{r})\hat{r}^2 d\hat{r} \tag{4.24}$$

and the spanwise center of pressure can be found by $r_{cp_x} = R\hat{r}_2$ [77]. The chordwise position of the center of pressure depends on the instantaneous angle of attack and can change position during the wing cycle. In the ry' frame, the location of the center of pressure for each blade element as a function of angle of attack, α is found

experimentally from a scaled model *Drosophila* wing [78],

$$\hat{y'}_{cp}(r,\alpha) = -\hat{c}(\hat{r})\left(\frac{0.82}{\pi}|\alpha| + 0.05\right). \tag{4.25}$$

In the xy frame, accounting for the wing hinge, and leading edge profile, the nondimensional chordwise center of pressure is

$$\hat{y}_{cp} = \frac{\int_0^1 \left[\hat{y}_r + \hat{y}_{LE}(\hat{r}) + \hat{y}'_{cp}(r,\alpha)\right](\hat{r}+\hat{x}_r)^2\hat{c}(\hat{r})d\hat{r}}{\int_0^1 (\hat{r}+\hat{x}_r)^2\,\hat{c}(\hat{r})d\hat{r}} \tag{4.26}$$

and the chordwise center of pressure can be found by $r_{cp_y} = y_{cp}\bar{c}$. The aerodynamic force normal to the wing is

$$F_N = \frac{1}{2}\rho_{air}\dot{\phi}|\dot{\phi}|C_N(\alpha)\bar{c}R^3\int_0^1 (\hat{r}+\hat{x}_r)^2\,\hat{c}(\hat{r})d\hat{r}, \tag{4.27}$$

where ρ_{air} is the density of air, and $C_N(\alpha)$ is the aerodynamic force coefficient normal to the wing, and α is the angle of attack [33]. The coefficients of lift and drag are given by

$$C_L(\alpha) = 1.8\sin(2\alpha), \tag{4.28}$$

$$C_D(\alpha) = 1.9 - 1.5\cos(2\alpha), \tag{4.29}$$

from which the aerodynamic force coefficient normal to the wing can be found from the rotational transformation,

$$C_N(\alpha) = C_L\cos(\alpha) + C_D\sin(\alpha) \approx 3.4\sin(\alpha), \tag{4.30}$$

assuming the transverse force coefficient, C_T is neglible for a thin flat plate. In the steady case of hovering, where the flapping stroke is horizontal, the 'geometric'

angle of attack, relative to the free-stream velocity, can be used [32]:

$$\alpha = \frac{\pi}{2} - \psi. \tag{4.31}$$

The lift force is found using the rotation angle, ψ,

$$F_L = F_N \sin(\psi) \tag{4.32}$$

4.2.3.2 Aerodynamic Moments

The relative air velocity due to rotation increases linearly away from the hinge axis, so the rotational damping is

$$M_\psi = -\frac{1}{2}\rho_{air}\dot{\psi}|\dot{\psi}|C_{rd}\bar{c}^4 R\hat{y}_{rd}, \tag{4.33}$$

where the leading edge position, y_0, and trailing edge position, y_1, and effective moment arm y_{rd} are

$$\hat{y}_0 = \hat{y}_r + \hat{y}_{LE}(\hat{r}) - \hat{c}(\hat{r}), \tag{4.34}$$

$$\hat{y}_1 = \hat{y}_r + \hat{y}_{LE}(\hat{r}), \tag{4.35}$$

$$\hat{y}_{rd} = \frac{1}{4}\int_0^1 \left[|\hat{y}_1|(\hat{y}_1)^3 - |\hat{y}_0|(\hat{y}_0)^3\right] d\hat{r} \tag{4.36}$$

and C_{rd} is the rotational damping coefficient.

4.2.3.3 Added Mass

Using added-mass coefficients for a thin flat wing section[79, 33], the added inertia terms are

$$J_{yy_{am}} = \int_0^R r^2 dm_{am} = \frac{\pi}{4}\rho_{air}\bar{c}^2 R^3 \int_0^1 (\hat{r} + \hat{x}_r)^2 \hat{c}(r)^2 d\hat{r}, \tag{4.37}$$

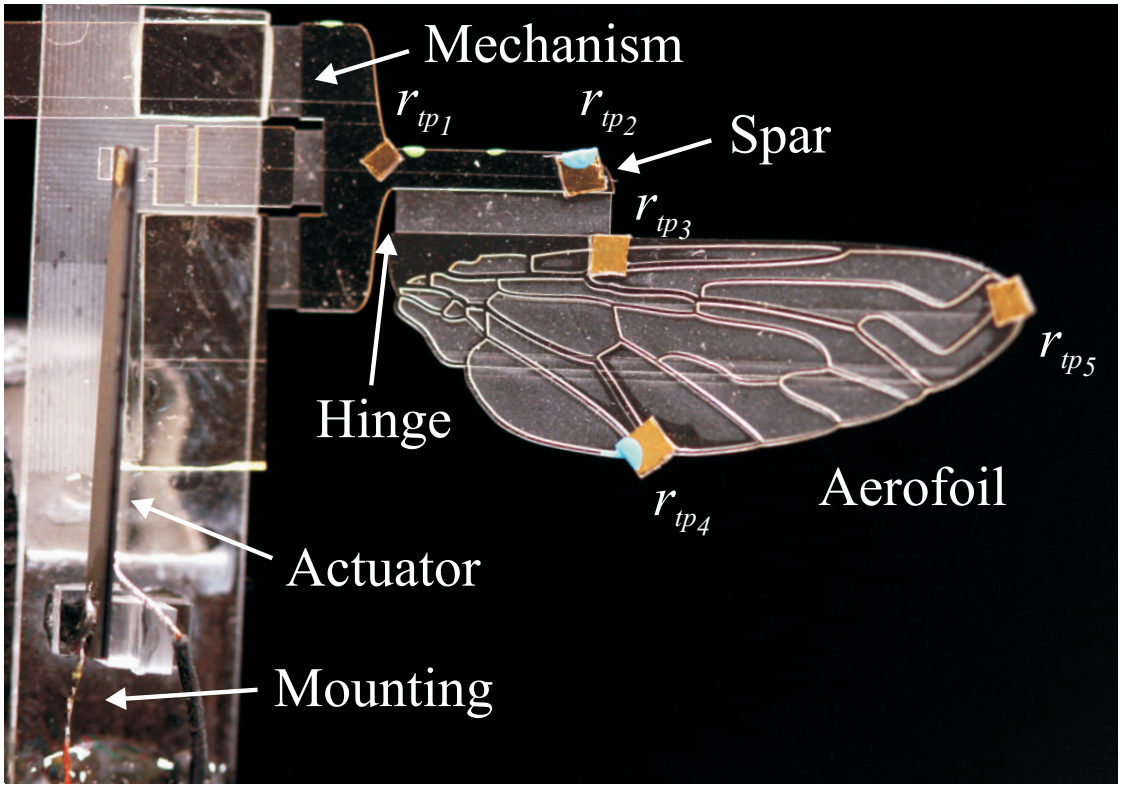

Figure 4.3.1. Photograph of fabricated prototype LionFly LF1203R20

$$J_{xy_{am}} = \int_0^R r y_h dm_{am} = \frac{\pi}{4}\rho_{air}\bar{c}^2 R^2 \int_0^1 (\hat{r} + \hat{x}_r)\hat{y}_h \hat{c}(r)^2 d\hat{r}, \tag{4.38}$$

$$J_{xx_{am}} = \int_0^R (y_h^2 + \frac{1}{32}c(r)^2) dm_{am} = \frac{\pi}{4}\rho_{air}\bar{c}^2 R \int_0^1 \hat{y}_h^2 \hat{c}(r)^2 d\hat{r}, \tag{4.39}$$

where $\hat{y}_h$ is the nondimensional distance from the midpoint to the rotational axis,

$$\hat{y}_h(\hat{r}) = \frac{1}{2}\hat{c}(\hat{r}) - \hat{y}_{LE}(\hat{r}) - \hat{y}_r. \tag{4.40}$$

4.3 Experimental Testing

Figure 4.3.1 shows the LionFly mechanism fabricated using the process developed in Section 3.2.2 and mounted onto a glass slide for characterization. A 2 mm $\times$ 16 mm PZT-5H bimorph actuator is mounted using precision linear stages. Using

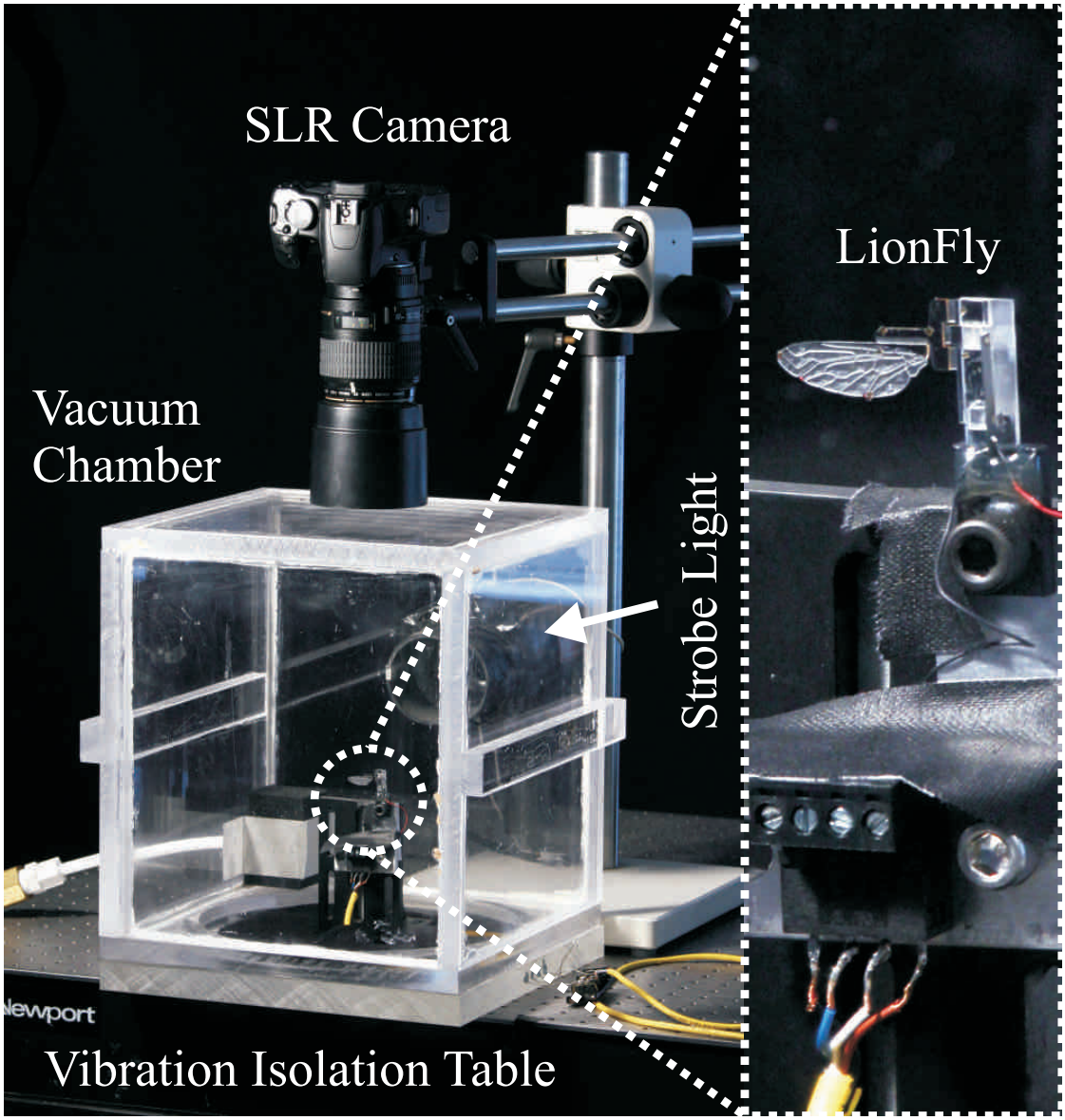

Figure 4.3.2. Photograph of experimental setup used for high voltage experiments

the stages, the wing is positioned at an initial angle ϕ_0 and fixed by clamping the bimorph with a 2 mm $\times$ 2 mm glass square bonded with cyanoacrylate. Gold reflective surfaces are attached to certain positions on the wing for small signal laser vibrometer measurement. A Polytec® laser vibrometer measures the displacement at the test points on the wing surface.. The vibrometer uses a 10$\times$ objective lens

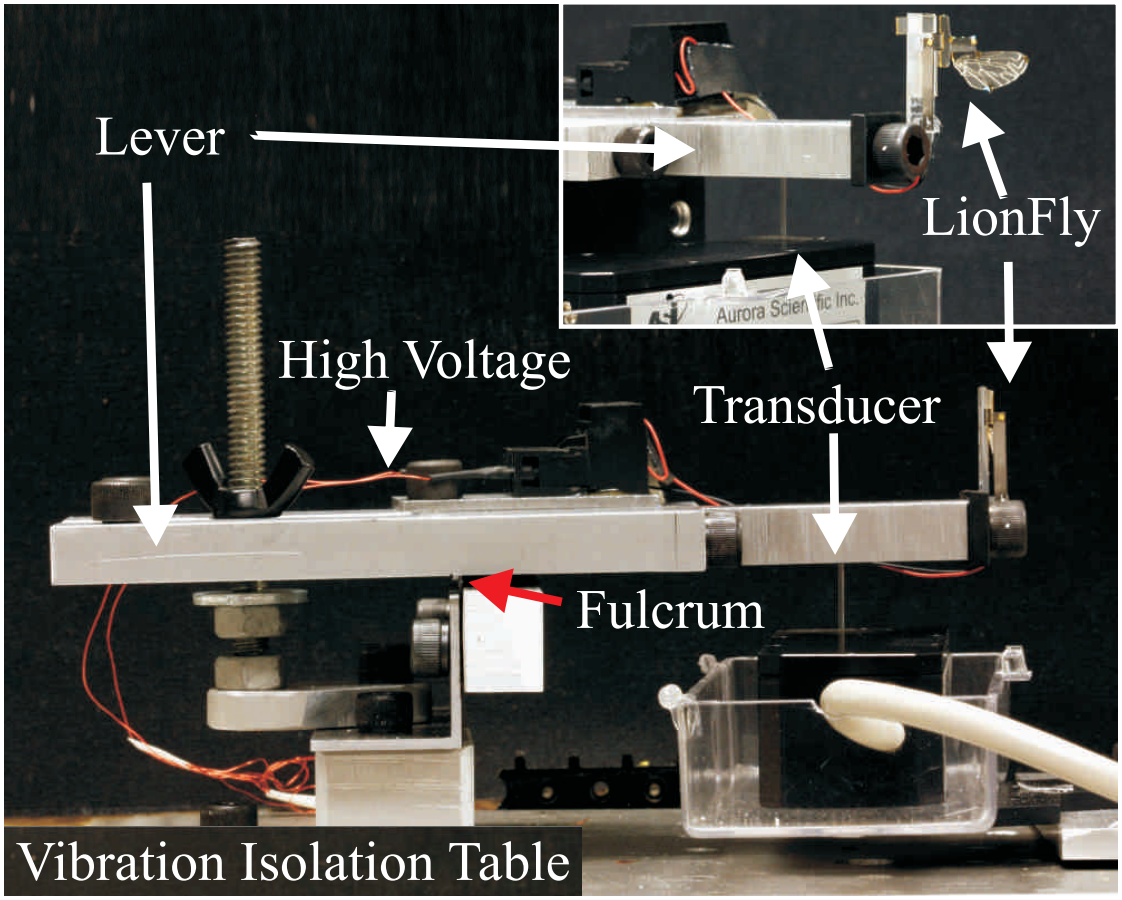

Figure 4.3.3. Photograph of experimental setup used for lift measurement experiments

to focus the laser to a 25 μm point and returns displacement and velocity data to LabView® with sub micron precision. For small signal actuation, the LabView® DAQ system can provide a 5 V amplitude signal, but for high voltage experiments ($25 - 75$ V amplitude with 75 V DC bias), a Matsusada® AP-1B3 amplifies the DAQ output. Figure 4.3.2 shows a photograph of the experimental setup used to measure high voltage wing trajectories using stroboscopic photography. LabView controls the digital SLR camera, strobe light, and the Matsusada® amplifier. A frequency sweep is conducted by adjusting the strobe frequency with the actuation frequency and taking twenty pictures throughout the wing flapping cycle at each frequency point. The photographs are processed in custom Matlab® software and

wing $\phi(t)$ and $\psi(t)$ data are extracted.

Figure 4.3.3 shows a photograph of the lift measurement setup. The LionFly is positioned vertically and bolted to an aluminum lever arm with a razor blade fulcrum that rests on an Aurora Scientific® Inc. 402A force transducer with 10 μN resolution and 2kHz bandwidth. The lever constrains the force measurement to a single degree of freedom, preloads the transducer, and allows dynamic loads to be transmitted to the transducer. When the device is actuated, the lift generated decreases the measured load on the transducer proportional to the leverage, and average lift data is taken from 100 cycles.

Flexure and membrane thicknesses are measured using a Zygo® NewView 100C optical profilometer and vein thickness using a micrometer. The initial angle and vertical offset were measured using high resolution macro photographs with calibrated pixels. A three dimensional model of the wing, spar, veins, and test points was created in Matlab using discretized images and the measured vein and membrane thickness, t_{vein} and t_{mem}, respectively. The inertia terms were calculated by numerically integrating the model wing using the reported value for SUEX density, ρ_{SUEX}. As a check, the mass was experimentally measured and verified to match the calculated mass of the wing. Using the measured value of wing span, R, and the profile of the wing and spar, all aerodynamic parameters can be numerically calculated.

4.3.1 Experimental Results

Out-of-plane laser vibrometer data is transformed into flapping and rotation angles using the displacement of test points on the wing, shown in Figure 4.3.1

$$\vec{r}_{tp_i} = x_i\hat{i} + y_i\hat{j} + z_i\hat{k}, \tag{4.41}$$

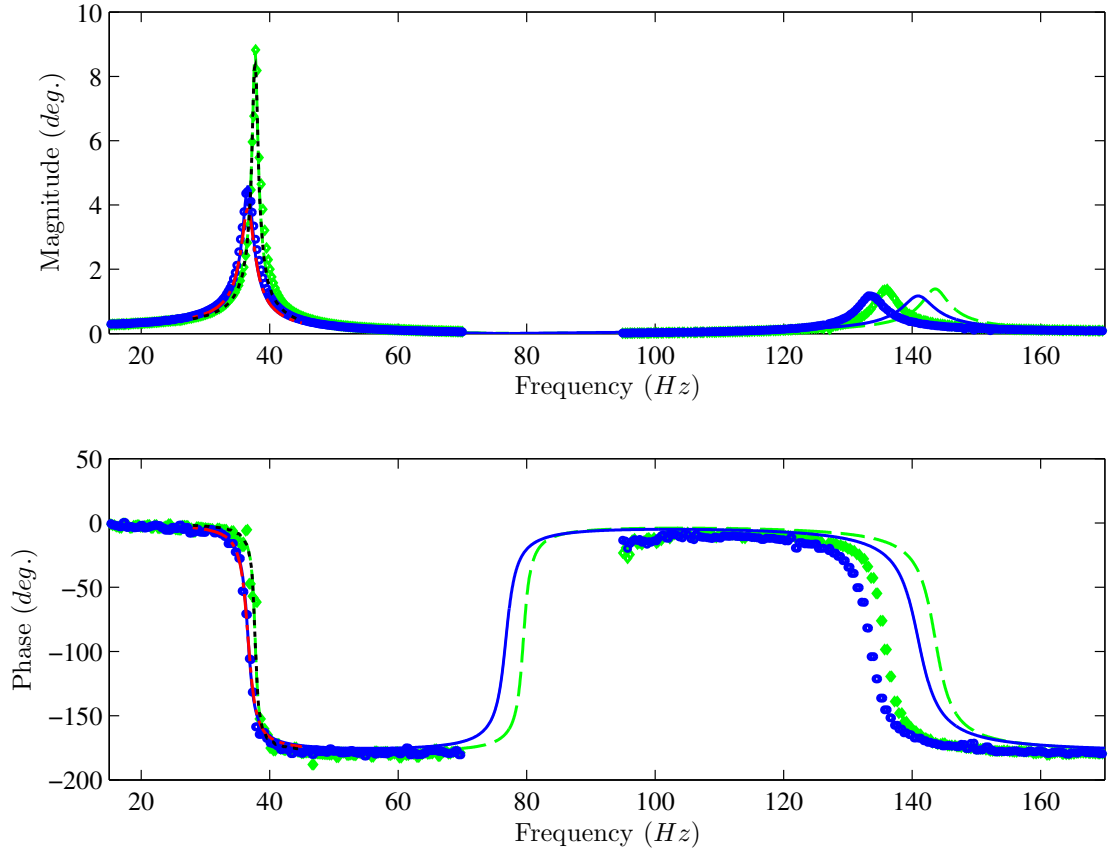

Figure 4.3.4. Flapping frequency response $\Phi(s)$ of LionFly LF1203 (0 VDC/5 VAC): Experimental data in air (blue circles), theoretical response in air (blue solid), experimental data in vacuum (green diamonds), theoretical response in vacuum (green dashed), simulated response in air (red dashed dot), simulated response in vacuum (black dotted).

where x_i and y_i are the x and y distance from the ϕ and ψ axes, respectively, and z_i is the measured vibrometer displacement, given by $z_i = \delta_{meas} e^{j\theta_V - \theta_\delta}$, where δ_{meas} is a vector of magnitudes of the displacement frequency response, θ_V is the phase of the voltage signal, and θ_δ is the phase of the displacement signal. The vector perpendicular to the wing plane can be written as

$$\vec{n} = (\vec{r}_{tp_3} - \vec{r}_{tp_4}) \times (\vec{r}_{tp_5} - \vec{r}_{tp_4}) = x_n \hat{i} + y_n \hat{j} + z_n \hat{k}. \tag{4.42}$$

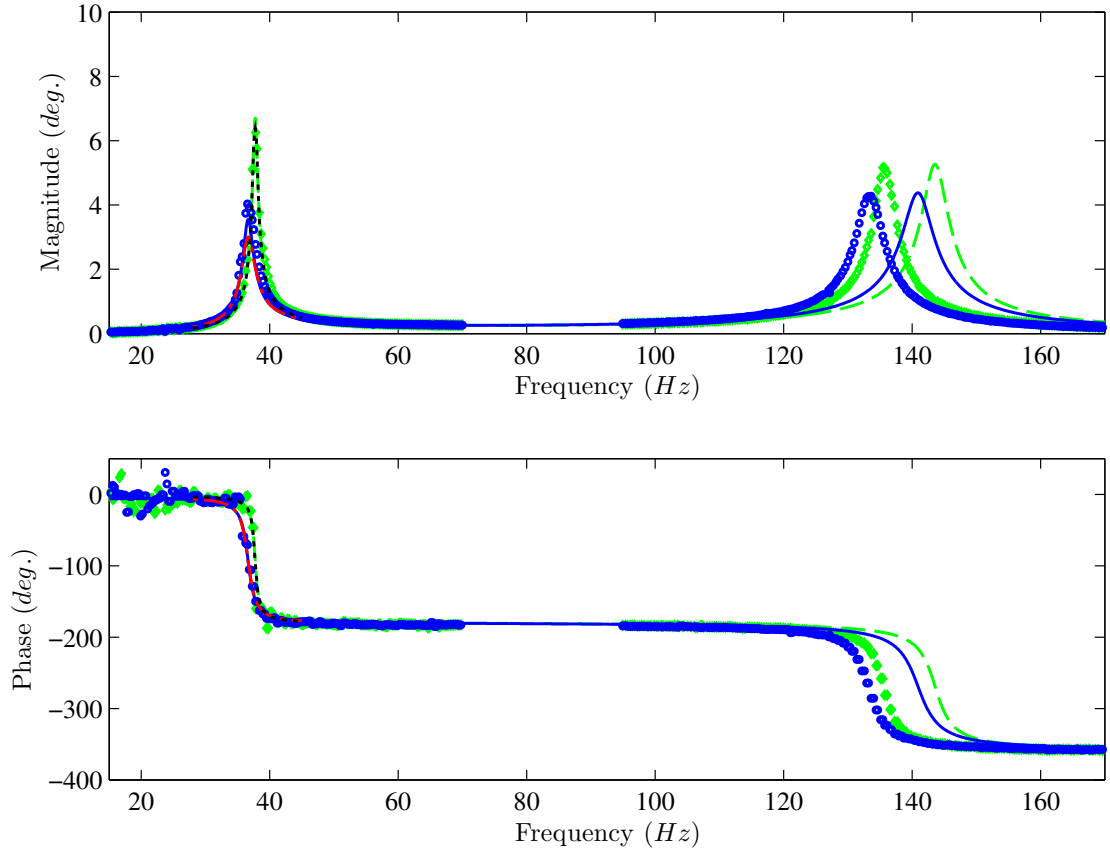

Figure 4.3.5. Rotation frequency response $\Psi(s)$ of LionFly LF1203 (0 VDC/5 VAC): Experimental data in air (blue circles), theoretical response in air (blue solid), experimental data in vacuum (green diamonds), theoretical response in vacuum (green dashed), simulated response in air (red dashed dot), simulated response in vacuum (black dotted).

and the transformed angles are calculated as

$$\phi = \arctan\left(\frac{-x_n}{z_n}\right), \tag{4.43}$$

$$\psi = \arctan\left(\frac{y_n}{z_n}\right). \tag{4.44}$$

Figures 4.3.4 and 4.3.5 show the frequency response of flapping and rotation, respectively, under applied voltage of 5 V amplitude, using Equations 4.21 and 4.22, respectively, and also using the nonlinear aerodynamics in Equation 4.16. Tables 4.3.1- 4.3.4 show the selected parameter and values used in the modeling.

Table 4.3.1. Constant parameters and values

Constants ($Units$)	Description	Value
E_f (GPa)	Young's modulus of SUEX	2.80
γ	characteristic radius factor	0.8517
K_θ	stiffness coefficient	2.6762
ρ_{SUEX} (kg/m^3)	density of air	1190.00
ρ_{air} (kg/m^3)	density of air	1.28
C_N	aerodynamic normal force coefficient	3.40
C_{rd}	aerodynamic rotational damping coefficient	5.00

Table 4.3.2. Selected LionFly actuator parameters and values

Parameter	Description	Value	
G_{act}	blocking force gain	328.29	$\mu N/V$
k_{act}	stiffness	658.83	N/m
m_{act}	mass	81.69	mg
x_{ref}	reference position	53.40	μm

The linear viscous damping terms are tuned to match the experiment in air and in vacuum. All other parameters are independently measured or calculated as stated earlier. The results show excellent agreement for the first mode, near 38 Hz. The response in vacuum is much larger than in air due to aerodynamic damping. The first flap and rotation natural frequencies are also reduced from vacuum to air, showing the effect of added aerodynamic inertia. The simulated and experimental results have the same decrease in natural frequency so the model accurately captures the added mass effect. The flap and rotation amplitudes and phases are roughly equal in the first mode, indicating strong coupling and potentially poor lift production, respectively. At this low level of excitation the aerodynamic forces are not sufficient to rotate the wing and change the zero degree relative phase between flap and rotation. It is therefore expected that the lift produced by this wing motion will be extremely low because the phase difference is far from the optimal value of 90 degrees [11]. The frequency response for the nonlinear sim-

Table 4.3.3. LionFly mechanism parameters and values

Parameter	Description	Value	
L_{AB}	length of coupler link	3.25	(mm)
L_{OA}	length of rocker link	0.75	(mm)
L_A	length of flexure hinge A	1.00	(mm)
L_B	length of flexure hinge B	0.25	(mm)
L_O	length of flexure hinge O	1.00	(mm)
r_4	vertical offset of slider	0.77	(mm)
t_f	mean flexure thickness	24.7	(μm)
k_A	stiffness of flexure hinge A	18.43	$(\mu N \cdot m)$
k_B	stiffness of flexure hinge B	73.73	$(\mu N \cdot m)$
k_O	stiffness of flexure hinge O	44.88	$(\mu N \cdot m)$
ϕ_0	initial ϕ angle	2.50	$(deg.)$
m_{mech}	mass	21.62	(mg)

ulation also matches the experimental results at low voltage. At each frequency point, the nonlinear simulation is run to steady state and the amplitude and phase calculated numerically. The vacuum results show that the nonlinear, linear, and experimental results all agree for the first mode, matching both magnitude and phase for both flap and rotation. The simulated results in air do not include the tuned aerodynamic damping of the linear model but match the linear and experimental data very well nonetheless. This validates the accuracy of the nonlinear aerodynamic model at low amplitudes.

The agreement between models and experiment at the second mode, near 135 Hz is also reasonable. The flap and rotation amplitudes and frequencies are slightly larger in vacuum than in air, again indicating the effects of aerodynamic drag and added mass. The model slightly over predicts the second natural frequency, probably due to unmodeled compliance in the LF1203 wing and mechanism. The second mode couples flap and rotation but rotation has a substantially larger amplitude relative to the first mode. Thus, the first mode is primarily a flap mode and the second is primarily a rotation mode but both are strongly coupled and cannot be accurately analyzed or understood with a decoupled model. Decou-

Table 4.3.4. LionFly wing parameters and values

Parameter	Description	Value	
R	wing span from O' to tip	20.10	(mm)
$\bar{c}$	mean chord	5.82	(mm)
A	area of wing	116.89	(mm^2)
x_r	x distance from O to O'	3.00	(mm)
y_r	y distance from O to O'	-0.21	(mm)
$\vec{r}_{cp_x}$	x distance from O to CP	13.43	(mm)
$\vec{r}_{tp_3}$	(x, y) distance from O to $\vec{r}_{tp_3}$	(10.47,-1.88)	(mm)
$\vec{r}_{tp_4}$	(x, y) distance from O to $\vec{r}_{tp_4}$	(11.60,-7.86)	(mm)
$\vec{r}_{tp_5}$	(x, y) distance from O to $\vec{r}_{tp_5}$	(22.87,-3.29)	(mm)
t_{tp}	effective thickness of PET test surface	75.04	(μm)
t_{vein}	average thickness of veins	250	(μm)
t_{mem}	average thickness of membrane	250	(μm)
t_ψ	flexure thickness of rotational hinge	25.74	(μm)
k_ψ	stiffness of wing rotational hinge	44.05	$(\mu N \cdot m)$
m_w	mass of wing	10.44	(mg)
m_s	mass of spar	8.62	(mg)
J_s	spar inertia about y axis	170.82	$(g \cdot mm^2)$
$J_{s_{am}}$	added spar inertia about y axis	1.40	$(g \cdot mm^2)$
J_{yy}	wing inertia about y axis	1738.17	$(g \cdot mm^2)$
$J_{yy_{am}}$	added inertia about y axis	117.84	$(g \cdot mm^2)$
J_{xy}	product of inertia about y axis	-461.07	$(g \cdot mm^2)$
$J_{xy_{am}}$	product of added inertia about y axis	-37.29	$(g \cdot mm^2)$
J_{xx}	wing inertia about x axis	175.17	$(g \cdot mm^2)$
$J_{xx_{am}}$	added inertia about x axis	14.14	$(g \cdot mm^2)$
$c_{\phi,vac}$	linear viscous damping of ϕ in vac	10.02	$(mN \cdot \mu m \cdot s)$
$c_{\phi,air}$	linear viscous damping of ϕ in air	19.60	$(mN \cdot \mu m \cdot s)$
$c_{\psi,vac}$	linear viscous damping of ψ in vac	4.46	$(mN \cdot \mu m \cdot s)$
$c_{\psi,air}$	linear viscous damping of ψ in air	5.70	$(mN \cdot \mu m \cdot s)$

pled analyses may be appropriate for systems with light wings where the rotation resonance is much higher than the flap resonance (10 times) but the stiffness is low enough to allow rotation under aerodynamic loading at the flap resonance. This is clearly not the case for LF1203. Although the two resonances are separated by a factor of three, both modes involve significant flap and rotation.

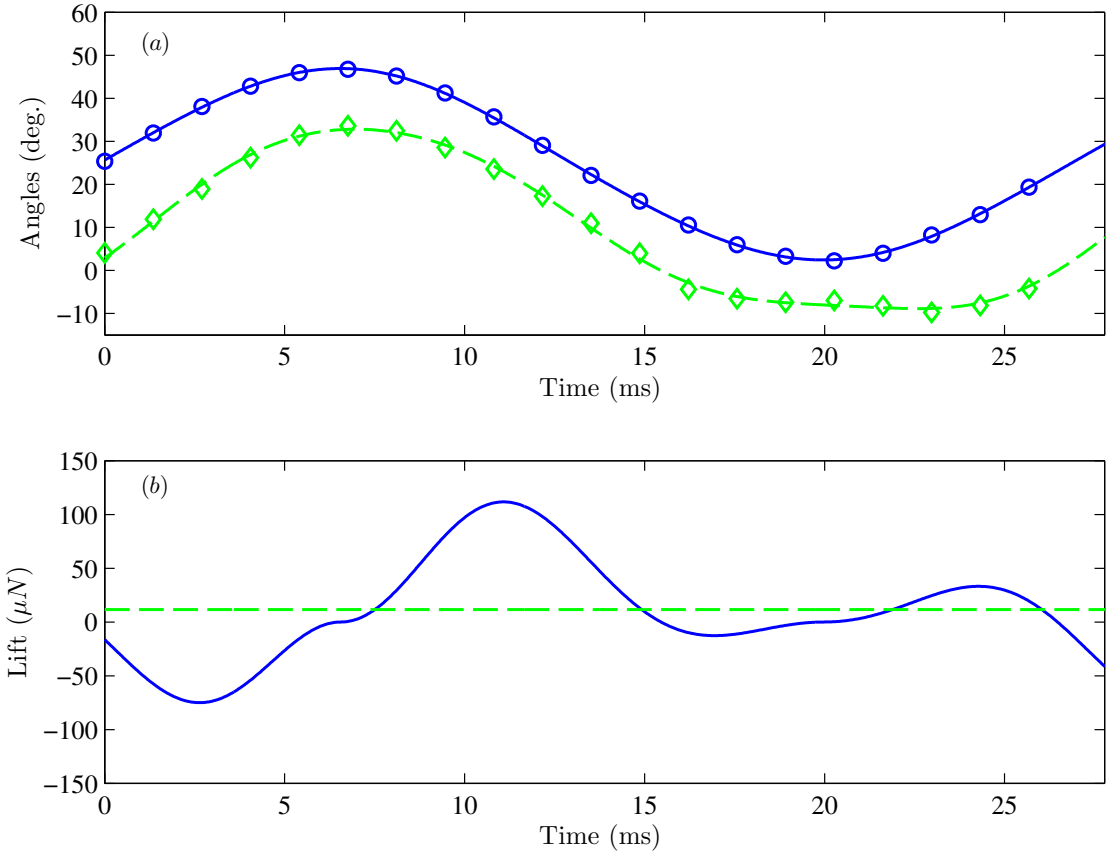

Figure 4.3.6. Stroboscopically photographed, image processed, and fitted flapping, $\phi(t)$ and rotation angles, $\psi(t)$, and calculated lift force (75 VDC/75 VAC) and 36 Hz: (a) Experimental $\phi(t)$ (circles) and $\psi(t)$ (diamonds) and fitted $\phi(t)$ (solid) and $\psi(t)$ (dashed), and (b) calculated lift force average (green dashed) and calculated using experimental $\phi(t)$ and $\psi(t)$ data (blue solid).

At higher actuation voltages, the laser vibrometer cannot be used for angle measurement, so stroboscopic photography and image processing measure the flap and rotation angles versus time. The wing trajectory points measured from photographs are linearly interpolated and fitted using the magnitude and phase from the highest four frequency components as calculated using the fast fourier transform. Figure 4.3.6(a) shows a time trace of one period of measured and fitted wing trajectories at 36 Hz. Figure 4.3.6(b) shows the lift calculated from the measured angle trajectories using Equations 4.27, 4.30, and 4.32. While the lift varies widely

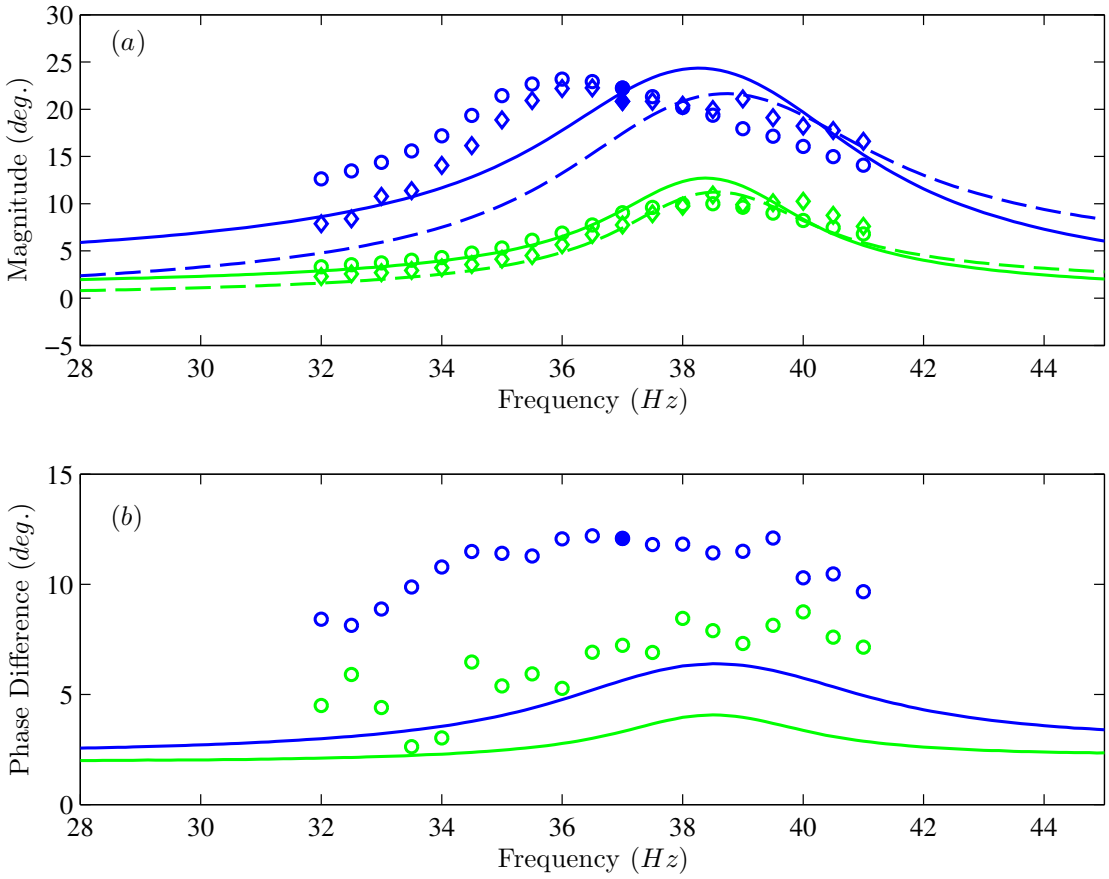

Figure 4.3.7. Experimental and simulated flapping, $\phi(t)$, rotation, $\psi(t)$, and relative phase, $\angle\phi(t) - \angle\psi(t)$, versus frequency: (a) experimental $\phi(t)$ (circles) and $\psi(t)$ (diamonds) amplitudes and simulated $\phi(t)$ (solid) and $\psi(t)$ (dashed) amplitudes at 75 VDC/75 VAC (blue), and 75 VDC/25 VAC (green), and (b) experimental relative phase (circles) and simulated relative phase (solid) at 75 VDC/75 VAC (blue) and 75 VDC/25 VAC (green). Data points corresponding to Figure 4.3.6(a) are filled.

during the cycle, the mean value is a small 11.52 μN. The reason for the low lift is that the $\phi(t)$ and $\psi(t)$ time trajectories are almost completely in phase at this frequency. The $\psi(t)$ trajectory lags the $\phi(t)$ trajectory by approximately 12.06 *deg.*, much less than the optimal value of 90 degrees that produces maximal lift.

Figure 4.3.7 shows the measured and simulated high voltage wing trajectories and relative phase difference between flapping and rotation under applied voltage of 75 V DC bias, and amplitudes of 25 V (75 VDC/25 VAC) and 75 V (75 VDC/75

VAC) versus frequency. The 23 *deg.* amplitude $\phi(t)$, 22 *deg.* amplitude $\psi(t)$, and 12 *deg.* relative phase results from Figure 4.3.6(a) are shown as filled symbols at 37 Hz. At 25 V, the peak wing angles occur at a resonance slightly higher than the low excitation resonance because the 75 V offset shifts the linearization point, slightly decreasing amplification, and thereby increasing resonance frequency. The nonlinearity of the mechanism is apparent in the shift in resonance frequency when amplitude is again increased in the ($75VDC/75VAC$) case. In both cases, flapping and rotation magnitudes are well predicted, however the phase differences are under predicted. The phase difference is highly dependent on the aerodynamic forces acting upon the wing, in which changes in center of pressure location and uncertainties in aerodynamic force coefficients contribute to error.

Figure 4.3.8 shows the average lift frequency response of the LionFly using experimentally measured lift, calculated lift from measured wing trajectories, and simulated lift. The 11.52 μN average lift result from Figure 4.3.6(b) is shown as the filled symbol at 36 Hz. The experimentally measured lift contains data from three runs at each applied voltage, showing consistent performance of the lift measurement system. The measured lift is larger than predicted by the calculated lift from wing trajectory data and simulation. Accuracy of measured lift depends strongly on the relative phase difference in the measured wing trajectory data, which is limited by temporal and pixel resolution. The Reynold's number approximated by $Re = (2\phi R\bar{c})/\nu$, where ν is the kinematic viscosity of air, $\nu \approx 20 - 26mm^2/s$, yields ≈ 1500, higher than the Reynold's number (≈ 100) used in finding aerodynamic coefficients in [11]. Additionally, unmodeled aerodynamic phenomena, such as rotational lift, wake capture, etc., could be responsible for these differences. Simulated lift values suffer from low magnitude as expected from the underpredicted phase data. Both the 25 V case and the 75 V case show maximum lift at a frequency slightly higher than the resonance observed in the wing trajectory data, due to increased relative phase difference with slightly off-resonance flapping and

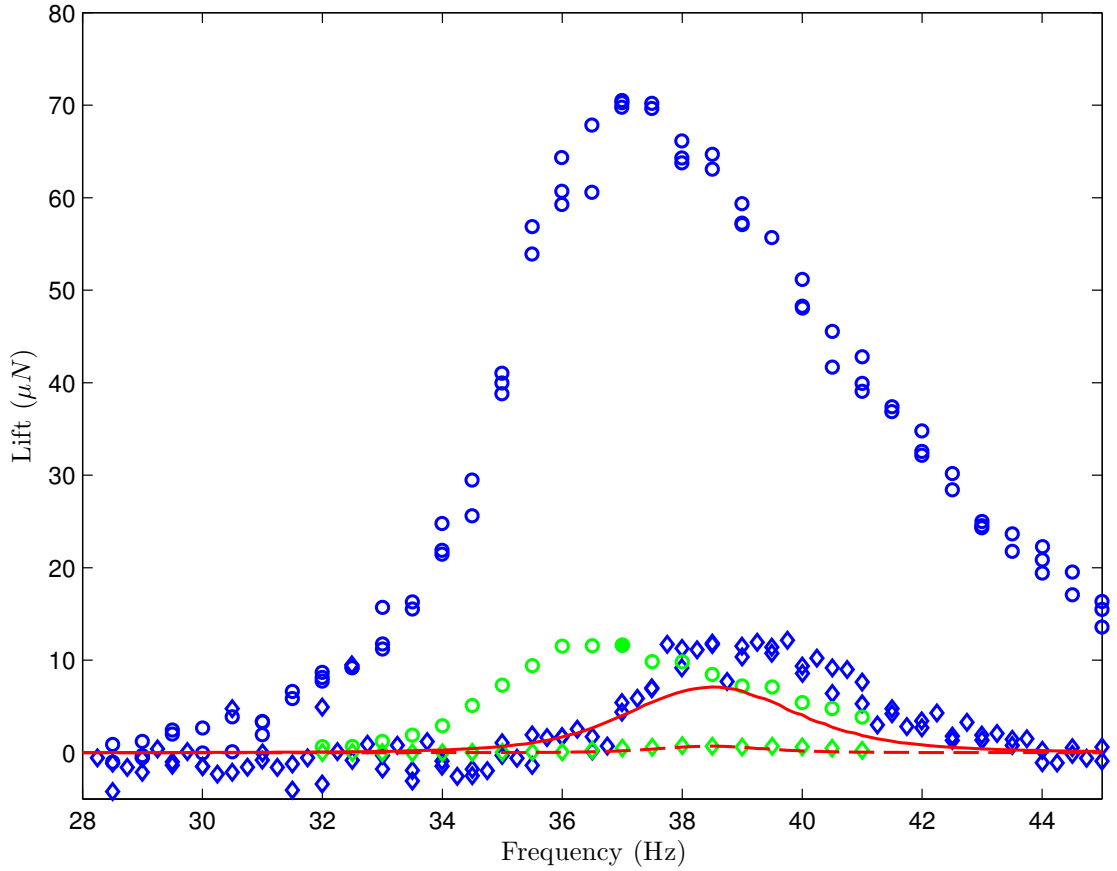

Figure 4.3.8. Average value lift versus frequency: experimentally measured lift (blue), calculated lift from wing measurement (green) at 75 VDC/75 VAC (circles), 75 VDC/25 VAC (diamonds), and simulated lift (red) at 75 VDC/75 VAC (solid) and 75 VDC/25 VAC (dashed). Data point corresponding to Figure 4.3.6 is filled.

rotation amplitudes. Despite uncertainties in aerodynamic parameters, the measured wing trajectories and lift validate the key criteria required for lift production: large flapping, rotation, and relative phase trajectories.

4.4 Model-Based Redesign

The lift generated by LF1203 is much smaller than what would be required to hover (1195 μN), not including the payload weight. The vehicle design is constrained by the current fabrication process that produces a minimum SUEX thickness of 20 μm.

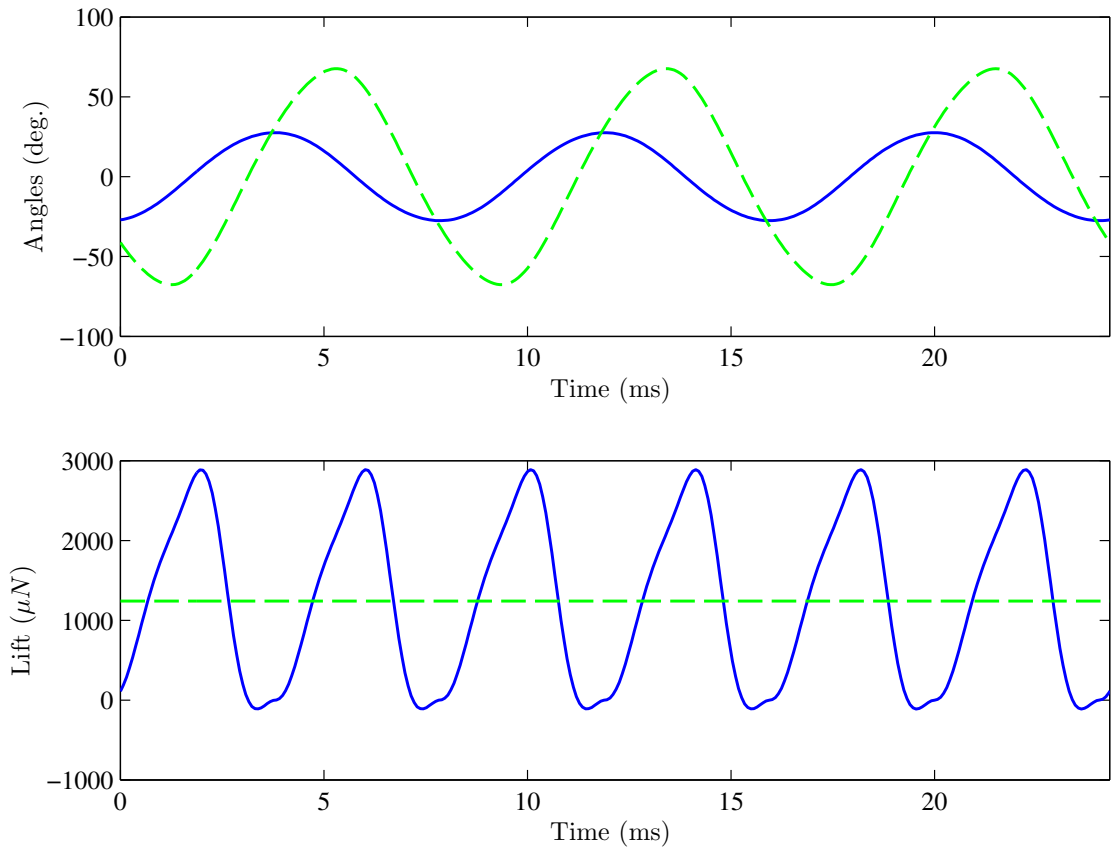

Figure 4.4.1. Simulated wing trajectories and lift force versus time of improved device of the redesigned LionFly at applied voltage of (0 VDC/ 300 VAC) and 123 Hz: (a) flapping, $\phi(t)$ (blue solid), and rotation, $\psi(t)$ (green dashed), (b) lift force, F_L (blue solid), and average lift (green dashed).

This minimum thickness is important because it governs the stiffness of the rotation hinge and the mass of the wing. Optimal lift production requires large wing flap and rotation and a phase difference of around 90 degrees. A thinner rotation hinge would allow larger rotation but lower the "rotation natural frequency, amplifying the modal coupling. The modal solutions typically do not provide good phase difference so this coupling must be overcome by the aerodynamics. To maintain a high rotation frequency, the mass of the wing must also be reduced. The mass of the wing, however, also dominates the flap natural frequency so it is not clear that the spectral separation between the two modes would be improved. In this

section, the LionFly is redesigned using the model to produce lift equal to its weight, enabling a hovering device in theory. This is by no means an optimized device and the previous section showed underprediction of lift by the model so the actual performance in practice may be better than predicted. The purpose of this section, however, is to demonstrate that if the constraints on the fabrication process are removed then a higher performing PAV becomes a possibility.

From the experiment, it is clear that the wing rotation of LF1203 is nearly in phase with flapping and aerodynamic forces are small compared to the wing inertia. If the wing inertia is reduced, resonance frequencies are increased, potentially increasing lift production. Fabrication of a wing with vein thickness of 30 μm and membrane thickness of 1 μm (much smaller than the 250 μm and 20 μm contraints of the LF1203 fabrication process), wing mass can be reduced from 10.4 mg to 1.35 mg, reducing the inertia accordingly. A second design change is the specification of an initial flap angle of 45 deg. This is difficult to dial in exactly using the current process so DC voltages are applied to adjust the initial flap angle. Specifying an initial flap angle of 45 deg provides a wide operating range and lower amplification factor. The reduced amplification factor raises the resonance frequencies, a positive result, but also increases the required voltage to obtain the desired flap amplitude, a negative result. The overall voltage amplitude is therefore increased to 300V, within the operating range of the LF1203 bimorph. The final design change is a reduction in the rotational flexure thickness, $t_\psi = 7.5$ μm, and the flexure length, $L_\psi = 352$ μm. These three design changes greatly improve the amplitudes and relative phase, potentially leading to higher lift production.

Figure 4.4.1 shows the simulated flapping and rotation wing trajectories versus time at the maximum average lift frequency of the redesigned LionFly (123 Hz). Compared with Figure 4.3.6, significant phase shift between flapping and rotation combined with large rotation angles should lead to much larger lift forces. The increased resonance frequency also quadratically increases aerodynamic forces.

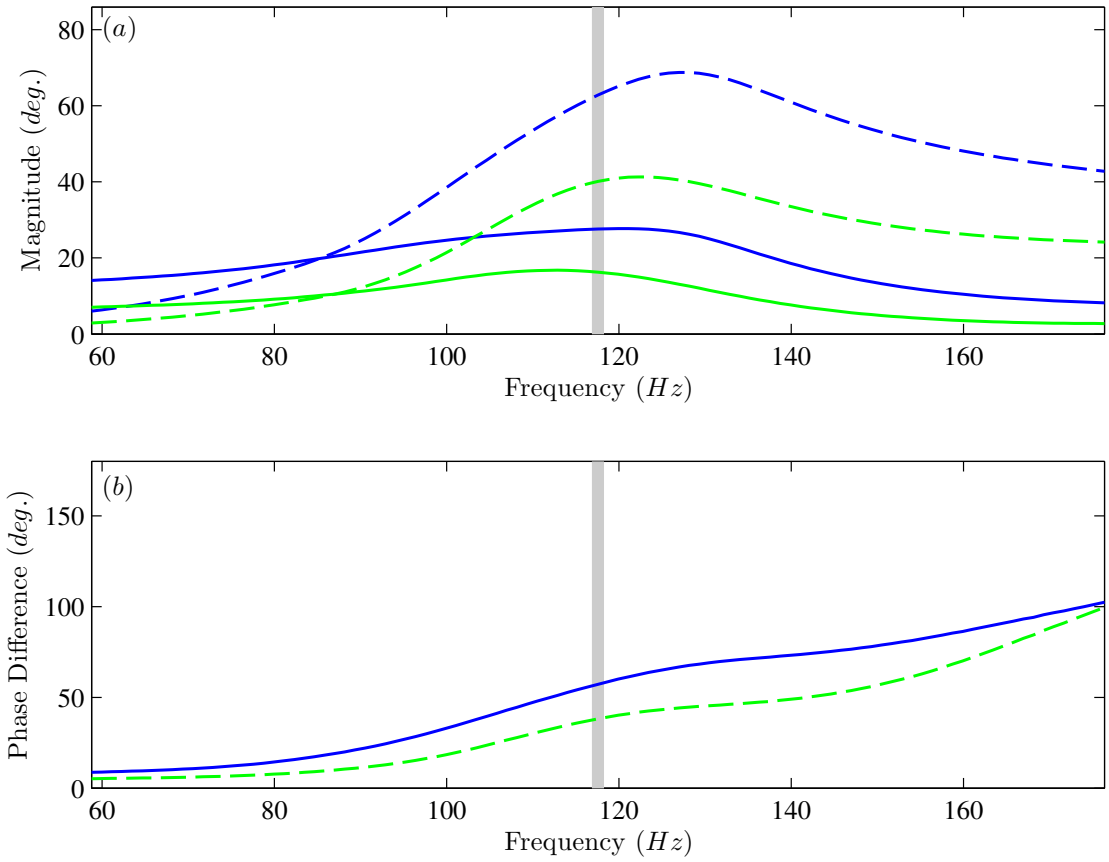

Figure 4.4.2. Simulated flapping, $\phi(t)$, rotation, $\psi(t)$, and relative phase, $\angle\phi(t) - \angle\psi(t)$, versus frequency for the redesigned LionFly (0 VDC/ 300 VAC - blue and 0 VDC/ 150 VAC - green): (a) $\phi(t)$ (solid) and $\psi(t)$ (dashed), and (b) relative phase. The flapping resonance frequency is highlighted at 117 Hz (gray shaded).

Figure 4.4.2 shows the simulated high voltage frequency reponse of the redesigned LionFly using applied voltages of 150 VAC and 300 VAC. These results show much larger rotation, similar flapping, and most importantly, the larger relative phase compared to LF1203.

Figure 4.4.3 shows the simulated lift frequency response, with peak lift at 1250 μN. The peak lift occurs at a frequency slightly above the flapping resonance, similar to the experiment. This effect increases as a function of voltage amplitude. The simulated lift brings the LionFly within a lift to weight ratio of one, theoretically allowing the device to hover.

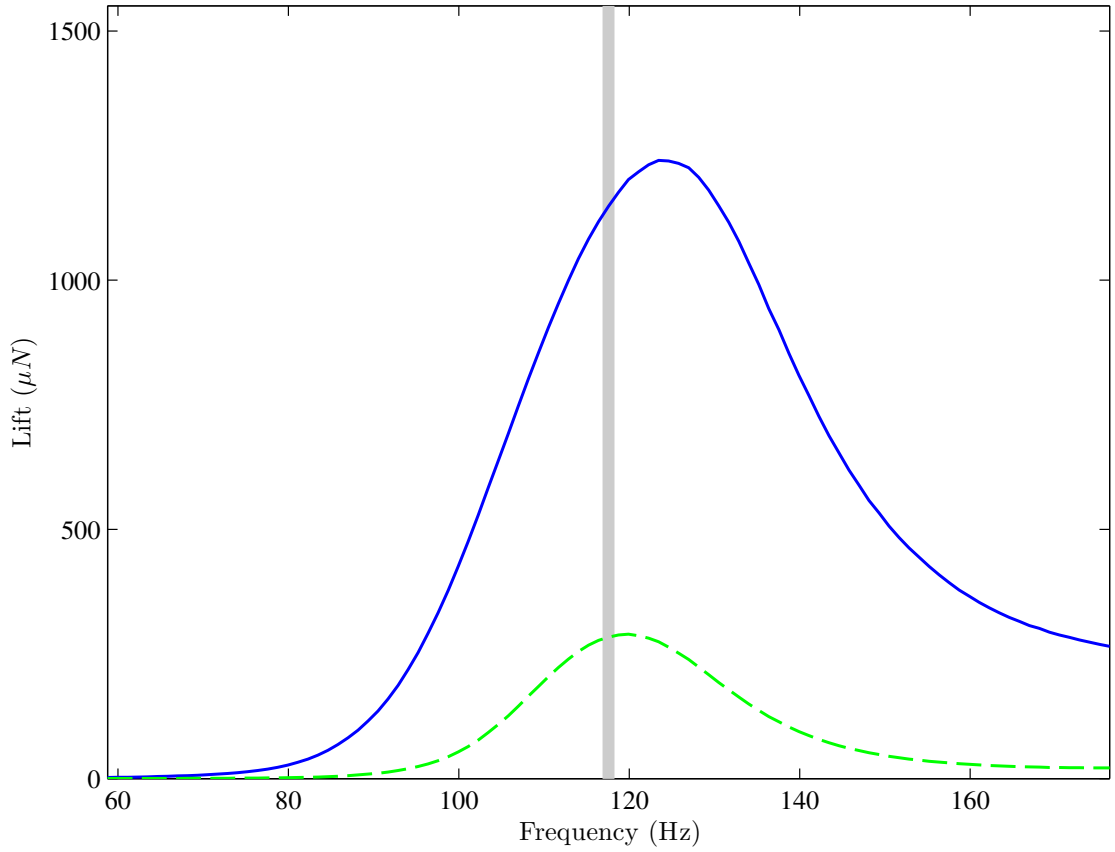

Figure 4.4.3. Simulated average steady state lift versus frequency of the redesigned LionFly (0 VDC/ 300 VAC - blue and 0 VDC/ 150 VAC -green). The flapping resonance frequency is highlighted at 117 Hz (gray shaded)

Chapter 5

Conclusions and Future Work

In this work, the design, fabrication, modeling, and experimental validation of an NAV scale clapping wing mechanism is presented. A flexure hinge allows passive wing rotation for the clapping wing mechanism that has the potential to increase thrust. Analytical models of wing flapping and rotation are derived and validated using experimental wing trajectory results. The Penn State NAV prototype is experimentally shown to provide approximately 54◦ peak to peak wing rotation, 14◦ peak to peak flapping angle, and 0.21 mN of thrust at 9.5 Hz. At 25.5 Hz, the prototype produces a maximum of 1.34 mN of thrust. The PSNAV model accurately predicts the wing resonances in the experimental prototype. Model-predicted thrust is lower than the experimentally measured values, however.

This work also presents a simple, low cost, precise, and rapid process for monolithic fabrication of SUEX™ dry film to prototype PAV mechanisms and wings. Several LionFly prototypes were fabricated and experimentally tested. Theoretical and experimental results have excellent agreement validating the compliant mechanism kinematics and aerodynamic added mass and damping. High voltage tests show a flapping angle of 55° at 150 V amplitude peak to peak with 150 V DC offset at 51 Hz resonance. The results demonstrate the potential of this process to fabricate PAV scale flapping mechanisms and wings, and the ability of the mech-

anism to amplify the small displacement of the piezoelectric bimorph into large flapping angle. Consistent performance from multiple prototypes demonstrate the reliable and repeatable nature of the fabrication process.

Finally, this work presents detailed modeling and experimental testing of the flapping and rotation dynamics, and the lift producing mechanisms in the LionFly. The linear vibration model augmented with nonlinear aerodynamic forces was validated using experimental testing with a laser vibrometer and accurately predicts small amplitude wing dynamics in air and vacuum. At higher amplitudes, the model can sufficiently predict wing trajectory amplitudes, but phase measurement and simulation have slight error. The LionFly produces 46 *deg*. flap and 44 *deg*. rotation amplitude peak to peak with relative phase of 12 *deg*., and maximum lift of 71 μN at 37 Hz. Calculated lift values using measured wing trajectories and simulated lift values underpredict measured lift. Sensitivity to phase measurement, unmodeled aerodynamic mechanisms, and uncertainty in aerodynamic parameters each contribute to error. Despite this, the measured wing trajectories and lift validate the key criteria required for lift production: large flapping, rotation, and relative phase trajectories. By reducing the inertia of the wing and tuning the rotational hinge stiffness, a redesigned device is simulated to produce lift to weight ratio of one.

5.1 Future Work

5.1.1 Fabrication

The current fabrication process has many advantages in simplicity, time, and cost. Using the validated model, we have shown that reducing the membrane thickness to 1 μm along with wing venation to 30 μm will cause a significant increase in performance. However, the thickness range for the thin region is between 20 - 75 μm. The minimum thickness, found through a reduction of yield due to membrane

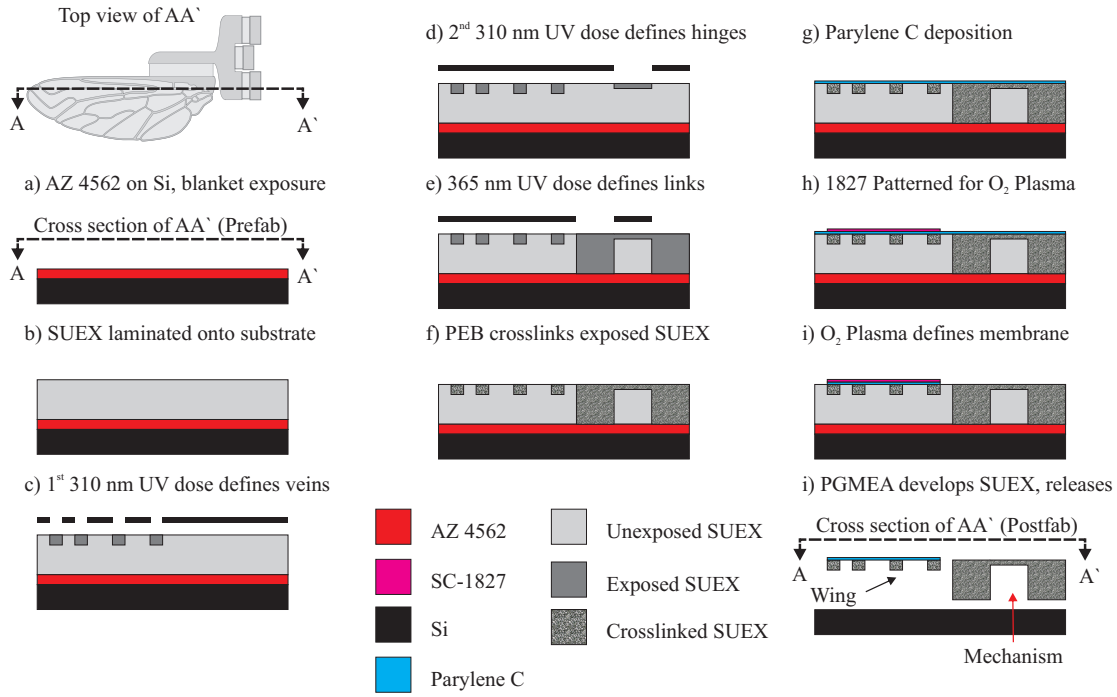

Figure 5.1.1. Potential fabrication process for PAV flapping wing mechanisms: a) prepare of Si wafer with an AZ 4562 sacrificial layer, b) laminate SUEX onto substrate, c) define venation through 310 nm UV dose, d) define flexure hinges through $2^n d$ 310 nm UV dose, e) define links through 365 nm UV dose, f) crosslink SUEX through post exposure bake at 65°C for 30 minutes, g) 1 μm parylene C deposition, h) pattern SC-1827 to mask membrane (spin SC-1827, soft bake at 95°C for 2 minutes, expose using 310 nm UV dose, develop in acetone, N_2 dry), i) oxygen plasma removes undesired parylene C, j) develop and release in PGMEA, dry using N_2 and a 50°C vacuum oven.

perforation, is feature size dependent and is strongly correlated to stress that develops during the post exposure bake. More characterization and tests need to be conducted to better understand this issue. Alternatively, the process could be modified to include a separate material for the 1 μm membrane layer.

Figure 5.1.1 shows a potential fabrication process to implement the design changes proposed in section 4.4. The previous process only used photolithography which allowed SUEX to be used as a substrate. In this process, SUEX must be laminated to a substrate for additional processing. The process begins with preparing a sacrificial layer for releasing the device, shown in Figure 5.1.1 a). AZ

4562 has recently been used as a sacrificial layer in SU-8 processing [80] and is much simpler to use than other sacrificial layers such as aluminum which must be deposited by sputtering or evaporation. The SUEX must be hot roll laminated onto the AZ 4562/Si substrate shown in Figure 5.1.1 b). The vein layer and the flexure hinge layer can both be defined using different 310 nm UV doses as shown in Figure 5.1.1 c) and d), respectively. Figure 5.1.1 e) shows the rigid link definition using 365 nm UV dose. The post exposure bake in Figure 5.1.1 f) at 65°C for 30 minutes crosslinks the SUEX. Parylene C is a suitable candidate for membrane material because it is easily deposited at room temperature at thicknesses of 1 μm and can withstand the chemical development used for SUEX. Figure 5.1.1 g) shows the parylene C deposition, and Figure 5.1.1 h) shows patterned SC-1827. This step involves spinning SC-1827, soft baking The membrane must be defined using an oxygen plasma etch, which requires a masking layer of SC-1827. The 1 μm parylene layer will etch rather quickly in comparison to the approximately 3 μm layer of photoresist, forming the wing membrane in Figure 5.1.1 i). The final development in PGMEA dissolves the uncrosslinked SUEX and AZ4562, simultaneously releasing the device. The device is dried using N_2 and a vacuum oven at 50°C vacuum oven.

This potential process assumes SUEX will not be negatively affected by the SC-1827 soft bake temperatures, exposure, or O_2 plasma. The SC-1827 data sheet soft bake temperature of 110°C can be adjusted to 95°C with extra time to be within reported values for PEB of SUEX. The exposure dose required for SC-1827 is an order of magnitude smaller than SUEX, and no post exposure bake is conducted subsequently so no undesired crosslinking of SUEX should occur. Defining the parylene C layer using the O_2 plasma could require tuning of SC-1827 thickness and etch time. This process presents one possible solution to utilize the current benefits without significant increase in processing steps.

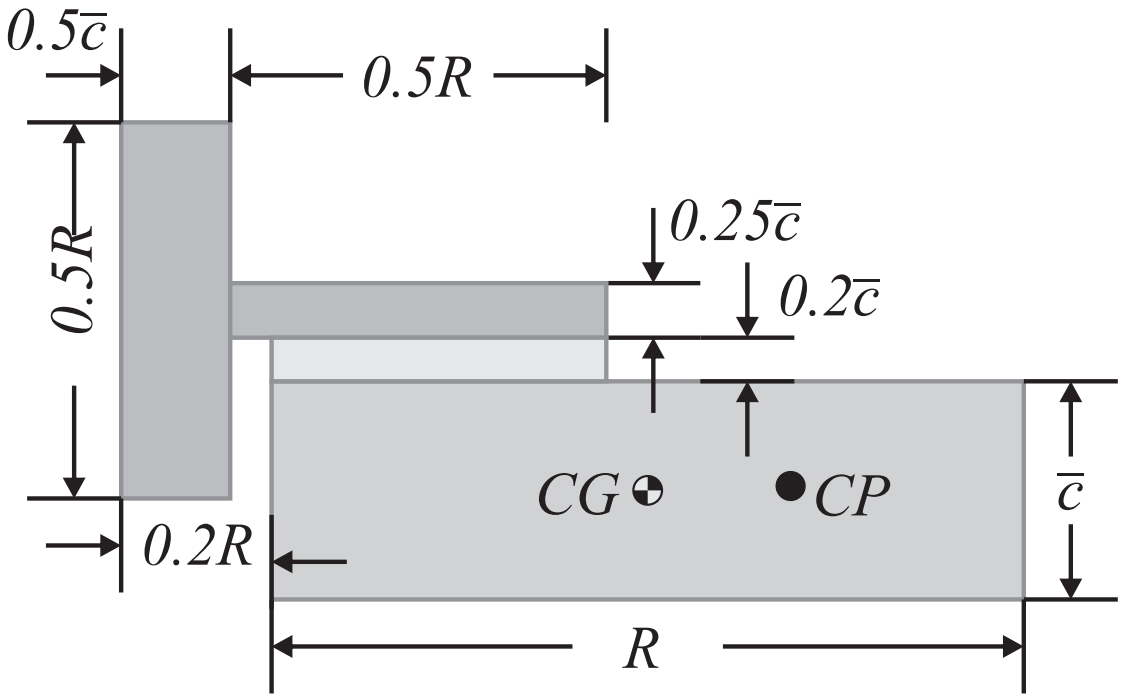

Figure 5.1.2. Parameterization schematic of simplified Lionfly wing design

5.1.2 Design

Optimizing the wing under the current fabrication constraints would be invaluable for future prototypes. To explore the design space, simplifying the wing, spar, and rotational hinge allows parameterization based on a few variables. Based on the current prototype, a simplified, rectangular design can be formed as a function of wing span, R, and average chord, $\bar{c}$, by Figure 5.1.2. For a constant aspect ratio, AR, the average chord can be written as, $\bar{c} = R/AR$. The wing planform has thickness, t_{avg}, and the inertia matrix is

$$\mathbf{J} = t_{avg} R^4 \begin{bmatrix} 157.31 & 34.87 \\ 34.87 & 10.76 \end{bmatrix}. \tag{5.1}$$

(5.2)

The aerodynamic moments on acting on ϕ and ψ rewritten in terms of R are

$$M_\phi = R^5 \left(0.1876\dot{\phi}|\dot{\phi}| \cos^2(\psi)\cos(\phi)\right), \tag{5.3}$$

$$M_\psi = R^5 \left(0.0396\cos(\psi)\dot{\phi}|\dot{\phi}| + 0.0117\dot{\psi}|\dot{\psi}|\right). \tag{5.4}$$

This shows that the inertia terms have a R^4 dependence while the aerodynamics have a R^5 dependence. The rotational hinge stiffness, k_ψ, determined strongly by the flexure thickness, t_ψ, is another design variable which can be used in optimization. Selecting an appropriate t_{avg}, t_ψ between 20 to 75 μm, the current model can be used to find an optimal wing span for a fixed actuator and mechanism.

Further optimization would include the design space of the actuator and mechanism which govern the flapping degree of freedom stiffness, k_ϕ, amplification, a, bimorph force gain, G_{act}, and the majority of the PAV weight budget. These terms are inherently coupled and more investigation is needed to determine PAV performance limits including actuator and mechanism.

Appendix A

Piezoelectric Materials and Actuators

A.1 Piezoelectric Actuators

Piezoelectric actuators have found many applications in macroscale applications such as walking microrobots [81], cooling fans [82], inkjet printers [83], and microscale applications such as RF MEMS switches [84], micropumps [85], and MEMS gyroscopes [86], for example. Historically, piezoelectric materials have been used for ultrasonic transducers, resonators, and accelerometers. This section gives a brief background of piezoelectric materials, and describes the static and dynamic function of multilayer beam bending actuators and novel T-beam actuators.

A.1.1 Piezoelectric Materials

Piezoelectric materials have the ability to convert mechanical energy to electrical energy (direct effect) and vice versa (indirect) and are available in many forms. Quartz, lead zirconate titanate (PZT), $(1-x)Pb(Mg_{1/3}Nb_{2/3})O_3-xPbTiO_3$ (PMN-PT) and polyvinylidene diflouride (PVDF) are examples of a piezoelectric crystal, ceramic, relaxor-ferroelectric and polymer. Figure of merits for these piezo-

electric materials include piezoelectric coefficients, electromechanical coupling coefficient, and quality factor. The linear piezoelectric constitutive equations relate the electromechanical properties of the material

$$D_i = d_{ij}\sigma_j + \epsilon_{ii}^T E_i \tag{A.1}$$

$$S_j = s_{ij}^E \sigma_j + d_{ij} E_i, \tag{A.2}$$

where S_j is the mechanical strain, σ_i is the mechanical stress, E_i is the electric field, D_i is the electrical displacement, s_{ij}^E is the elastic compliance at zero electric field, and ϵ_{ii}^T is the permittivity at zero stress. The piezoelectric coefficients, d_{ij}, are third rank tensors which in reduced tensor notation correspond to a 3×6 matrix[50]. In this reduced notation, the indices $(i = 1 - 3)$ define normal electric displacement orientation, $(j = 1 - 3)$ define normal mechanical strains and $(j = 4 - 6)$ represent shear strains.

The electromechanical coupling coefficient can be thought of as energy conversion effectiveness, and is defined as the square root of the ratio of stored mechanical (electrical) energy over input electrical (mechanical) energy[83]. It can also be written as[52]

$$k_{ij}^2 = \frac{d_{ij}^2}{\epsilon_{jj}^T s_{ii}^E} \tag{A.3}$$

Mechanical quality factor is inversely proportional to the intensive mechanical loss, $(\tan\delta')$, of the material. It determines the sharpness of the frequency response of a piezoelectric material and is important in resonance applications. At the macroscale, bulk crystals and ceramics are typically used. Microscale sensors and actuators can be micromachined from bulk material or deposited using thin films (just PZT).

PZT and PMN-PT are considered ferroelectric materials, which have a spontaneous polarization which can be reversed by an electric field. These materials have

a Curie temperature, above which it will lose its polarization. This however can be reverse by re-poling the material with an applied field while near or above its Curie temperature, and allowing the material to cool. The material can also lose its polarization due to an applied field higher than its coercive field, or stress which would induce this field. Ferroelectric materials are useful piezoelectrics because the polarization can be designed for different actuator configurations, however the operating temperature must be, in general, at least one half of the Curie temperature.

PZT has seen more applications because of its ease of fabrication either in bulk or thin film form. Despite their great piezoelectric properties, PMN-PT and other relaxor ferroelectric materials suffer from high cost, low Young's modulus and fracture toughness. PZT-4 and PZT-5H are different formulas of PZT which can be considered a "hard" or "soft" piezoelectric material, respectively. In general "hard" piezoelectrics will have higher quality factor, show more linearity, and be best suited for resonance applications. "Soft" piezoelectrics on the other hand, will have much better off-resonance performance but show significant hysteresis[50] and much lower Curie temperature. PZT-5H has been popular in NAV actuator applications[44, 53].

The indirect piezoelectric effect is used for piezoelectric actuation. If there is no applied stress, Eq. **??** can be simplified to A.4

$$\epsilon_j = d_{ij} E_i \tag{A.4}$$

where ϵ_j is the mechanical strain and E_i is the applied electric field. Typically, the index 3 is used to indicate the direction of poling. So, an applied field in the direction of poling, E_3 will cause an induced strain, ϵ_3 or ϵ_1, proportional to the d_{33} and d_{31} coefficients, respectively. Stack actuators use the d_{33} which is about three times larger than the d_{31} and is capable of produce large forces but very small displacement. To increase displacement, flextensional and cantilever beam

actuators are used. Flextensional piezoelectric actuators, such as the moonie, cymbal, and recent uniflex[87] use an elastic element to amplify displacement. These actuators use the d_{31} coefficient to amplify tip displacement along the length of the beam. The following section gives a background of cantilever beam bending actuators.

A.1.2 Cantilever Beam Bending Actuators

Typical PZT cantilever beam bending actuators are in a unimorph or bimorph configuration. In a unimorph, one piezoelectrically active layer bonds to another passive layer. An applied field in the polarization direction will cause contraction in the active layer while the passive layer resists the deformation causing upward bending in the beam. Bimorphs either replace the passive layer with a piezoelectrically active layer, or add a piezoelectric layer as the bottom layer. and are configured such that when the upper layer contracts, the bottom layer expands, increasing the performance of the actuator. Since the strain induced in the material is electric field induced, the voltage required to actuate is dependent on the thickness of the piezoelectric layer. To reduce this operating voltage, multiple thin layers can be bonded in either unimorph or bimorph configuration to form multilayer beam bending actuators[88] cite Ballas's book too.

Unimorph. bimorph, and multilayer beam bending actuators have been studied extensively. Models of the static and dynamic operation will be presented here for completeness. In addition to the geometry of the piezoelectric layer, the material choice and thickness of the passive layer is quite important, and many studies have been conducted on this topic. The following sections describe the static and dynamic operation of bimorph actuators.

Free tip displacement, blocking force at the tip, and stiffness are important for the static operation of piezoelectric actuators. The static free displacement and

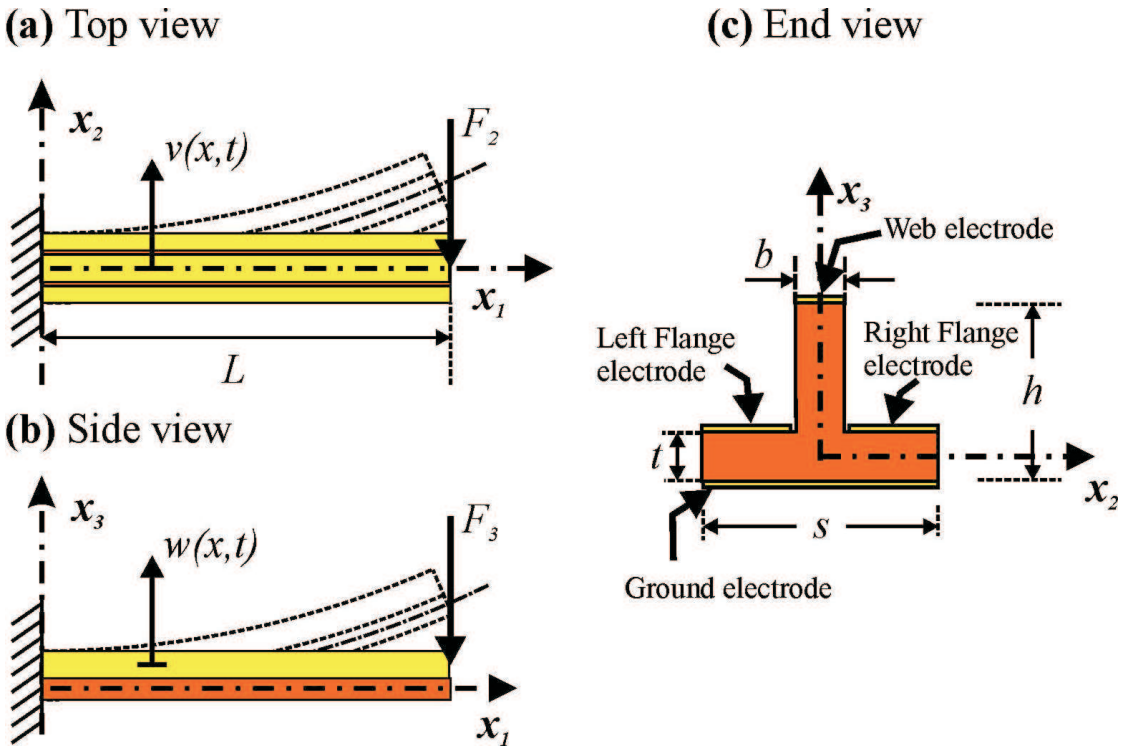

Figure A.1.1. Schematic of T-beam cantilever beams: (a) top view showing in-plane displacement $v(x,t)$ and tip force F_2, (b) side view showing out-of-plane displacement $w(x,t)$ and tip force F_3, and (c) end view showing cross section of T-beam with design parameters b, web width, t, flange thickness, s, total width, and h, total thickness

blocking force equations of a bimorph with center shim are[74].

$$\delta_f = \frac{3d_{31}L^2V}{2(t_{pzt}+t_{shim}t_{pzt})}\frac{(B+1)(2B+1)}{AB^3+3B^2+3B+1} \tag{A.5}$$

$$F_B = \frac{3d_{31}E_{pzt}w(2t_{pzt}+t_{shim})^2V}{8Lt_{pzt}}\frac{2B+1)}{(B+1)^2} \tag{A.6}$$

where $A = E_{pzt}/E_{shim}$ and $B = t_{pzt}/t_{shim}$. The stiffness of a a bimorph found as $k = F_B/\delta_f$. The center shim is required to be electrically conductive, and the bimorph can be driven in multiple configurations.

A.1.3 T-beam Actuators

When fabricating cantilevers using PZT film deposition, unwanted curvature due to residual film stress and/or thermal expansion coefficient mismatch can occur [14, 18]. For certain applications, such as RF switches and optical alignment, obtaining flat cantilevers is crucial. It is possible to compensate for the curvature during the design process, however it requires precise knowledge of material parameters[19] which can be difficult in practice. A more robust method of creating flat cantilevers is by increasing the substrate thickness to withstand the residual stress at the expense of tip displacement[20]. This however leads to suboptimal designs for the sake of a flat device. Recent advances in high aspect ratio deep reactive ion etching processes [27-29] have made possible monolithic fabrication of cantilever T-beam actuators from bulk PZT. These actuators have T-shaped cross section that can produce out-of-plane displacement without the need to bond or deposit multiple layers[22].

A.1.3.1 Operation

subsection A.1.3 shows a T-beam cross section with design arameters of web width, b, flange thickness, t, total width, s, and total height, h. Electrodes are deposited on the top and bottom of the web and flange regions. The T-beam can provide in-plane and out-of-plane displacement by selective activation of the web and flange electrode. The PZT is poled through the thickness from top to bottom, with the bottom electrode acting as ground. Assuming uniform electric field, a positive electric field applied to the web in the direction of poling causes the web region to expand through the thickness and contract longitudinally by the d_{31} piezoelectric coefficient. Similar to the passive layer in a unimorph, the flange regions remain essentially piezoelectrically inactive, constraining the lower part of the T-beam, forcing the beam to bend upwards. Similarly, activating both flange electrodes contracts the flange region while the web region resists contraction forcing the beam

to deflect downwards. Activation of a single flange causes an in-plane deflection. Analytical models of the in-plane and out-of-plane static T-beam tip displacement in response to applied voltage on the web and flange electrodes have been developed [89] and included here for completeness. The in-plane, v_f, and out-of-plane, w_f, free tip displacement in response to an applied voltage, V, is given by

$$v_f = \frac{A_{p2} d_{31} L^2 V}{4 I_2 t} \tag{A.7}$$

$$w_f = -\frac{z E A_p d_{31} L^2 V}{E I_{3,eff}} \tag{A.8}$$

The in-plane, F_{2b}, and out-of-plane, F_{3b}, blocking force is given by

$$F_{2b} = -\frac{3 E A_{p2} d_{31} V}{2 L t} \tag{A.9}$$

$$F_{3b} = \frac{3 z E A_p d_{31} V}{2 L} \tag{A.10}$$

where the distance from the top of the flange to the neutral axis is

$$e = \frac{t^2 s - t^2 b + 2tbh - bh^2}{2(ts - tb + bh)}$$

the active piezoelectric cross sectional area, A_p, first moment of area about the x_2 axis, A_{p_2}, area moment of inertia about the x_2 axis, I_2, and effective area moment of inertia about the x_3 axis, I_{eff} are given in table 1. The Young's modulus, E, piezoelectric strain coefficient, d_{31}, permittivity, ϵ_{33}, and electromechanical coupling coefficient of PZT-4, calculated by $k_{31} = (E d_{31}^2)/\epsilon_{33}$, are given in Table A.1.2. T-beam cross sections have been optimized for displacement, blocking force and mechanical energy output[22]. Define $b^* = b/s$, and $t^* = t/s$ as the web and flange ratio, respectively. Maximum displacement is achieved as b* and t* approach 0. There exists an optimal ratio for maximum blocking force, $b^* = 0.381, t^* = 0.381$, and maximum mechanical energy output, $b^* = 0.25$, $t^* = 0.33$. This will be useful

Table A.1.1. Geometric Parameters of T-beam

Web	Dual flange	Single flange	
z	$\frac{2e+h-2t}{2h}$	$\frac{2e-t}{2t}$	$\frac{2e-t}{2t}$
A_p	bh	$t(s-b)$	$\frac{1}{2}t(s-b)$
A_{p2}	0	0	$\frac{1}{8}t(s^2-b^2)$
I_{b2}	$\frac{t}{12}(s^3-b^3)$	$\frac{b^3h}{12}$	$\frac{1}{24}((2h-t)b^3+ts^3)$
I_{p2}	$\frac{b^3h}{12}$	$\frac{t}{12}(s^3-b^3)$	$\frac{t}{24}(s^3-b^3)$
I_{b3}	$\frac{(s-b)t^3}{12}$ $+A_b(e-\frac{t}{2})^2$	$\frac{bh^3}{12}$ $+A_b(e-t+\frac{h}{2})^2$	$I_{p3}+\frac{bh^3}{12}$ $+bh(e-t+\frac{h}{2}$
I_{b3}	$\frac{bh^3}{12}$ $+A_b(e-t+\frac{h}{2})^2$	$\frac{(s-b)t^3}{12}$ $+A_b(e-\frac{t}{2})^2$	$I_{p3}+\frac{bh^3}{12}$ $+bh(e-t+\frac{h}{2}$
$I_{3,eff}$	$(1+k_{31}^2)I_{p3}+I_{b3}$ $-k_{31}^2h^2z^2A_p$	$(1+k_{31}^2)I_{p3}+I_{b3}$ $-k_{31}^2t^2z^2A_p$	$(1+k_{31}^2)I_{p3}+I_{b3}$ $-k_{31}^2h^2z^2A_p$

in designing T-beam actuators for applications in Nano Air Vehicles.

A.1.4 Static and Dynamic Modeling of T-Beam Actuators

This work presents static and dynamic modeling and testing of PZT-5H T-beam actuators. Macroscale T-beams have been used in flapping wing mechanisms driven statically[90] and at resonance[91]. The results of this work can also be applied to microscale T-beams where the fabrication process is particularly advantageous. Dynamic modeling of PZT-5H T-beam actuators allows the T-beam to be integrated into flapping wing mechanism modeling for Nano Air Vehicle (NAV) applications.

A.1.4.1 Fabrication and Experimental Setup

T-beam actuators are fabricated from 1 mm thick, finely polished, Cr/Au electroded, bulk PZT-5H using a high precision dicing saw. The cross section of the T-beam has web width b, total width s, flange thickness t, and total thickness h as shown in subsection A.1.3(c). The material properties and T-beam dimensions

Table A.1.2. PZT-5H Material Properties[1]

Property	PZT-4	PZT-5H
Young's Modulus, E, (GPa)	78	64
Piezoelectric Strain Coefficient, d_{31}, (pm/V)	-122	-265
Relative Permittivity, ϵ_{33}/ϵ_0	1700	3400
Density, (kg/m^3)	7600	7500

are shown in Table A.1.2. After the T cross sections are realized, the individual T-beams are mounted onto a glass base using two part epoxy, and wires are soldered to the web and bottom electrode. For ease of handling the base is then bonded to 4 mm thick FR4 PCB board material which can be mounted onto a Newport linear stage as shown in Figure A.1.2. The T-beams are poled through the thickness of the web region using 2 $V/\mu m$ in 80 ℃ peanut oil for 30 minutes and then cleaned using acetone, isopropyl alcohol, and detergent. A Model 609E-6 high voltage Trek amplifies input signals from a LabVIEW system. A Polytec laser vibrometer with a 25 μm diameter laser point measures static tip displacement on the T-beam. An Aurora force transducer with a 1 mm diameter glass tube measures blocking force. The T-beam is clamped to a Newport linear stage using the FR4 board and precisely positioned for measurement while LabVIEW records all data. Figure **??** shows a photograph of the mounted beam, the laser vibrometer used for displacement measurement, and the load cell used for force measurement.

A.1.4.2 Static Results and Modeling

During the blocking force measurement, slight flexibility of the FR4 board was observed using the laser vibrometer. This softening of a perfectly clamped boundary condition can be modeled as a free-free beam with a rotational and translational spring at the base, as shown in Figure A.1.4. The Cartesian coordinates x and z denote the position along the length and through the thickness of the beam,

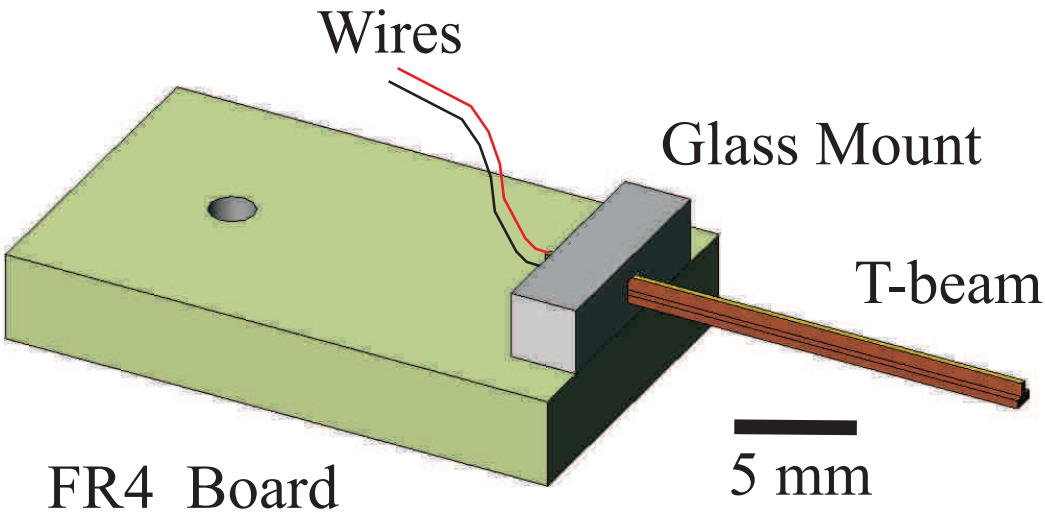

Figure A.1.2. Schematic of T-beam mounted onto glass base and FR4 board

Table A.1.3. T-beam Model Parameters

Constant	Expression
a_2	$\frac{1}{2}E\left(1+\frac{Ed_{31}}{\epsilon_{33}}\right)$
a_3	$-\frac{(Ed_{31})^2(2e+h-2t)^2}{8\epsilon_{33}}$
a_4	$-\frac{Ed_{31}(2e+h-2t)}{2h}$
a_5	$-\frac{\epsilon_{33}}{2h^2}$
A_b	$t(s-b)$
A_p	bh
I_b	$\frac{(s-b)t^3}{12}+A_b\left(e-\frac{t}{2}\right)^2$
I_p	$\frac{bh^3}{12}+A_p\left(e-t+\frac{h}{2}\right)^2$
K_V	$-\frac{2e+h-2t}{2h}EA_pd_{31}$
I_{eff}	$(I_b+I_p)+\frac{Ed_{31}^2}{\epsilon_{33}}\left(I_p-A_p\frac{(2e+h-2t)^2}{4h^2}\right)$

respectively. Only the transverse displacement of the beam will be considered and is denoted by $w(x,t)$. The centroidal axis location can be calculated from the T-beam cross section parameters, at a distance

$$e=\frac{1}{2}\frac{t^2s-t^2b+2tbh-bh^2}{ts-tb+bh} \tag{A.11}$$

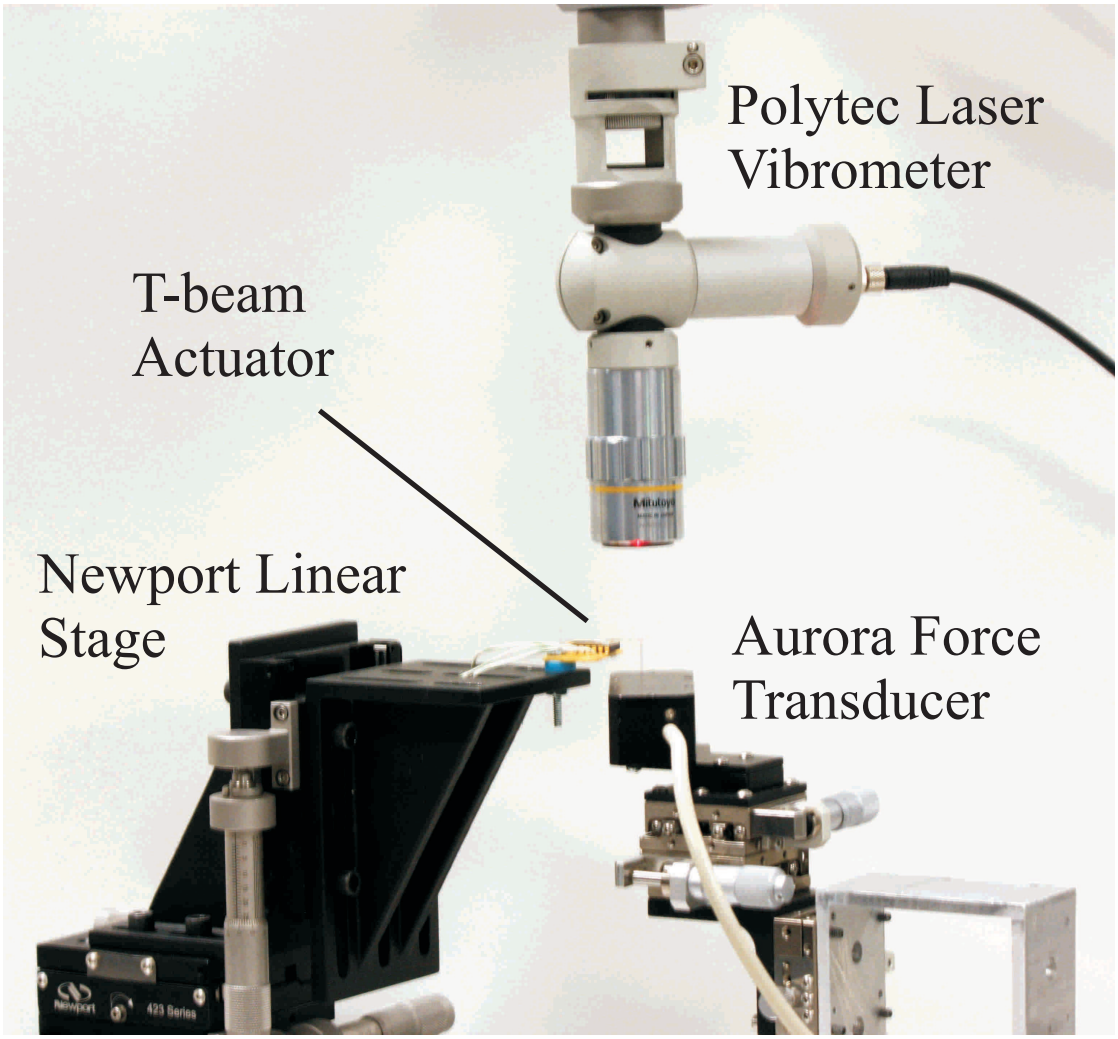

Figure A.1.3. Experimental testing setup of T-beam actuator

below the top of the flange. The potential energy is

$$U = U_b + U_p + \frac{1}{2}k_T w(0,t)^2 + \frac{1}{2}k_R w'(0,t)^2 \tag{A.12}$$

$$U_b = \int_{V_b} \frac{E}{2}(-zw'')^2 dV \tag{A.13}$$

$$U_p = \int_{V_p} H dV \tag{A.14}$$

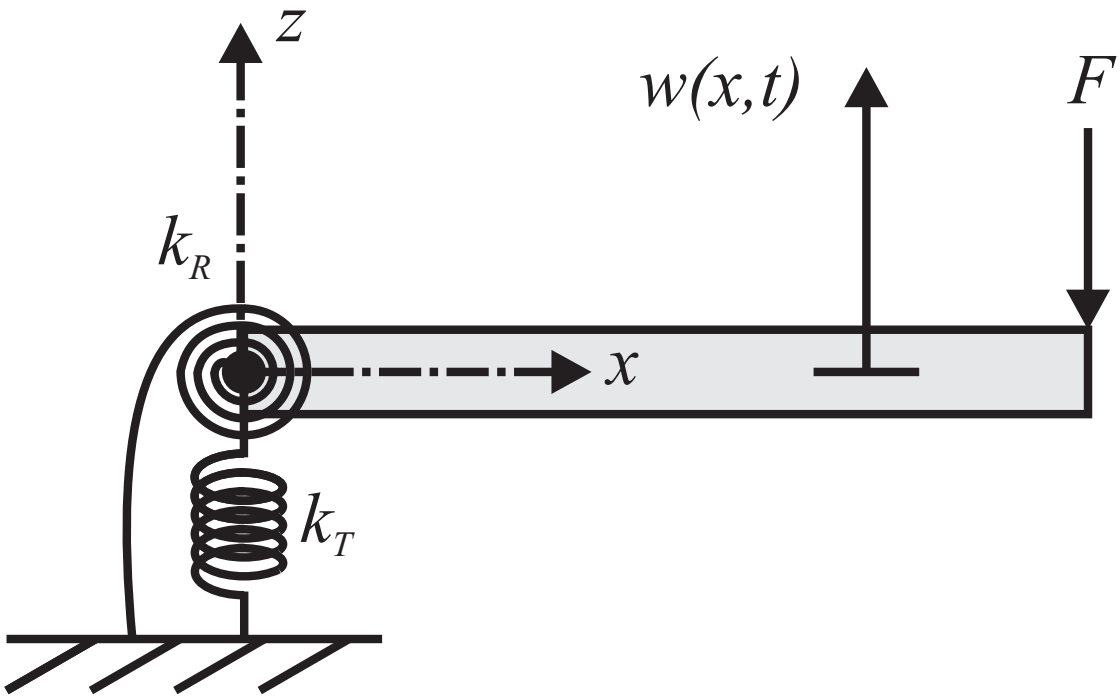

Figure A.1.4. Schematic diagram of T-beam with modified boundary condition

where $()' = \frac{d()}{dx}$, U_b and U_p are the potential energy of the passive and piezoelectrically active region, k_T is the translational spring constant, k_R is the rotational spring constant, and E is the Young's modulus of PZT-5H. The electric enthalpy, H, is given as

$$H = (a_2 z^2 + a_3)(w'')^2 + a_4 V w'' + a_5 V^2. \tag{A.15}$$

where the coefficients $a_i (i = 2, 3, 4, 5)$ are given in Table A.1.3. The virtual work done by the force generated at the tip is

$$\delta W = F \delta w(L, t). \tag{A.16}$$

Substitution of the potential energy into the principle of virtual work, $\int_0^{t_f}(\delta U + \delta W)dt = 0$, produces the field equations

$$w'''' = 0, \ \forall x \in (0, L), \tag{A.17}$$

boundary conditions

$$EI_{eff}w''(0,t) + K_V V - k_R w'(0,t) = 0 \tag{A.18}$$

$$EI_{eff}w'''(0,t) + k_T w'(0,t) = 0 \tag{A.19}$$

$$EI_{eff}w''(L,t) + K_V V = 0 \tag{A.20}$$

$$EI_{eff}w'''(L,t) - F = 0 \tag{A.21}$$

where the effective bending stiffness of the T-beam EI_{eff} and the coefficient K_V is given in Table A.1.3. The solution for Equation A.17 is

$$w(x) = c_3x^3 + c_2x^2 + c_1x + c_0. \tag{A.22}$$

The coefficients $c_i(i = 0, 1, 2, 3)$ are solved using the boundary conditions in Eqs. (**??**) - (**??**). The free displacement and blocking force at the tip of the beam are

$$w_f = \frac{K_V L^2 V}{2EI_{eff}} \tag{A.23}$$

$$F_b = \frac{3K_V L^2 V}{2L^3 + 6EI_{eff}(L^2/k_R + 1/k_T)} \tag{A.24}$$

The d_{31} coefficient given by the manufacturer in Table A.1.2 is measured at low electric fields. Nonlinear electromechanical effects begin to contribute significantly when soft PZT materials are actuated at fields greater than 0.005 $V/\mu m$[92]. The piezoelectric strain coefficient, d_{31} can be considered a function of electric field, temperature, and stress[93] and can increase 40% in response to high electric fields[94]. In this work, the focus is to develop useful models for T-beam actu-

ators over a certain operating regime. Figure A.1.5 shows the experimental and theoretical peak values of static displacement using a 40% larger d_{31} than the data from the manufacturer in Table A.1.2. Figure A.1.6 shows the experimental and theoretical peak value of the blocking force, where the parameters k_R and k_T were adjusted to simulate the deflection of the FR4 board thereby reducing the force predicted in the model.

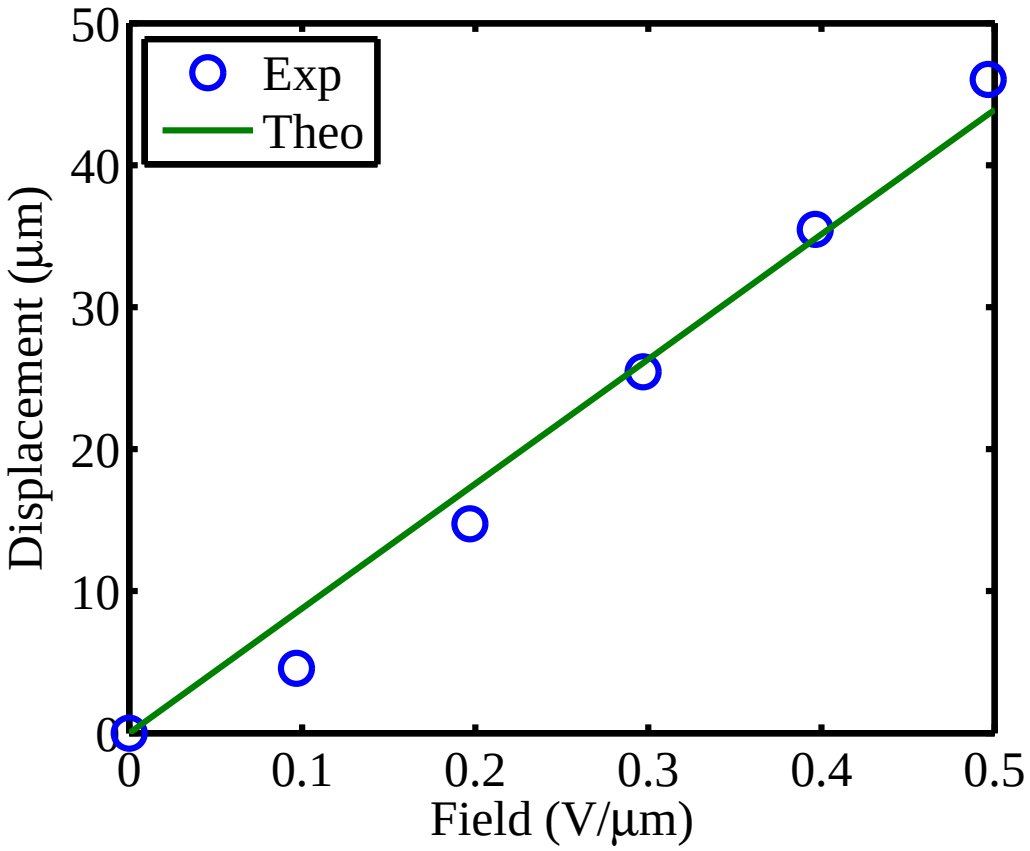

Figure A.1.5. Experimental (circle) and theoretical (solid) tip displacement versus electric field

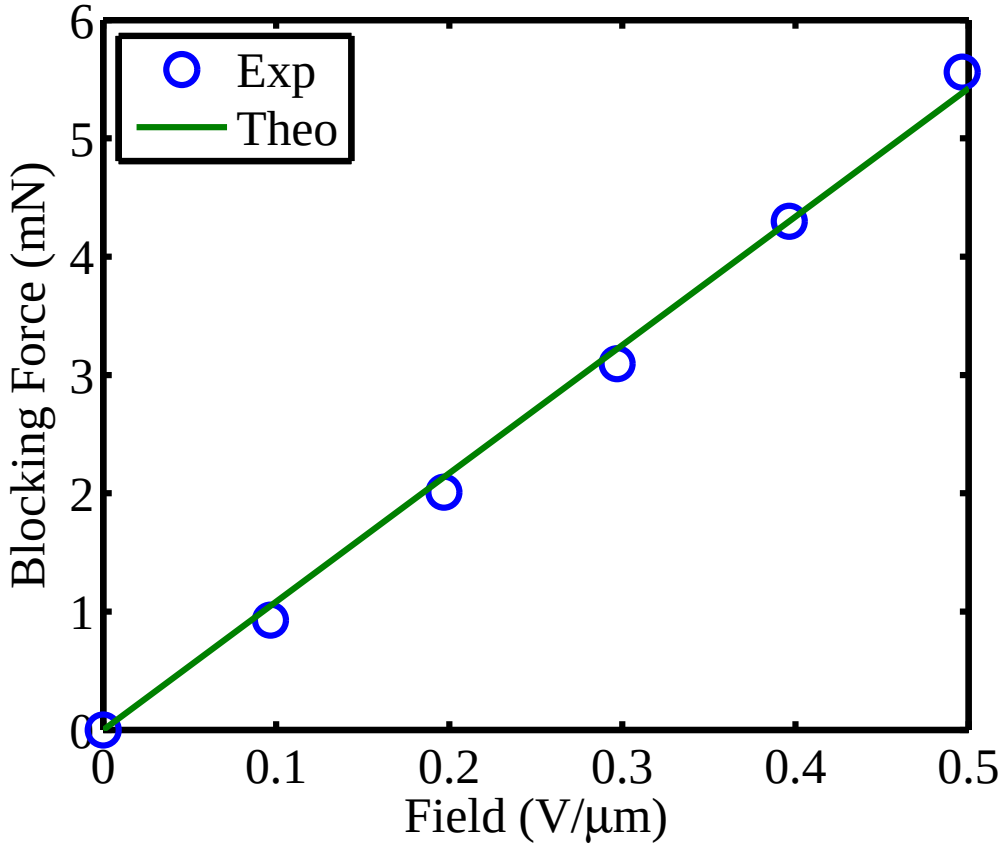

Figure A.1.6. Experimental (circle) and theoretical (solid) blocking force versus electric field

A.1.4.3 Dynamic Modeling

The kinetic energy of the T-beam, neglecting rotational inertia, is

$$T = \frac{1}{2}\int_0^L \rho A \dot{w}^2 dx. \tag{A.25}$$

where ρ is the density of PZT-5H, and $A = A_b + A_p$ is the total cross sectional area of the beam. Using the potential energy term derived in (Equation A.14), the virtual work (Equation A.16), and the kinetic energy (Equation A.25) into

Hamilton's principle $\int_0^{t_f}(\delta W + \delta T - \delta U)dt$ yields the equations of motions

$$EI_{eff}w'''' + \rho A\ddot{w} = 0 \tag{A.26}$$

with the same boundary conditions, Eqs. (A.19) - (A.21). The equations of motion can be modified to include strain-rate damping and viscous air damping by [95]

$$EI_{eff}w'''' + c_s\dot{w}'''' + c_a\dot{w} + \rho A\ddot{w} = 0 \tag{A.27}$$

where c_s is the strain-rate damping coefficient, c_a is the viscous air damping coefficient. Considering the small area of the T-beam, assume the air damping will have neglegible effect compared with the strain-rate damping ($c_a = 0$). Taking the Laplace transform of equation (**??**) with $c_a = 0$ yields

$$\rho As^2\tilde{w} + c_s s\tilde{w}'''' + EI_{eff}\tilde{w}'''' = 0. \tag{A.28}$$

Assume a solution

$$\tilde{w}(x,s) = C_1\cos(\beta x) + C_2\sin(\beta x) + C_3\cosh(\beta x) + C_4\sinh(\beta x) \tag{A.29}$$

where

$$\beta(s) = \left(-\frac{s^2\rho A}{c_s s + EI_{eff}}\right)^{1/4} \tag{A.30}$$

and $s = j\omega$. Solving for the coefficents $C_i(i = 0,1,2,3)$ using the boundary conditions (A.19-A.21) yields the solution for tip displacment in the frequency domain

$$\tilde{w}(L,s) = \frac{N(\beta)}{D(\beta)}V(s) \tag{A.31}$$

where

$$N(\beta) = K_V \left(\frac{\beta^3 EI_{eff}}{k_R k_T} (\cos(\beta L) - \cosh(\beta L)) \right. \tag{A.32}$$

$$+ \frac{1}{k_R} (\sinh(\beta L) - \sin(\beta L)) \tag{A.33}$$

$$+ \left(\frac{\beta^3 EI_{eff}}{k_R k_T} + \frac{1}{\beta EI_{eff}} \right) \sin(\beta L) \sinh(\beta L))) \tag{A.34}$$

$$+ \left(\frac{1}{k_R} + \frac{\beta^2}{k_T} \right) \cosh(\beta L) \sin(\beta L) \tag{A.35}$$

$$+ \left. \left(\frac{1}{k_R} - \frac{\beta^2}{k_T} \right) \cos(\beta L) \sinh(\beta L) \right) \tag{A.36}$$

$$D(\beta) = \beta(1 + \cos(\beta L) \cosh(\beta L)) \tag{A.37}$$

$$+ \frac{\beta^5 (EI_{eff})^2}{k_R k_T} (\cos(\beta L) \cosh(\beta L) - 1) \tag{A.38}$$

$$+ \left(\frac{\beta^2 EI_{eff}}{k_R} + \frac{\beta^4 EI_{eff}}{k_T} \right) \tag{A.39}$$

$$\times (\cosh(\beta L) \sin(\beta L) + \cos(\beta L) \sinh(\beta L)) \tag{A.40}$$

Figure A.1.7 shows the experimental and theoretical frequency response of the T-beam actuator. The damping coefficient c_s was adjusted to match the experimental data. During strong AC electric fields, soft piezoelectrics also exhibit softening due to elastic nonlinearity[92]. The Young's modulus was reduced by 10% from Table A.1.2 to simulate this effect.

A.1.4.4 Conclusion

This work presents static and dynamic testing and modeling of PZT-5H T-beam actuators. These models are useful tools in further studies involving NAV flapping wing mechanisms. The results include boundary condition modifications to simulate imperfect clamping. This could be useful because the mechanical grounding in a lightweight NAV airframe may not provide a perfect clamped boundary condition. Nonlinear effects on the electromechanical properties of soft PZT under

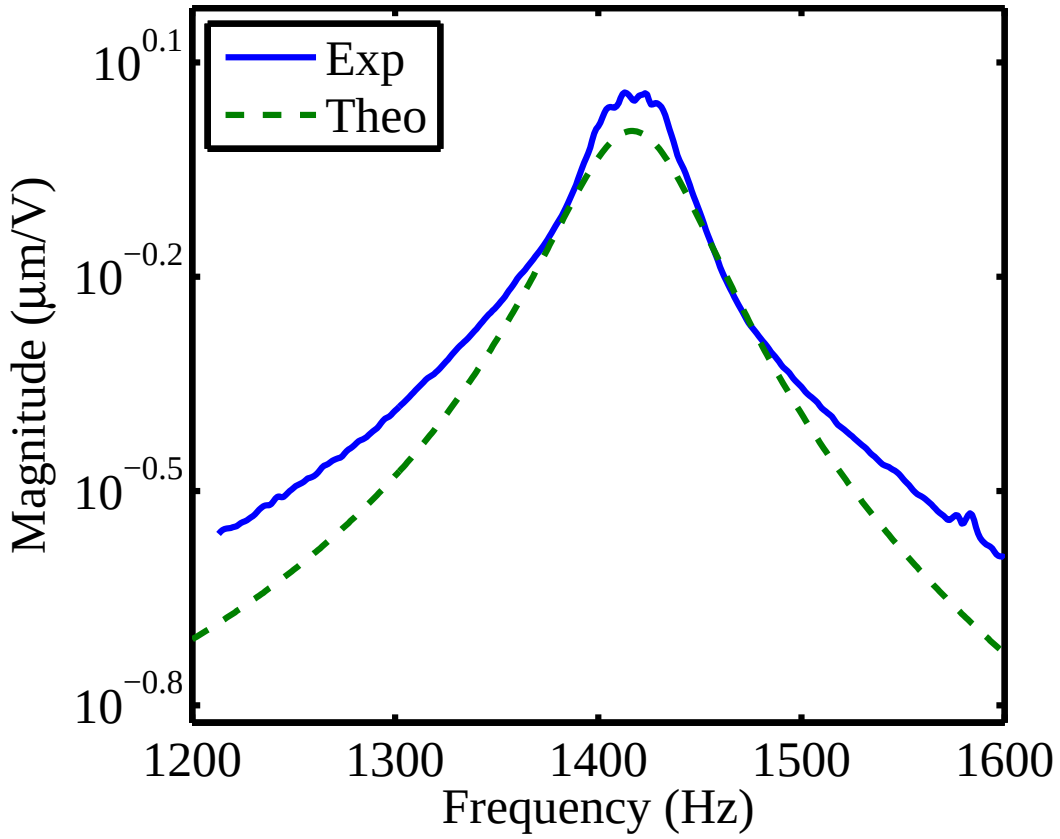

Figure A.1.7. Experimental (solids) and theoretical (dashed) displacement versus frequency in response to 0.01 $V/\mu m$ electric field

strong fields were considered, and piezoelectric coefficients and Young's modulus were modified based on experimental data. A frequency response solution has been derived including strain-rate damping. The accuracy of the models greatly depend on proper experimental data to fit key parameters, but is useful for future modeling efforts.

Appendix B

Design and Extra Results of the Lionfly

B.1 Single Degree of Freedom Design

B.1.1 Kinematics

The following section studies the effect of the mechanism parameters on static operation of the LionFly mechanism. The device designed to flap at a maximum of 90 *deg*. at resonance, which sets the flexure lengths, L_A, L_B, L_O for a given flexure thickness, t_f. The starting position of the actuator, x_{ref}, is chosen such that the starting flapping angle is 45 deg. The flexure lengths and mechanism parameters: link lengths, L_{AB}, L_{OA}, and vertical offset, $r4$, must satisfy Equation 4.1. In the first step in the design optimization it is reasonable to assume a certain actuator displacement, because flapping angle is based purely on kinematics. Later, we include the spring forces from the flexures. As the width of the actuator increases, the actuator bending stiffness and blocking force production increases and the two results should converge. First, understanding the effect of L_{AB}, L_{OA}, and vertical offset, $r4$, on flapping angle is made. For Figure B.1.1 and Figure B.1.2, assume

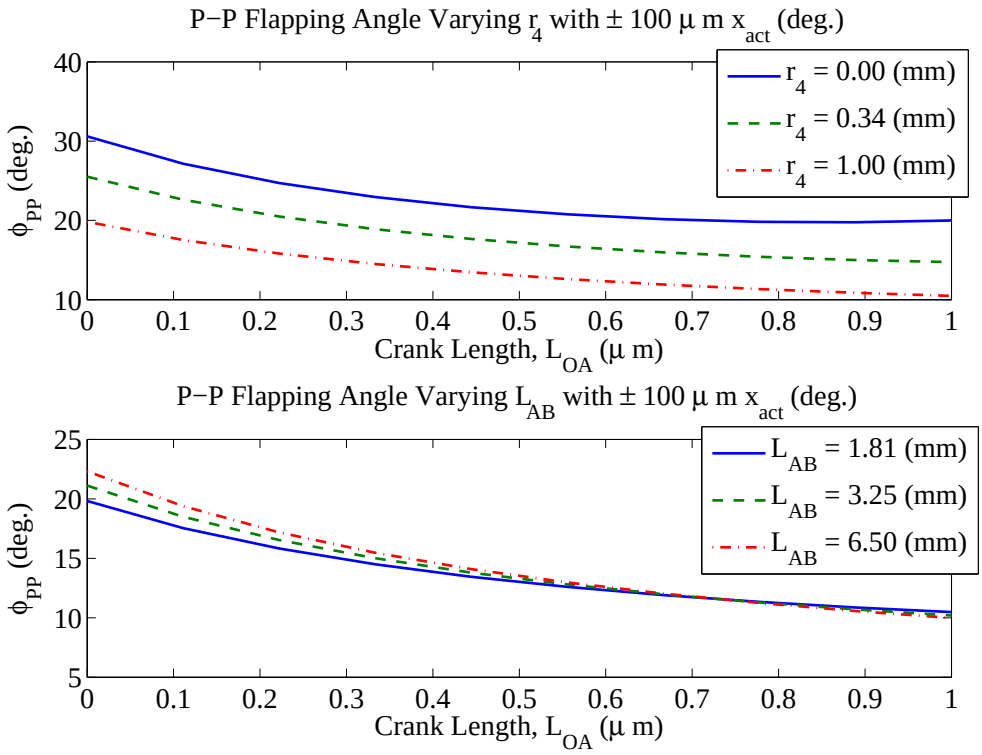

Figure B.1.1. Peak to peak flapping angle versus crank length. Top plot, $L_{AB} = 1.81\ mm$, bottom plot $r_4 = 1\ mm$.

+/- 100 μm displacement from the actuator (0.05% strain of a 15 mm bimorph or applied 150V).

Figure B.1.1 shows the peak to peak flapping angle as a function of crank length and varying vertical offset and coupler link length. In the first subplot using r_4, a coupler link value was chosen that leads to least amplification $L_{AB} = 1.81mm$, and the same idea for the coupler link plot, holding $r_4 = 1mm$. The coupler length doesn't greatly affect the flapping angle magnitude. Setting the crank length to zero (r_2 is nonzero because of the flexure lengths), will yield maximum amplification.

In Figure B.1.2 we see that although the peak-peak flapping angle increases when r_4 goes to zero, it becomes more nonlinear. Increasing r_4 shifts the dead

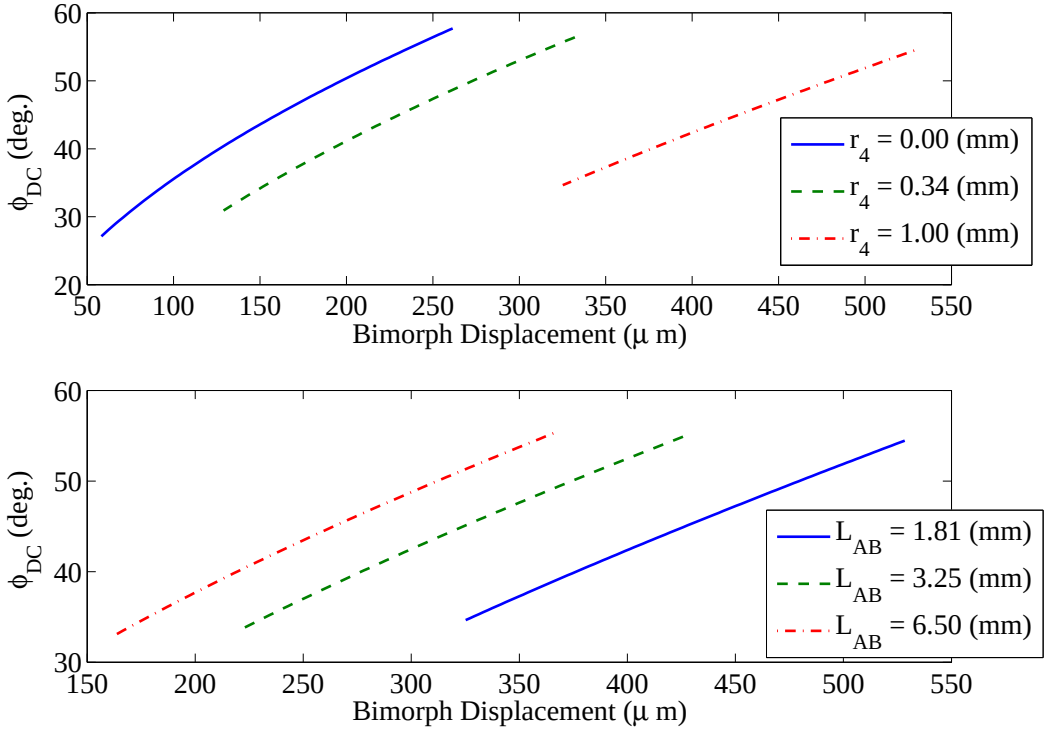

Figure B.1.2. Flapping response with prescribed bimorph displacement, centered on x_{ref} such that $\phi = 45\ deg.$. Notice how the $r_4 = 0$ response begins to curve

position of the mechanism, when the crank length and coupler length become colinear, to a negative angle. So, a nearly linear response is achieved when we make r_4 large (1 mm is easy to fabricate using a thick glass slide). The responses are centered around 45 *deg.*, and have different x_{ref} positions. The coupler to crank length ratio, L_{AB}/L_{OA} determines the deviation from a perfect sinusoid the output will have. The higher the ratio, the closer to a pure sinusoid the output will be.

B.1.2 Static Response

Now we solve the equilibrium equation for the actual bimorph position, using Equation 4.9. The coupler length and vertical offset were fixed at 2 *mm*, and

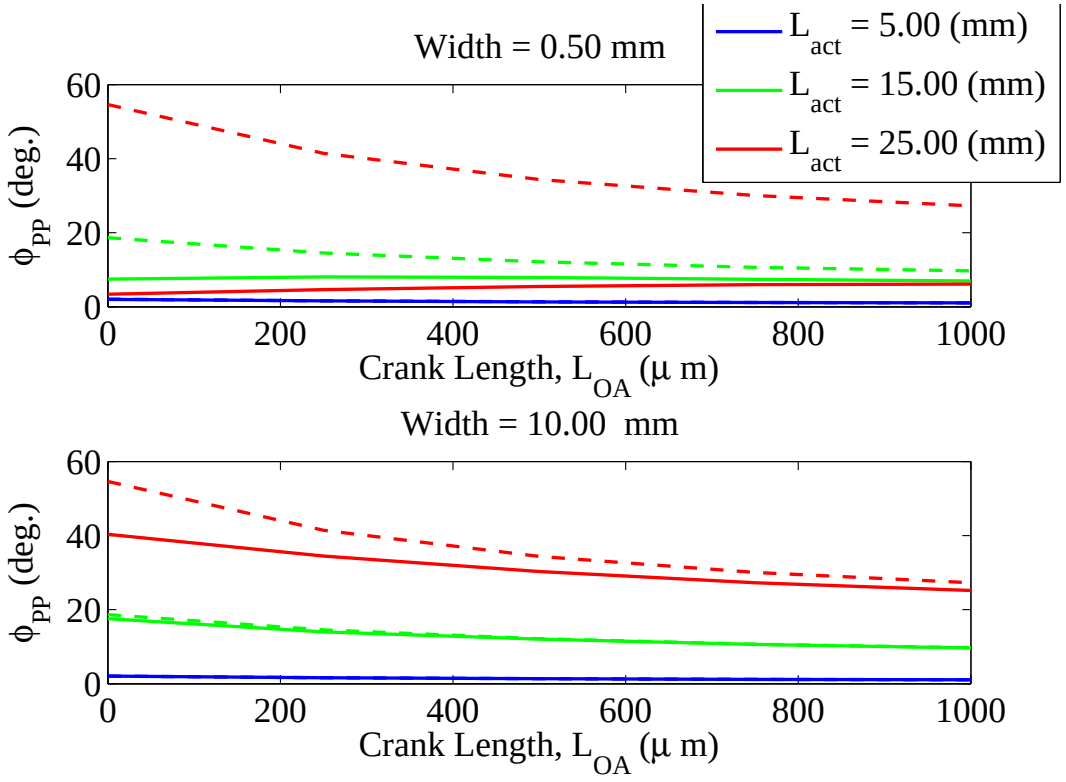

Figure B.1.3. ϕ_{PP} versus crank length, L_{OA} with applied voltage of $\pm 150\ V$, $\phi_0 = 45°$: (solid) calculated ϕ by solved bimorph displacement, (dashed) ϕ calculated by bimorph free displacement

$1mm$ respectively. The constraints for the length of the crank link, L_{OA}, actuator, L_{act}, and width of the actuator, w_{act} are

$$0 \leq L_{OA} \leq 1\ mm \tag{B.1}$$

$$5 \leq L_{act} \leq 25\ mm \tag{B.2}$$

$$0.5 \leq w_{act} \leq 10\ mm. \tag{B.3}$$

The flexure thickness is $t_f = 25\mu m$, widths $w_O = 6\ mm$, $w_A = w_B = 3\ mm$, and $E_f = 2.8\ GPa$. With and applied voltage $\pm 150\ V$, Equation 4.9 is solved for x, and Equation 4.2 is used to find $\phi(x)$.

The results show the effect of the flexure stiffness in reducing peak to peak flap-

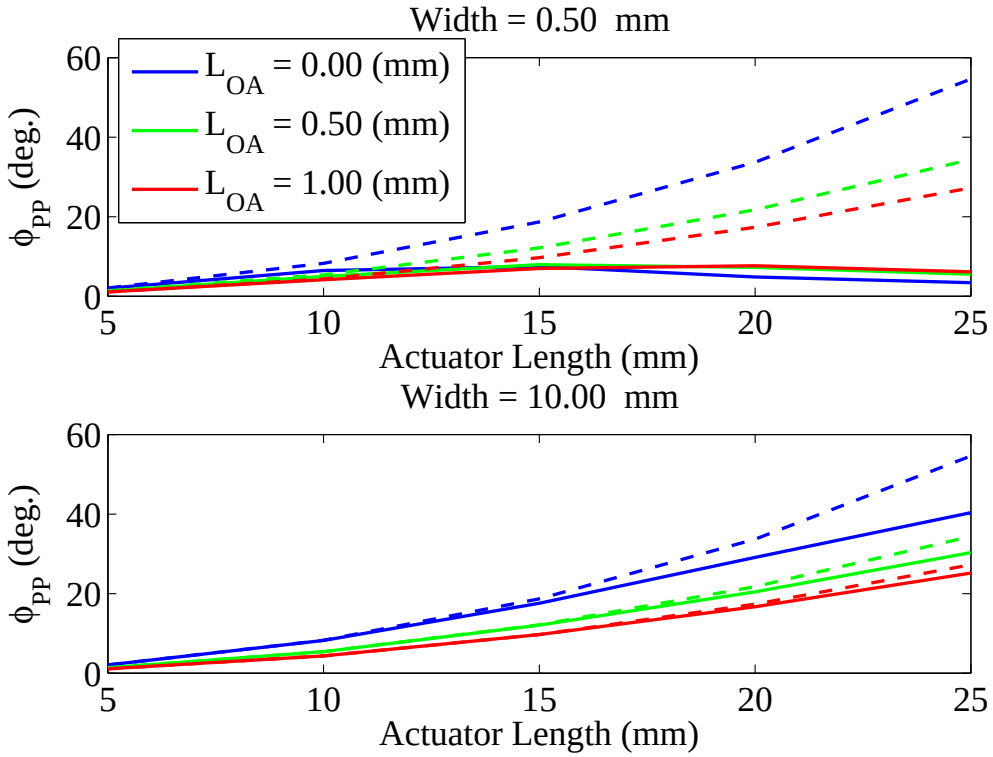

Figure B.1.4. ϕ_{PP} versus actuator length, L_{OA} with applied voltage of $\pm 150\ V$, $\phi_0 = 45°$: (solid) calculated ϕ by solved bimorph displacement, (dashed) ϕ calculated by bimorph free displacement

ping angles for most actuator geometry and crank lengths. The results show that for any given crank length, the wider actuators will approach the free displacement values as expected. For narrow actuators, smaller crank lengths (increased kinematic amplification) do not buy larger flapping angles. For a given width, there is a critical length after which the flapping angle decreases, as shown in Figure B.1.4. With maximum width, maximum length, and shortest crank length the largest flapping angles are achieved, however, even then the free displacement values are not reached (for $t_f = 25\ \mu m$).

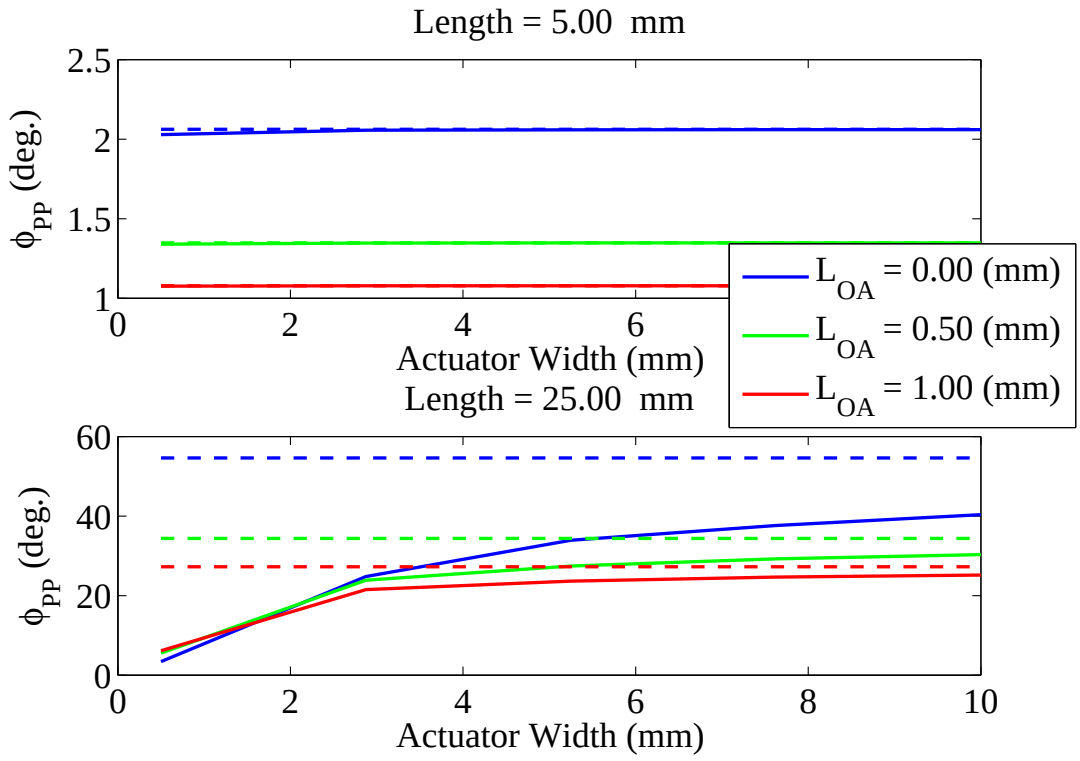

Figure B.1.5. ϕ_{PP} versus actuator width, L_{OA} with applied voltage of $\pm 150\ V$, $\phi_0 = 45°$: (solid) calculated ϕ by solved bimorph displacement, (dashed) ϕ calculated by bimorph free displacement

B.1.3 Amplitude Dependent Linear Aerodynamic Drag Force

The aerodynamic drag force on a single degree of freedom flapping wing mechanism is a quadratic nonlinear damping term dependent on the flapping velocity. Developing a linear approximation of this term will allow design of flapping wing mechanisms based on resonance operation and include amplitude dependent damping. The device has maximum flapping amplitude and angular velocity at resonance, however it is difficult to estimate what the magnitude is without adequate experimental results to tune damping coefficients. Following the approach of Davis [96], we can approximate a linear damping coefficient using the formula for the aerodynamic drag force on the wing, as a function of the forcing, linear

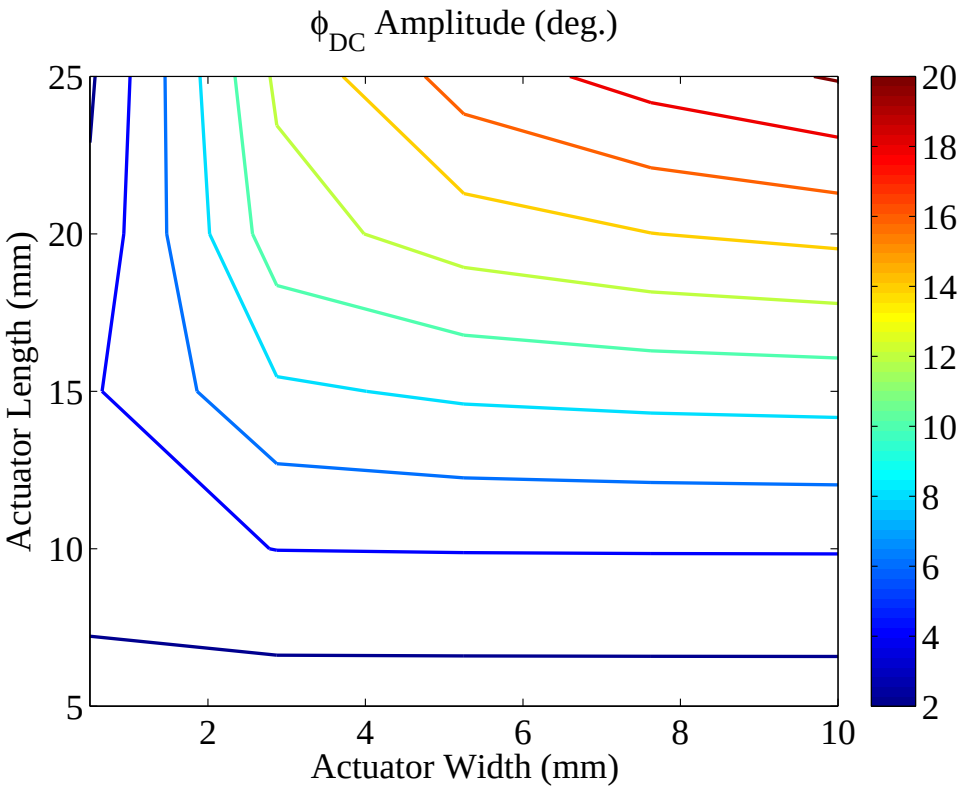

Figure B.1.6. Contour plot of ϕ_{DC} amplitude over actuator length and width.

damping and natural frequency. If we focus on the single degree of freedom system with flapping, ϕ, and temporarily neglect ψ, the kinetic energy is simply

$$T = \frac{1}{2}(J_{yy} + J_s + J_{am})\dot{\phi}^2 = \frac{1}{2}J_\phi\dot{\phi}^2 \tag{B.4}$$

where, J_{yy} is the inertia about the flapping axis, J_s is the inertia of the wing spar about the flapping axis, and

$$J_{am} = \int_0^R \frac{\pi}{4}c(r)^2 r'^2 dr. \tag{B.5}$$

The virtual work is

$$\delta W = G_{act}V\delta x + F_N\delta r_{CP_x} + c_\phi\dot{\phi}\delta\phi, \tag{B.6}$$

where c_ϕ is the linear viscous damping in vacuum, and using Lagrange's equations with ϕ as the generalized coordinate, we can write the equations of motion as

$$\ddot{\phi} + 2\mu_L\dot{\phi} + 2\mu_Q|\dot{\phi}|\dot{\phi} + \omega_n^2 = F_0(V) \tag{B.7}$$

where

$$\mu_L = \frac{c_\phi}{2J_\phi} = \zeta_L\omega_n \tag{B.8}$$

$$\mu_Q = \frac{r_{CP_x}\rho_{air}C_N(\alpha)\int_0^R c(r)r'^2dr}{2(J_{yy}+J_s)} \tag{B.9}$$

$$\omega_n = \sqrt{\frac{K}{J_\phi}} \tag{B.10}$$

$$F_0(V) = \frac{G_{act}V}{aJ_\phi} \tag{B.11}$$

$$K = \frac{1}{a^2}\left(k_{act} + \frac{\partial}{\partial x}f_s(x)\bigg|_{x=x_0}\right) \tag{B.12}$$

$$a = \frac{\partial\phi(x)}{\partial x}\bigg|_{x=x_0} \tag{B.13}$$

$$\tag{B.14}$$

From the results in [96], if the forcing function F_0 is sinusoidal at the resonant frequency ω_n, we can arrive at an estimate for the amplitude at resonance

$$a_p(V) = \frac{-3\mu_L\pi + \sqrt{(3\mu_L\pi)^2 + 48\mu_Q F_0(V)\pi}}{16\mu_Q w_n} \tag{B.15}$$

from which we can calculate an voltage dependent linear damping coefficient,

$$\zeta_Q(V) = \frac{8\mu_Q a_p(V)}{3\pi} \tag{B.16}$$

such that the equations of motion can be rewritten as

$$\ddot{\phi} + 2(\zeta_L + \zeta_Q(V))\dot{\phi} + \omega_n^2 = F_0(V) \tag{B.17}$$

To validate this approach, LF07 was tested using 125 VDC and multiple voltage amplitudes (25 VAC, 50 VAC, and 75 VAC) in air and in vacuum. **??** shows the flapping frequency response taken using high definition photographic measurement and image processing. The results show consistent prediction of resonant amplitude as voltage levels and flapping amplitudes are increased, validating the approach to estimate amplitude at resonance. This can now be used to estimate flapping velocity at resonance as a function of wing shape, resonant frequency, and forcing.

B.1.4 Rotational Hinge Stiffness

To achieve lift, we must have rotation in proper phase with flapping. This requires properly designed flexure hinges that allow passive rotation in response to aerodynamic forces acting upon the wing. To predict this force, the steady state angular velocity of the wing must be found. Using the results of last section, assuming a sinusoidal response, the angular velocity can be written as

$$\dot{\phi} = \omega_n a_p. \tag{B.18}$$

If the wing is extremely light, the force balance of the system in Fig. **??** is

$$r_{CP_y} F_N - k_\psi \psi = 0 \tag{B.19}$$

Substituting Eq. **??** and **??** into **??**, we can rearrange terms to solve for the hinge stiffness for a desired ψ

$$k_\psi = \frac{r_{CP_y} F_N}{\psi}. \tag{B.20}$$

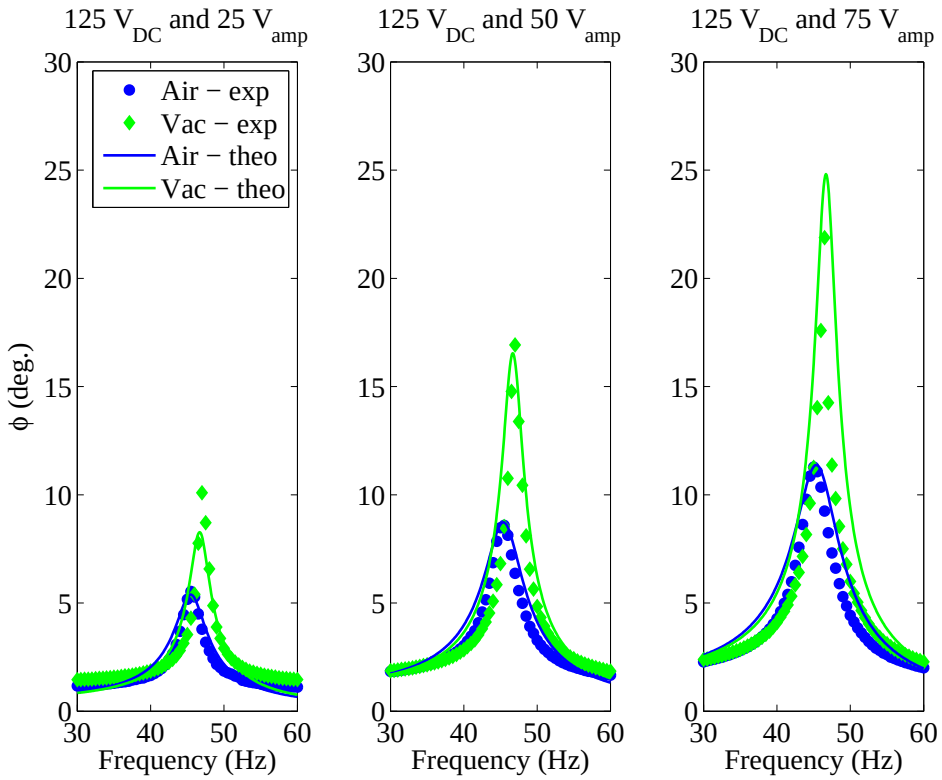

Figure B.1.7. Photographed, image processed and theoretical flapping, $\phi(t)$ versus frequency at (125 VDC/ 25 VAC) (left), (125 VDC/ 75 VAC) (middle), and (125 VDC/ 75 VAC) (right): Experimental $\phi(t)$ in air(blue circles) and vacuum (green diamonds), and theoretical $\phi(t)$ in air (blue solid) and vacuum (green solid).

The length of the rotational flexure hinge is determined by the maximum bending angle equation ref TBD. Since the thickness is limited by fabrication constraints, we control the stiffness of the hinge using the width. To achieve the desired k_ψ, the flexure width must be

$$w_{flex} = \frac{12 k_\psi L_{flex}}{\gamma K_\Theta E_{flex} t_{flex}^3} \tag{B.21}$$

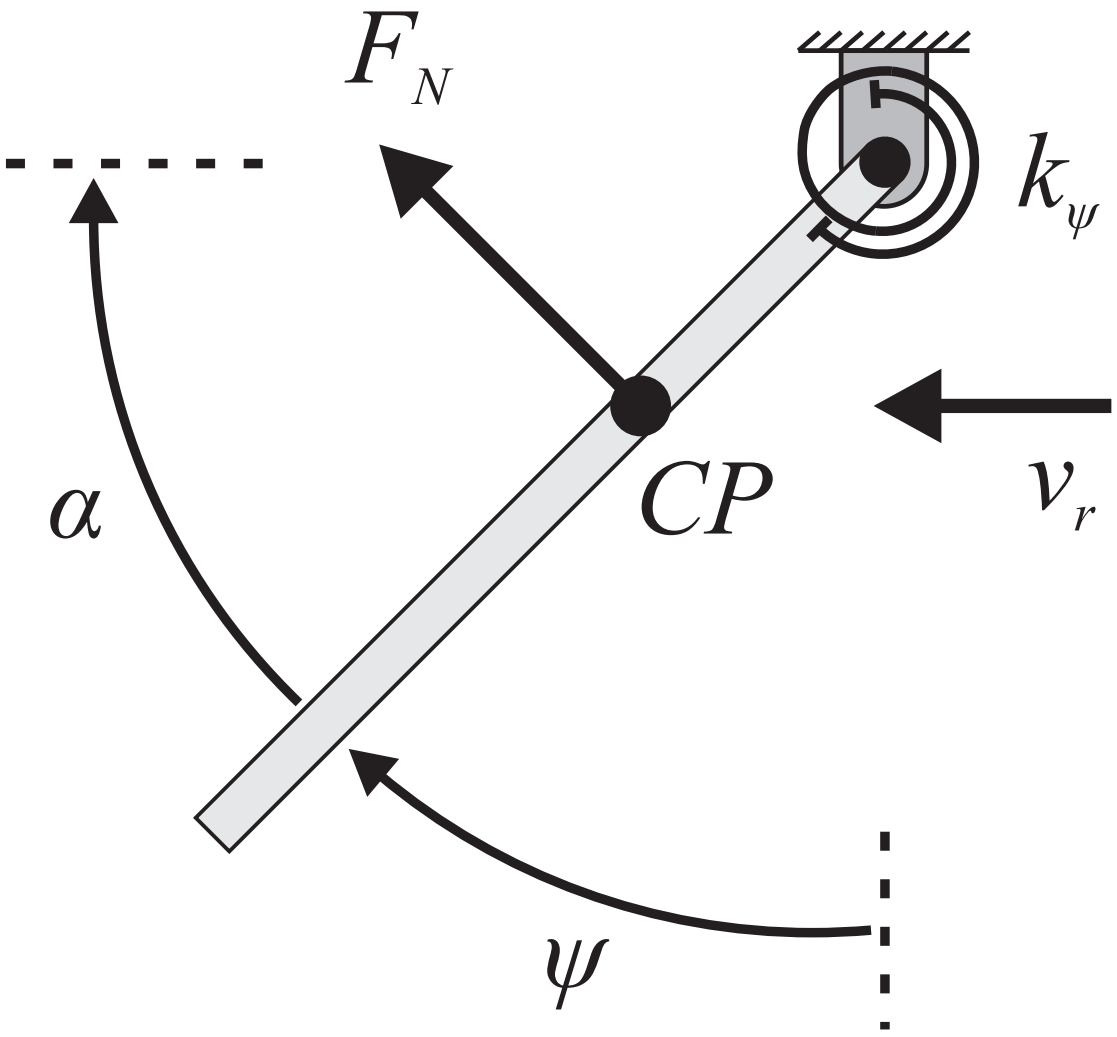

Figure B.1.8. Schematic of wing hinge, aerofoil, and aerodynamic drag force

B.2 Additional LionFly Data

New LionFly designs were fabricated to minimize flexure width according to Equation B.21, and with an extra photolithography step to define a intermediate flexure thickness level for vein definition. Yield of devices during fabrication drastically decreases when attempting to create flexure thickness below 20 μm. Additionally, successfully fabricated devices were extremely fragile and had very short life cycles, preventing sufficient testing. Even at these reduced thicknesses, testing

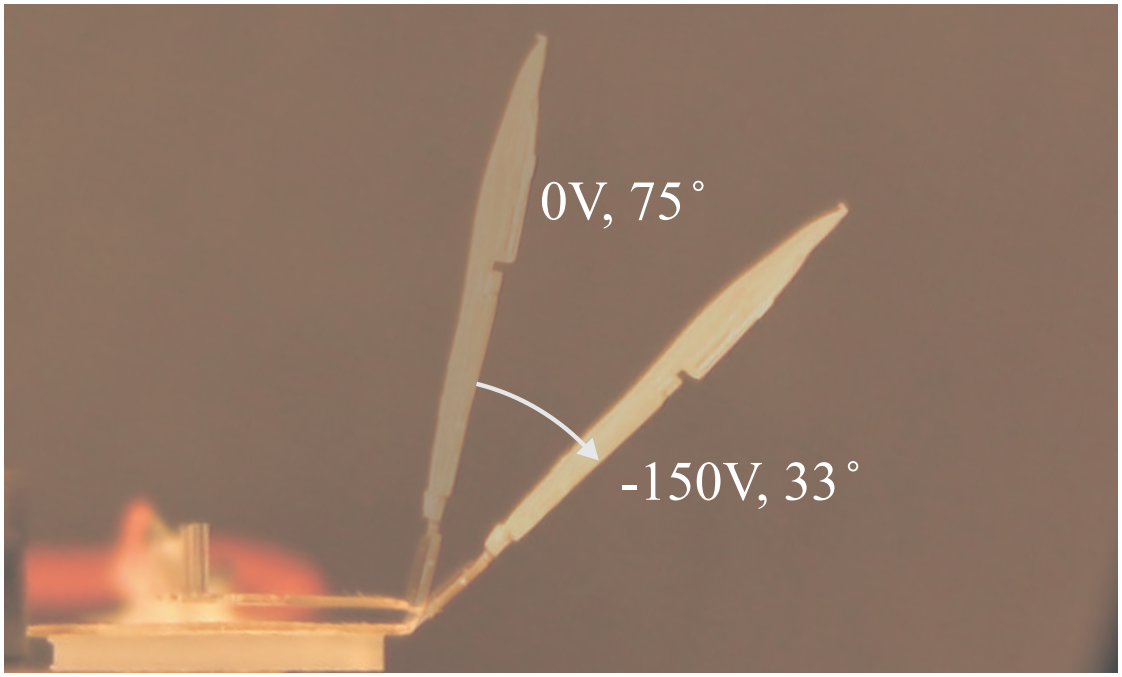

Figure B.2.1. Combined photograph of Tipulidae 1 at rest and actuated at -150 VDC. Thin flexure hinges, a 75 $deg.$ initial angle, and 25 mm long bimorph contributed to an increase in static performce with 33 $deg.$ flapping for -150 V.

showed nearly in phase flapping and rotation, showing that the "'light wing"' assumption is invalid. Figures B.2.1 and B.2.2 show the static and dynamic response of the LionFly modeled after a Cranefly, *Tipulidae*, an insect of the order *Diptera*. Figure B.2.3 shows the static response of the LionFly modeled after a Hoverfly, *Eristalis*, also of the order *Diptera*. This device shows the greatest static performance of any LionFly to date. Finally, a scaled down version of LF1203 with 10 mm span was fabricated and tested for lift. The device shows a force transducer measured 110 μN, which corrected for leverage is approximately 60 μN, showing slightly less lift than the LF 1203.

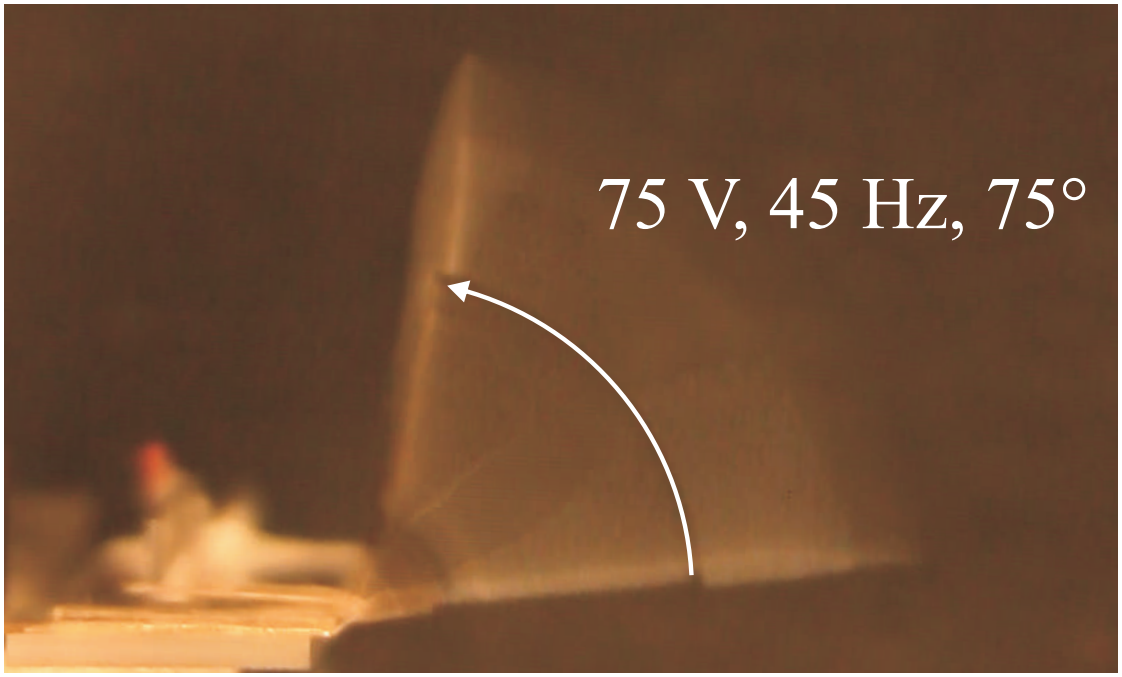

Figure B.2.2. Photograph of flapping at 75 V and 45 Hz for Tipulidae 1. Large amplitude flapping at 75 $deg.$ demonstrates the effectiveness in flapping mechanism performance. Improvements can be made to extend the cycle life of these devices, however.

B.3 Review of SU-8 Material Properties

SUEX is a relatively new material and little literature exists that report material property testing as a function of processing conditions. SU-8 negative photoresist shares many similar characteristics to SUEX and has numerous articles that report the influence of processing conditions on material properties. The key material properties we are interested in are Young's modulus and yield stress. Table B.3.1 shows a list of SU-8 material properties, and associated fabrication process notes.

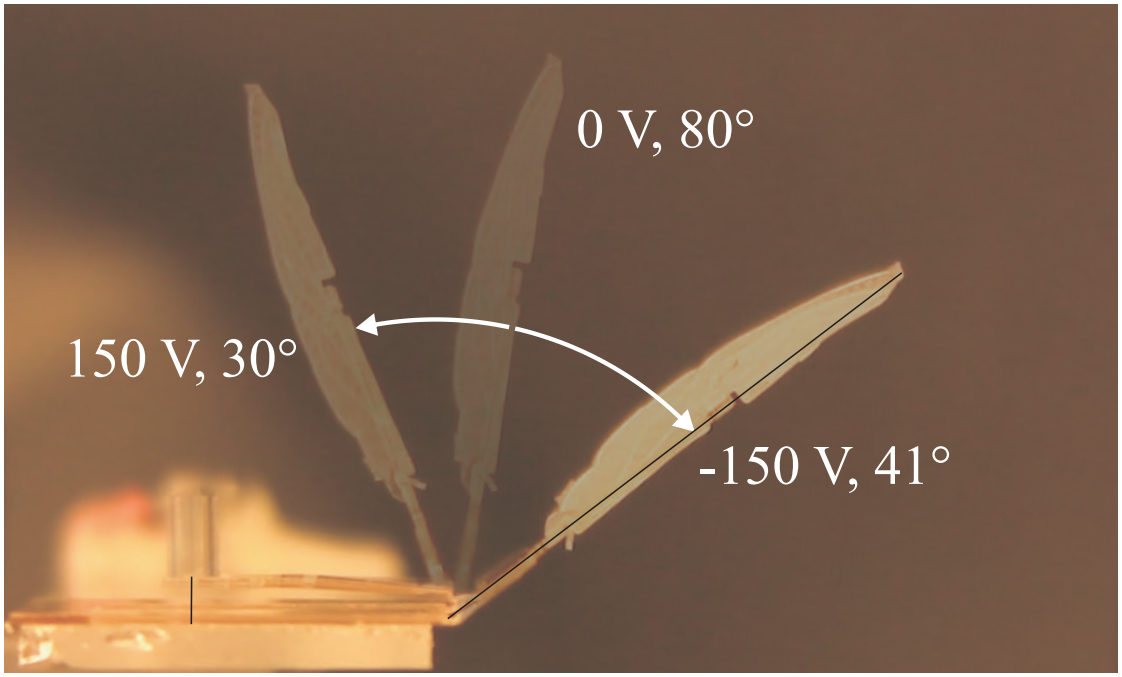

Figure B.2.3. Combined photograph of Eristalis 1 at rest and actuated at -150 to 150 VDC. Thin flexure hinges, a 80 $deg.$ initial angle, and 25 mm long bimorph contributed to an increase in static performce with 71 $deg.$ total flapping angle, the best recorded for any LionFly.

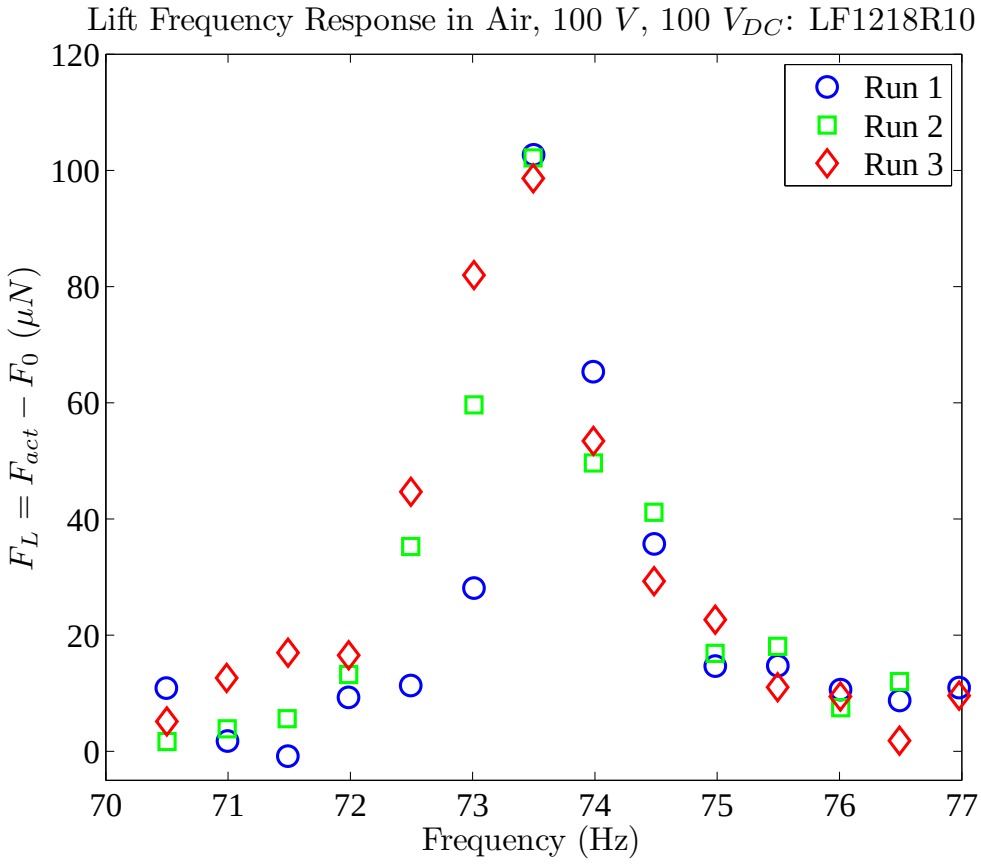

Figure B.2.4. Average value lift versus frequency for LF1218R10 with 10 mm wingspan actuated at (100 VDC/ 100VAC) over three independent runs.

Table B.3.1. SU-8 and SUEX Material Properties

Material Blend	E (GPa)	σ_y (MPa)	Notes
SU-8 2000[a] [97]	2.0	60.0	HB at 150°C/30 min
SU-8 3000[a] [97]	2.0	73.0	HB at 150°C/30 min
XP SU-8 25[a] [98]	0.7	16.1	No PEB or HB, Instron 5564, immediately
XP SU-8 25[a] [98]	2.7	42.1	95°C/30 min PEB, 200°C/30 min HB, Instron 5564 , 24h
EPON® SU-8[a] [10]	2.0	/	95°C/2 min PEB, no HB, TA Q800 DMA
EPON® SU-8[b] [99]	1.4-3.2	/	Custom profilometer stylus method, MFT2000
EPON® SU-8 [100]	1.5-3.1	49.0-77.0	Speckle Interferometery with Electron Microscope
EPON® SU-8[c] [101]	4.0	/	Screw Tensile Testing UTS-100
SU-8 [102]	5.3-6.2	/	No PEB, no HB, nanomechanical triboindenter
SU-8 50 [103]	3.5-7.5	/	70°C/ 45 min PEB, no HB
SUEX™ TDFS[d] [68]	2.8-3.9	86.0	ASTM D3379-75, Dage tensile pull

[a] Shell Chemical, [b] MicroChem Corp., [c] Resolution Europe BV, [d] DJ DevCorp

Bibliography

[1] "Boston Piezo Optics, Inc." Accessed 12-6-2010.

[2] Hylton, T. (2008) "DARPA Nano Air Vehicle Program Fact Sheet," Arlington, VA.

[3] Wood, R. J., B. Finio, M. Karpelson, K. Ma, N. Perez-Arancibia, P. Sreetharan, H. Tanaka, and J. Whitney (2011) "Progress on "pico" air vehicles," in *International Symposium on Robotics Research*.

[4] Proceedings of the 2005 IEEE/ASME International Conference on Advanced Intelligent Mechatronics (2005) *A MAV That Flies Like An Airplane and Hovers Like a Helicopter*.

[5] AHS 61st Annual Forum (2005) *Design and Testing of a Rotary Wing MAV with an Active Structure for Stability and Control*, AHS International, Inc., Grapevine, TX.

[6] Madangopal, R., Z. A. Khan, and S. K. Agrawal (2005) "Biologically Inspired Design Of Small Flapping Wing Air Vehicles Using Four-Bar Mechanisms And Quasi-steady Aerodynamics," *J. Mech. Des.*, **127**(4), pp. 809–816.
URL `http://link.aip.org/link/?JMD/127/809/1`

[7] Kawamura, Y., S. Souda, S. Nishimoto, and C. P. Ellington (2008) "Clapping-wing Micro Air Vehicle of Insect Size," *Bio-mechanisms of Swimming and Flying*, pp. 319–330.

[8] Wood, R. (2008) "The First Takeoff of a Biologically Inspired At-Scale Robotic Insect," *Robotics, IEEE Transactions on*, **24**(2), pp. 341–347.

[9] Bradshaw, N. and D. Lentink (2008) "Aerodynamic and structural dynamic identification of a flapping wing micro air vehicle," in *American Institute of Aeronautics and Astronautics, 26th AIAA Applied Aerodynamics Conference*.

[10] Dargent, T., X. Q. Bao, S. Grondel, G. L. Brun, J. B. Paquet, C. Soyer, and E. Cattan (2009) "Micromachining of an SU-8 flapping-wing flying micro-electro-mechanical system," *Journal of Micromechanics and Microengineering*, **19**(8), p. 085028.

[11] Dickinson, M. H., F.-O. Lehmann, and S. P. Sane (1999) "Wing Rotation and the Aerodynamic Basis of Insect Flight," *Science*, **284**(5422), pp. 1954–1960.
URL http://www.sciencemag.org/cgi/content/abstract/284/5422/1954

[12] Ennos, A. (1989) "The kinematics and aerodynamics of the free flight of some diptera," *Journal of Experimental Biology*, **142**(1), pp. 49–.

[13] Karpelson, M., G.-Y. Wei, and R. Wood (2009) "Milligram-scale high-voltage power electronics for piezoelectric microrobots," in *Robotics and Automation, 2009. ICRA '09. IEEE International Conference on DOI - 10.1109/ROBOT.2009.5152319*, pp. 2217–2224.

[14] Karpelson, M., J. Whitney, G.-Y. Wei, and R. Wood (2010) "Energetics of flapping-wing robotic insects: towards autonomous hovering flight," in *Intelligent Robots and Systems (IROS), 2010 IEEE/RSJ International Conference on DOI - 10.1109/IROS.2010.5650269*, pp. 1630–1637.

[15] Steltz, E., M. Seeman, S. Avadhanula, and R. Fearing (2006) "Power Electronics Design Choice for Piezoelectric Microrobots," in *Intelligent Robots and Systems, 2006 IEEE/RSJ International Conference on*, pp. 1322–1328.

[16] Bruggerman, B. (2010) *Improving Flight Performance of DelFly II in Hover by Improving Wing Design and Driving Mechanism*, Master's thesis, Deflt University of Technology.

[17] Pornsin-Sirirak, T., Y. Tai, H. Nassef, and C. Ho (2001) "Titanium-alloy MEMS wing technology for a micro aerial vehicle application," *Sensors and Actuators A: Physical*, **89**(1-2), pp. 95–103.

[18] "Nano Hummingbird," Accessed February 29, 2012.
URL http://www.avinc.com/nano

[19] Wood, R., S. Avadhanula, R. Sahai, E. Steltz, and R. S. Fearing (2007) "Microrobot Design Using Fiber Reinforced Composites," *Journal of Mechanical Design*, **130**, pp. 052304–2.

[20] Bronson, J., J. Pulskamp, R. Polcawich, C. Kroninger, and E. Wetzel (2009) "PZT MEMS Actuated Flapping Wings for Insect-Inspired Robotics," in *IEEE 22nd International Conference on Micro Electro Mechanical Systems, 2009*, pp. 1047–1050.

[21] Bao, X., T. Dargent, S. Grondel, J. Paquet, and E. Cattan (2011) "Improved micromachining of all SU-8 3D structures for a biologically-inspired flying robot," *Microelectronic Engineering*, **88**, pp. 2218–2224.

[22] Lentink, D., S. R. Jongerius, and N. L. Bradshaw (2009) *The Scalable Design of Flapping Micro-Air Vehicles Inspired by Insect Flight*, Springer-Verlag Berlin Heidelberg.
URL `http://dx.doi.org/10.1007/978-3-540-89393-6-14`

[23] (1998) *Update on Flapping Wing Micro Air Vehicle Research Ongoing work to Develop a Flapping WIng, Crawling "Entomopter"*.

[24] Bunget, G. and S. Seelecke (2008) "BATMAV: a biologically inspired micro air vehicle for flapping flight: kinematic modeling," in *Proc. SPIE*, 1, SPIE, San Diego, California, USA, p. 6928.
URL `http://link.aip.org/link/?PSI/6928/69282F/1`

[25] ——— (2010) "BATMAV: a 2-DOF bio-inspired flapping flight platform," in *Proc. SPIE*, 1, SPIE, San Diego, CA, USA, p. 7643.
URL `http://link.aip.org/link/?PSI/7643/76433B/1`

[26] Lentink, D., N. Bradshaw, and S. Jongerius (2007) "Novel micro aircraft inspired by insect flight," *Comparative Biochemistry and Physiology - Part A: Molecular & Integrative Physiology*, **146**(4, Supplement 1), pp. S133–S134.

[27] Park, H. C., M. Syaifuddin, N. S. Goo, D. Byun, and K. J. Yoon (2006) "An Insect-Mimicking Flapping System Actuated by A Piezoceramic Actuator," in *Robotics and Biomimetics, 2006. ROBIO '06. IEEE International Conference on DOI - 10.1109/ROBIO.2006.340234*, pp. 451–456.

[28] Zdunich, P., D. Bilyk, M. MacMaster, D. Loewen, J. Delaurier, R. Kornbluh, T. Low, S. Stanford, and D. Holeman (2007) "Development and Testing of the Mentor Flapping-Wing Micro Air Vehicle," *Journal of Aircraft*, **44**, pp. 1701–1711.

[29] Steltz, E., S. Avadhanula, and R. Fearing (2007) "High lift force with 275 Hz wing beat in MFI," in *Intelligent Robots and Systems, 2007. IROS 2007. IEEE/RSJ International Conference on*, pp. 3987–3992.

[30] Cox, A., D. Monopoli, D. Cveticanin, M. Goldfarb, and E. Garcia (2002) "The Development of Elastodynamic Components for Piezoelectrically Actuated Flapping Micro-Air Vehicles," *Journal of Intelligent Material Systems and Structures*, **13**(9), pp. 611–615.

[31] Nguyen, Q.-V., H. C. Park, N. S. Goo, and D. Byun (2009) "Aerodynamic Force Generation of an Insect-Inspired Flapper Actuated By a Compressed Unimorph Actuator," *Chinese Science Bulletin*, **54**, pp. 2871–2879.

[32] Sane, S. P. (2003) "The aerodynamics of insect flight," *J Exp Biol*, **206**(23), pp. 4191–4208.
URL `http://jeb.biologists.org/cgi/content/abstract/206/23/4191`

[33] Whitney, J. and R. Wood (2010) "Aeromechanics of Passive Rotation in Flapping Flight," *Journal of Fluid Mechanics*, **660**, pp. 197–220.

[34] Wang, Z. J. (2004) "DISSECTING INSECT FLIGHT," *Annu. Rev. Fluid Mech.*, **37**(1), pp. 183–210.
URL `http://dx.doi.org/10.1146/annurev.fluid.36.050802.121940`

[35] Ishihara, D., T. Horie, and M. Denda (2009) "A Two-Dimensional Computatonal Study on the Fluid-Structure Interaction Cause of Wing Pitch Changes in Dipteran Flapping Flight," *Journal of Experimental Biology*, **212**, pp. 1–10.

[36] Bao, L. and Y. Yu (2009) "Preliminary Modeling of the Fluid-Structure Interaction on a Deformable Insect Wing in Flapping," *New Trends in Fluid Mechanics Research*, pp. 638–641.

[37] Khan, Z. and S. Agrawal (2007) "Design and optimization of a biologically inspired flapping mechanism for flapping wing micro air vehicles," in *Robotics and Automation, 2007 IEEE International Conference on*, IEEE, pp. 373–378.

[38] Finio, B., N. Prez-Arancibia, and R. Wood (2011) "System identification and linear time-invariant modeling of an insect-sized flapping-wing micro air vehicle," in *Intelligent Robots and Systems (IROS), 2011 IEEE/RSJ International Conference on*, IEEE, pp. 1107–1114.

[39] Dudley, R. (2002) *The biomechanics of insect flight: form, function, evolution*, Princeton Univ Pr.

[40] Fearing, R., K. Chiang, M. Dickinson, D. Pick, M. Sitti, and J. Yan (2000) "Wing transmission for a micromechanical flying insect," in *Robotics and Automation, 2000. Proceedings. ICRA'00. IEEE International Conference on*, vol. 2, IEEE, pp. 1509–1516.

[41] Chan, H.-Y., J. H. M. Lam, and W. Li (2004) "A Biomimetic Flying Silicon Microchip: Feasibility Study," in *Robotics and Biomimetics, 2004. ROBIO 2004. IEEE International Conference on*, pp. 447–451.

[42] Karpelson, M., G.-Y. Wei, and R. Wood (2008) "A review of actuation and power electronics options for flapping-wing robotic insects," in *Robotics and Automation, 2008. ICRA 2008. IEEE International Conference on*, pp. 779–786.

[43] Tang, W., T. Nguyen, and R. Howe (1989) "Laterally driven polysilicon resonant microstructures," *Sensors and actuators*, **20**(1-2), pp. 25–32.

[44] Wood, R., E. Steltz, and R. Fearing (2005) "Optimal energy density piezoelectric bending actuators," *Sensors and Actuators A: Physical*, **119**(2), pp. 476–488.
URL http://www.sciencedirect.com/science/article/B6THG-4F05G63-2/2/479c823e48f9592c889532f2ddfc8182

[45] Kornbluh, R., R. Pelrine, Q. Pei, R. Heydt, S. Stanford, S. Oh, and J. Eckerle (2002) "Electroelastomers: Applications of dielectric elastomer transducers for actuation, generation, and smart structures," in *Proceedings of SPIE*, vol. 4698, pp. 254–.

[46] Srinivasan, P. and S. Spearing (2008) "Optimal Materials Selection for Bimaterial Piezoelectric Microactuators," *Microelectromechanical Systems, Journal of*, **17**(2), pp. 462–472.

[47] Park, S.-E. and T. Shrout (1997) "Characteristics of relaxor-based piezoelectric single crystals for ultrasonic transducers," *Ultrasonics, Ferroelectrics and Frequency Control, IEEE Transactions on*, **44**(5), pp. 1140–1147.

[48] Brown, L. (2000) "Design considerations for piezoelectric polymer ultrasound transducers," *Ultrasonics, Ferroelectrics and Frequency Control, IEEE Transactions on*, **47**(6), pp. 1377–1396.

[49] Hollar, S., A. Flynn, C. Bellew, and K. Pister (2003) "Solar powered 10 mg silicon robot," in *Micro Electro Mechanical Systems, 2003. MEMS-03 Kyoto. IEEE The Sixteenth Annual International Conference on*, IEEE, pp. 706–711.

[50] Uchino, K. (2000) *Ferroelectric Devices*, Marcel Dekker, Inc.

[51] Karpelson, M., J. Whitney, G. Wei, and R. Wood (2011) "Design and fabrication of ultralight high-voltage power circuits for flapping-wing robotic insects," in *Applied Power Electronics Conference and Exposition (APEC), 2011 Twenty-Sixth Annual IEEE*, IEEE, pp. 2070–2077.

[52] Campolo, D., M. Sitti, and R. Fearing (2003) "Efficient Charge Recovery Method for Driving Piezoelectric Actuators WIth Quasi-square Waves," *IEEE Transactions on Ultrasonics, Ferroelectrics and Frequency Control*, **50**, pp. 237–244.

[53] Sitti, M., D. Campolo, J. Yan, and R. Fearing (2001) "Development of PZT and PZN-PT based unimorph actuators for micromechanical flapping mechanisms," in *Proceedings of IEEE 2001 ICRA*, pp. 3839–3846.

[54] Steltz, E. E. (2008) *Redesign of the Micromechanical Flying Insect in a Power Density Context*, Ph.D. thesis, EECS Department, University of California, Berkeley.
URL `http://www.eecs.berkeley.edu/Pubs/TechRpts/2008/EECS-2008-56.html`

[55] Wood, R. (2007) "Design, fabrication, and analysis of a 3DOF, 3cm flapping-wing MAV," in *Intelligent Robots and Systems, 2007. IROS 2007. IEEE/RSJ International Conference on*, pp. 1576–1581.

[56] Jacobsen, J. O., L. L. Howell, and S. P. Magleby (2007) "Components for the Design of Lamina Emergent Mechanisms," *ASME Conf. Proc.*, **2007**(43041), pp. 165–174.

[57] (2011), "Wowwee Dragonfly," Accessed February 29, 2012.
URL `http://www.wowwee.com/en/products/toys/flight/flytech/dragonfly`

[58] Garcia, E., Y. Nam, and N. Lobontiu (2005) "Design, Modeling, and Initial Experiments on Microscale Amplification Device," *Journal of Intelligent Material Systems and Structures*, **16**, p. 1039.

[59] Seidemann, V., S. Btefisch, and S. Bttgenbach (2002) "Fabrication and investigation of in-plane compliant SU8 structures for MEMS and their application to micro valves and micro grippers," *Sensors and Actuators A: Physical*, **97-98**, pp. 457–461.

[60] (2008) *Piezoelectric T-Beam Microactuators*.

[61] Andersen, A., U. Pesavento, and Z. J. Wang (2005) "Unsteady aerodynamics of fluttering and tumbling plates," *Journal of Fluid Mechanics*, **541**(-1), pp. 65–90.

[62] Petersen, K. (1982) "Silicon as a mechanical material," *Proceedings of the IEEE*, **70**(5), pp. 420–457.

[63] Chang, H.-K. and Y.-K. Kim (2000) "UV-LIGA process for high aspect ratio structure using stress barrier and C-shaped etch hole," *Sensors and Actuators A: Physical*, **84**(3), pp. 342–350.

[64] Chen, H. and C. Fu (2008) "An investigation into the characteristics of deep reactive ion etching of quartz using SU-8 as a mask," *Journal of Micromechanics and Microengineering*, **18**(10), pp. 105001–.

[65] Lin, C.-H., G.-B. Lee, B.-W. Chang, and G.-L. Chang (2002) "A new fabrication process for ultra-thick microfluidic microstructures utilizing SU-8 photoresist," *Journal of Micromechanics and Microengineering*, **12**(5), pp. 590–.

[66] Johnson, D. W., J. Goettert, V. Singh, and D. Yemane (2011) "SUEX process optimization for ultra-thick high-aspect ratio LIGA imaging," in *Proc. SPIE*, 1, SPIE, San Jose, California, USA, p. 7972.

[67] "HD MicroSystems™PI-2525, PI-2555, PI-2574," Accessed Feb. 15, 2012. URL `http://hdmicrosystems.com/HDMicroSystems/en_US/products/non_photodefineable/2500_dry_etch.html`

[68] "DJ Devcorp," Accessed Feb. 15, 2012. URL `http://www.djdevcorp.com/15501.html`

[69] "Polyethylene terephthalate," Accessed Feb. 15, 2012. URL `http://www.plastic-products.com/part12.htm`

[70] Howell, L. L. (2001) *Compliant Mechanisms*, John Wiley & Sons, Inc.

[71] (2010), "Parylene Properties & Characteristics," Accessed Feb. 15, 2012. URL `http://www.vp-scientific.com/parylene_properties.htm`

[72] Yao, P., G. Schneider, and D. Prather (2005) "Three-Dimensional Lithographical Fabrication of Microchannels," *Journal of Microelectromechanical Systems*, **14**(4), pp. 799–805.

[73] Yang, R. and W. Wang (2005) "A numerical and experimental study on gap compensation and wavelength selection in UV-lithography of ultra-high aspect ratio SU-8 microstructures," *Sensors and Actuators B: Chemical*, **110**(2), pp. 279–288.

[74] Wang, Q. M. and L. E. Cross (1998) "Performance Analysis of Piezoelectric Cantilever Bending Actuators," *Ferroelectrics*, **215**, pp. 187–213.

[75] Mateti, K., S. A. Tadigadapa, and C. D. Rahn (2010) "Modeling of PZT-5H T-beam Actuators for Nano Air Vehicle Flapping Wing Mechanisms," in *Proceedings of 21st International Conference on Adaptive Structures and Technologies*, University Park, Pennsylvania.

[76] Combes, S. A. and T. L. Daniel (2003) "Flexural stiffness in insect wings I. Scaling and the influence of wing venation," *J Exp Biol*, **206**(17), pp. 2979–2987.
URL http://jeb.biologists.org/cgi/content/abstract/206/17/2979

[77] Ellington, C. P. (1984) "The Aerodynamics of Hovering Insect Flight. II. Morphological Parameters," *Philosophical Transactions of the Royal Society of London. Series B, Biological Sciences*, **305**(1122), pp. 17–40.
URL http://www.jstor.org/stable/2396073

[78] Dickson, W., A. Straw, C. Poelma, and M. Dickinson (2006) "An integrative model of insect flight control," in *Proceedings of the 44th AIAA Aerospace Sciences Meeting and Exhibit*, pp. –.

[79] Sedov, L., C. Chu, H. Cohen, B. Seckler, and J. Gillis (1965) "Two Dimensional Problems in Hydrodynamics and Aerodynamics," *Physics Today*, **18**, pp. 62–.

[80] Bao, X. Q., T. Dargent, and E. Cattan (2010) "Micromachining SU-8 pivot structures using AZ photoresist as direct sacrificial layers for a large wing displacement," *Journal of Micromechanics and Microengineering*, **20**(2), pp. 025005–.
URL http://stacks.iop.org/0960-1317/20/i=2/a=025005

[81] Goldfarb, M., M. Gogola, G. Fischer, and E. Garcia (2002) "Development of piezoelectrically-actuated mesoscale robot quadruped." *Journal of Micromechatronics*, **1**(3), pp. 205–.

[82] Basak, S., A. Raman, and S. V. Garimella (2005) "Dynamic Response Optimization of Piezoelectrically Excited Thin Resonant Beams," *J. Vib. Acoust.*, **127**, pp. 18–27.
URL http://link.aip.org/link/?VAJ/127/18/1

[83] Uchino, K. and J. R. Giniewicz (2003) *Micromechatronics*, Marcel Dekker, Inc.

[84] Gross, S. J., S. Tadigadapa, T. N. Jackson, S. Trolier-McKinstry, and Q. Q. Zhang (2003) "Lead-zirconate-titanate-based piezoelectric micromachined switch," *Applied Physics Letters*, **83**(1), pp. 174–176.

[85] Feng, G.-H. and E. S. Kim (2004) "Micropump based on PZT unimorph and one-way parylene valves," *Journal of Micromechanics and Microengineering*, **14**(4), p. 429.
URL http://stacks.iop.org/0960-1317/14/i=4/a=001

[86] Iga, Y., K. Kanda, T. Fujita, K. Higuchi, and K. Maenaka (2010) "A design and fabrication of mems gyroscope using PZT thin films," in *World Automation Congress (WAC), 2010 DOI* -, pp. 1–4.

[87] Kommepalli, H., H. Yu, C. Muhlstein, S. Trolier-McKinstry, C. Rahn, and S. Tadigadapa (2009) "Design, Fabrication, and Performance of a Piezoelectric Uniflex Microactuator," *Microelectromechanical Systems, Journal of DOI - 10.1109/JMEMS.2009.2015480*, **18**(3), pp. 616–625.

[88] Xu, T.-B., Z.-Y. Cheng, and Q. M. Zhang (2002) "High-performance micromachined unimorph actuators based on electrostrictive poly(vinylidene fluoride trifluoroethylene) copolymer," *Applied Physics Letters DOI - 10.1063/1.1448661*, **80**(6), pp. 1082–1084.

[89] Kommepalli, H. K. R. (2010) *Design, Modeling and Optimization of Piezoelectric Actuators*, Ph.D. thesis, The Pennsylvania State University.

[90] (2009) *Clapping Wing Nano Air Vehicles Using Piezoelectric T-beam Actuators*.

[91] Mateti, K., Z. Zhang, S. A. Tadigadapa, and C. D. Rahn (2010) "Thrust Modeling and Measurement for Clapping Wing Nano Air Vehicles Actuated By Piezoelectric T-beams," in *Proceedings of the ASME 2010 Conference on SMASIS*, Philadelphia, Pennsylvania, USA.

[92] Wang, Q.-M., Q. Zhang, B. Xu, R. Liu, and L. E. Cross (1999) "Nonlinear piezoelectric behavior of ceramic bending mode actuators under strong electric fields," *J. Appl. Phys.*, **86**(6), pp. 3352–3360.
URL http://link.aip.org/link/?JAP/86/3352/1

[93] Kugel, V. D. and L. E. Cross (1998) "Behavior of soft piezoelectric ceramics under high sinusoidal electric fields," *J. Appl. Phys.*, **84**(5), pp. 2815–2830.
URL http://link.aip.org/link/?JAP/84/2815/1

[94] Masys, A. J., W. Ren, G. Yang, and B. K. Mukherjee (2003) "Piezoelectric strain in lead zirconate titante ceramics as a function of electric field, frequency, and dc bias," *J. Appl. Phys.*, **94**(2), pp. 1155–1162.
URL http://link.aip.org/link/?JAP/94/1155/1

[95] Erturk, A. and D. Inman (2008) "On Mechanical Modeling of Cantilevered Piezoelectric Vibration Energy Harvesters," *Journal of Intelligent Material Systems and Structures*, **19**(11), pp. 1311–1325.
URL http://jim.sagepub.com/content/19/11/1311.abstract

[96] Davis, W. (2011) "Measuring Quality Factor From a Nonlinear Frequency Response With Jump Discontinuities," *Microelectromechanical Systems, Journal of DOI - 10.1109/JMEMS.2011.2159103*, **20**(4), pp. 968–975.

[97] "SU-8 Permanent Photoresists," .
URL http://www.microchem.com/pdf/SU-8-table-of-properties.pdf

[98] Feng, R. and R. J. Farris (2003) "Influence of processing conditions on the thermal and mechanical properties of SU8 negative photoresist coatings," *Journal of Micromechanics and Microengineering*, **13**(1), pp. 80–.
URL http://stacks.iop.org/0960-1317/13/i=1/a=312

[99] Hopcroft, M., T. KRAMER, G. KIM, K. TAKASHIMA, Y. HIGO, D. MOORE, and J. BRUGGER (2005) "Micromechanical testing of SU-8 cantilevers," *Fatigue & Fracture of Engineering Materials & Structures*, **28**(8), pp. 735–742.
URL http://dx.doi.org/10.1111/j.1460-2695.2005.00873.x

[100] Proceedings of Microscale Systems: Mechanics & Measurement Symposium (2000) *Mechanical testing of EPON SU-8 with SIEM*, Brookhaven National Lab., Upton, NY (US), Orlando, FL.

[101] Lorenz, H., M. Despont, N. Fahrni, N. LaBianca, P. Renaudy, and P. Vettigerx (1997) "SU-8: a low-cost negative resist for MEMS," *Journal of Micromechanics and Microengineering*, **7**(3), pp. 121–.
URL http://stacks.iop.org/0960-1317/7/i=3/a=010

[102] Al-Halhouli, A., I. Kampen, T. Krah, and S. Bttgenbach "Nanoindentation testing of SU-8 photoresist mechanical properties," *Microelectronic Engineering*, **85**(5-6), pp. 942–944.
URL http://www.sciencedirect.com/science/article/B6V0W-4RP0MDJ-7/2/bd39c234a837f33d0a944acb823fa991

[103] Khoo, H. S., K.-K. Liu, and F.-G. Tseng (2003) "Mechanical strength and interfacial failure analysis of cantilevered SU-8 microposts," *Journal of Micromechanics and Microengineering*, **13**(6), pp. 822–.
URL http://stacks.iop.org/0960-1317/13/i=6/a=305